A High-Throughput Cell Design to Screen Bimetallic Catalysts for Electrochemical Nitrogen Reduction to Ammonia

by

Grigorios Antoniadis

to obtain the degree of Master of Science
in Sustainable Energy Technology
at the Delft University of Technology
to be defended publicly on 14 January 2021

Student number:	4853016	
Thesis committee:	Prof. dr. F.M. Mulder	TU Delft, supervisor
	Prof. dr. J.J.C. Geerlings	TU Delft
	Prof. dr.ir. J.R. van Ommen	TU Delft

TU Delft

Acknowledgements

Firstly, I would like to thank my daily supervisor, PhD candidate Martin Kolen, for his continuous support during this project. This project wouldn't have been possible without his guidance. Secondly, I would like to thank Prof. dr. F.M. Mulder for his help in solving the problems that were encountered during this project. Then, I would like to thank the PhD candidates and the lab technicians of the MECS group for their help in the laboratory. I would also like to thank the thesis committee members, Prof. dr. J.J.C. Geerlings and Prof. dr.ir. J.R. (Ruud) van Ommen for their time and effort evaluating this thesis. Finally, I would like to thank my family and my friends who always kept me motivated throughout this project.

Abstract

Ammonia (NH_3) is an important chemical used in the production of fertilizers and has the potential to become a green energy carrier. It is synthesized through the Haber-Bosch (HB) process, which involves nitrogen (N_2) and hydrogen (H_2) reacting at high temperature and pressure (400-500 ^oC, 100-200 bar) and consumes approximately 2% of the global energy supply. An alternative to this energy intensive process is the electrocatalytic nitrogen reduction reaction (NRR). The main challenge of this approach is the competing hydrogen evolution reaction (HER) that consumes most of the applied electricity, making the ammonia production inefficient. Based on the Sabatier principle, an ideal catalyst for the NRR would bind nitrogen and ammonia optimally, while hydrogen would be bound too strongly or too weakly, suppressing the HER. So far, no such catalyst has been found. A strategy that could lead to the discovery of a suitable catalyst is alloying, since materials with new adsorption properties can be created this way. The main goal of this project is to design an electrochemical cell that can be used for the screening of large numbers of bimetallic catalysts, increasing the chance of finding a suitable NRR catalyst. For this so-called high-throughput approach an electrochemical cell was designed that allows the screening of up to 16 catalysts in parallel. Furthermore, methods for sample preparation, characterisation and detection were developed that are compatible with a high-throughput technique.

List of abbreviations

ALD	=	Atomic Layer Deposition
CE	=	Counter Electrode
CO_2RR	=	Carbon Dioxide Reduction Reaction
DFT	=	Density Functional Theory
DMFC	=	Direct Methanol Fuel Cell
EDS	=	Energy-Dispersive X-Ray Spectroscopy
EPDM	=	Ethylene Propylene Diene Monomer
EPTFE	=	Expanded Polytetrafluoroethylene
FE	=	Faradaic Efficiency
GC	=	Gas chromatography
GDE	=	Gas Diffusion Electrode
GDL	=	Gas Diffusion Layer
HB	=	Haber-Bosch
HER	=	Hydrogen Evolution Reaction
HOR	=	Hydrogen Oxidation Reaction
HTE	=	High-Throughput Experimentation
HTP	=	High-Throughput
MFC	=	Mass Flow Controller
NMR	=	Nuclear Magnetic Resonance
NRR	=	Nitrogen Reduction Reaction
OER	=	Oxygen Evolution Reaction
ORR	=	Oxygen Reduction Reaction
PCB	=	Printed Circuit Board
PEM	=	Polymer Electron Membrane
PVD	=	Physical Vapor Deposition
RE	=	Reference Electrode
RHE	=	Reversible Hydrogen Electrode
SEM	=	Scanning Electron Microscopy
WE	=	Working Electrode
XRD	=	X-Ray Diffraction

Table of contents

1
Introduction

The conversion of atmospheric nitrogen (N_2) to ammonia (NH_3) is considered to be one of the most essential industrial processes in today's world due to its crucial role in the manufacturing of fertilizers [1]. With the continuous growth of the global population, the agricultural sector is heavily dependent on fertilizers to increase the yield of crops and raise the amount of natural nutrients present in cultivated soil [2]. However, ammonia is also an important green energy carrier, can be used as a fuel for the transportation industry and is an attractive option for seasonal energy storage applications [3]. Since the early 20th century, ammonia is produced industrially through the Haber-Bosch process, in which N_2 and H_2 react at high temperature and pressure over iron or ruthenium catalysts to form ammonia [4]. Due to these harsh reaction conditions and the production of hydrogen from steam methane reforming of natural gas, the fertilizer industry is responsible for approximately 2% of the global energy consumption and around 1% of the global CO_2 emissions [5, 6]. This highlights the importance of developing a new sustainable process for the production of ammonia, relying on renewable technologies and taking place at ambient conditions [7].

This necessity has led to interest in the field of electrocatalysis, specifically the nitrogen reduction reaction (NRR), which involves the dissociation of molecular nitrogen and water to ammonia over a metal catalyst [8]. NRR has many advantages over the traditional HB process, like reducing its high energy requirements and the carbon footprint, substantially reducing the size of ammonia plants and allowing for more decentralized ammonia production [9]. However, most of the reported catalysts for the electrochemical reduction of nitrogen to ammonia suffer from poor faradaic efficiencies (FE) and minimal ammonia yield in ambient conditions.

The main challenge of the NRR is the competing hydrogen evolution reaction (HER), which consumes the majority of the provided electrons for most of the studied metal catalysts, leading to poor FEs towards NH_3 production [10]. HER dominates on most catalyst surfaces because electrocatalytic NRR requires the splitting of the very strong N≡N bond that causes NRR to have sluggish kinetics. Additionally, the hydrogenation process involves the formation of three N-H bonds to create NH_3, which is very difficult to occur if molecular nitrogen is bound too strongly on the catalyst surface. According to the Sabatier principle, the optimal catalyst for NRR should neither bind N_2 too strongly nor too weakly on the surface of the catalyst, leading to the creation of volcano plots [2, 11]. A volcano plot describes the catalytic activity as a function of nitrogen binding energy (see Figure 2.1). Theoretical DFT calculations for single metal catalysts show that HER is more favourable than NRR because the volcano

for HER is at lower overpotentials. So far, this has been confirmed experimentally because reported FEs for NRR are low [12].

One tool that can be used to rapidly manufacture and screen catalysts is High Throughput (HTP) experimentation. High throughput strategies allow researchers to conduct experiments, where many combinations of test variables are involved, in a time efficient manner [13]. By screening an array of catalyst compositions simultaneously, the total number of material combinations that can be tested in a project that utilizes HTP techniques is orders of magnitude higher compared to one that follows conventional experimental procedures [14].

A promising strategy that can be employed in combination with HTP techniques to overcome the problems of single metal catalysts is alloying. New catalysts with nitrogen adsorption properties that differ from their parent metals can be created through alloying [15]. This is a promising strategy that is already implemented in the field of CO_2RR to facilitate the discovery of new catalysts [16]. In addition, electrochemical HTP systems have some unique challenges that need to be addressed by the cell design. The two most commonly used cell designs are the Gas Diffusion Electrode (GDE) and the H-cell. As we will see later, the different cell designs can heavily influence the maximum current density and the mass transport limitations of the electrochemical system [17].

In this project, a high-throughput electrochemical GDE cell design will be presented and compared to conventional electrochemical setups. The advantages and disadvantages of several 3D printed cell designs will be discussed, along with the supporting components of the cell. These components include the ePTFE Gas Diffusion Layer (GDL) and the Printed Circuit Board (PCB) used to establish an electrical contact between each individual catalyst and the potentiostat. Furthermore, the preparation of bimetallic catalysts through magnetron sputtering will be demonstrated, as a suitable method to manufacture and characterize 16 bimetallic catalysts in a single deposition. The functionality of the HTP cell as a tool to screen electrocatalysts in parallel will be validated by means of high-throughput chronopotentiometry experiments for oxygen reduction (ORR) and HER and Nuclear Magnetic Resonance (NMR). Additionally, contamination checks will be conducted to measure the NH_3 background concentration and the crossover between the HTP cell compartments. Finally, an experiment with nitrate (NO_3^-) will be conducted to show that an active catalyst could be detected by means of Gas Chromatography (GC) and NMR in the gas and liquid phase respectively.

2
Theoretical background

In this chapter the fundamental principles of the electrocatalytic NRR will be discussed. Next, high-throughput techniques implemented in literature for electrochemical experiments will be discussed with a focus on the cell design of the electrochemical cell.

2.1. Fundamentals of electrocatalytic NRR

The first reliable case of electrochemical NRR was reported in 1922 by Fichter and Suter [18]. However, during the first decade of the 20th century, Fritz Haber and Carl Bosch had already discovered a thermal pathway towards the formation of ammonia [19]. They would later be awarded the Nobel prize in 1918 and 1931 respectively for what came to be known as the Haber-Bosch process. Even though the HB process has been the dominant method for the industrial production of ammonia for the past 100 years, growing environmental concerns have led to increasing interest around the electrochemical pathway. The discovery of a process to generate ammonia electrochemically from atmospheric nitrogen would allow for the production of fertilizers from sustainable energy sources directly at the point of use [20]. It would also provide an opportunity to use ammonia as an energy carrier on a large scale. NH_3 is a very good hydrogen carrier, as it satisfies safety concerns and energy density problems for mobile applications, compared to hydrogen [21]. Also, it can utilize the existing infrastructure and storage facilities used for natural gas.

In an electrocatalytic cell for NRR in alkaline environment, the two reactions that can occur at the cathode are NRR and HER, while OER will occur at the anode. These reactions are summarized in Eq. (2.1)-(2.3):

NRR $$N_2 + 6H_2O + 6e^- \leftrightarrow 2NH_3 + 6OH^- \quad (2.1)$$

HER $$2H_2O + 2e^- \leftrightarrow H_2 + 2OH^- \quad (2.2)$$

OER $$4OH^-(aq) \rightarrow O_2(g) + 2H_2O(l) + 4e^- \quad (2.3)$$

The electrochemical NRR on a heterogeneous catalyst surface can follow two possible pathways: the dissociative and the associative pathway [22]. Looking at the dissociative pathway first, a N_2 molecule is adsorbed on the catalyst surface and the triple N≡N bond is split, a process which requires a large energy input, since the triple nitrogen bond is highly inert and therefore hard to split. This is followed by the hydrogenation process, where H atoms are added to the N atom one at a time, until an

NH_3 molecule is formed and released [7]. The elementary reaction steps and the intermediate products for the dissociative pathway are shown in Equations (2.4)-(2.7), where * denotes a surface site:

$$N_2 + 2^* \rightarrow 2^*N \tag{2.4}$$

$$2^*N + 2e^- + 2H^+ \rightarrow 2^*NH \tag{2.5}$$

$$2^*NH + 2e^- + 2H^+ \rightarrow 2^*NH_2 \tag{2.6}$$

$$2^*NH_2 + 2e^- + 2H^+ \rightarrow 2NH_3 + 2^* \tag{2.7}$$

The main difference between the dissociative and the associative pathways is that in the latter the triple nitrogen bond doesn't break when the N_2 molecule is adsorbed on the catalyst surface and the two nitrogen atoms remain bonded until the desorbtion of the first NH_3 molecule. As a result, the hydrogenation process of the two nitrogen atoms can happen in two possible ways, either through the associative distal pathway or the associative alternating pathway [4]. In the former, hydrogen atoms are only added to one of the nitrogen atoms until an ammonia molecule is formed and released. Then, the same hydrogenation process occurs as for the dissociative pathway for the remaining Nitrogen atom. In the alternating pathway, a hydrogen atom is attached sequentially to each one of the two nitrogen atoms, until two ammonia molecules are formed and released in quick succession [10]. The elementary steps for the two possible associative pathways are shown in in Equations (2.8-2.21):

Associative distal pathway:

$$N_2 + * \rightarrow *N_2 \tag{2.8}$$

$$*N_2 + e^- + H^+ \rightarrow *NNH \tag{2.9}$$

$$*NNH + e^- + H^+ \rightarrow *NNH_2 \tag{2.10}$$

$$*NNH_2 + e^- + H^+ \rightarrow *N + NH_3 \tag{2.11}$$

$$*N + e^- + H^+ \rightarrow *NH \tag{2.12}$$

$$*NH + e^- + H^+ \rightarrow *NH_2 \tag{2.13}$$

$$*NH_2 + e^- + H^+ \rightarrow NH_3 + * \tag{2.14}$$

Associative alternating pathway:

$$N_2 + * \rightarrow *N_2 \tag{2.15}$$

$$*N_2 + e^- + H^+ \rightarrow *NNH \tag{2.16}$$

$$*NNH + e^- + H^+ \rightarrow *NHNH \tag{2.17}$$

$$*NHNH + e^- + H^+ \rightarrow *NHNH_2 \tag{2.18}$$

$$*NHNH_2 + e^- + H^+ \rightarrow *NH_2NH_2 \tag{2.19}$$

$$*NH_2NH_2 + e^- + H^+ \rightarrow *NH_2 + NH_3 \tag{2.20}$$

$$*NH_2 + e^- + H^+ \rightarrow NH_3 + * \tag{2.21}$$

Through density functional theory (DFT) calculations, the free energy change of each reaction step can be estimated, which is an indication of the stability of the produced intermediates. This allows the identification of key intermediates and limiting steps of the mechanism [7]. In the work of Montoya *et. al*. it is shown that the electrochemical NRR is limited by the protonation of $*N_2$ to $*N_2H$ in Eq. (2.9) for less reactive transition metals that bind nitrogen weakly, like Au(211) surfaces [11]. This trend is representative of (111) and (211) unreactive metal surfaces. In the case of more reactive transition metal catalyst surfaces, where nitrogen is bound strongly, the potential limiting step can either be the desorption of $*NH_2$ to NH_3, shown in Eq. (2.14), or the protonation of *NH to $*NH_2$, shown in Eq. (2.13). The former was demonstrated on Ru(211) surfaces, which is considered representative of reactive (211) surfaces, while the latter was demonstrated on Re(111) surfaces, which is considered representative of reactive (111) surfaces.

The relationships between the binding energy of different reaction intermediates over a variety of catalytic surfaces are called scaling relationships [23]. In order to compare the catalytic activity of different metals, these scaling relations can be summarized in volcano plots. In a volcano plot, the minimum potential for the rate limiting step of the nitrogen reduction reaction is plotted versus the binding energy of nitrogen, ΔG_N [22]. The limiting potential of the hydrogen evolution reaction for the same metals can also be added to the same plot. The outcome of such an analysis is presented in Figure 2.1:

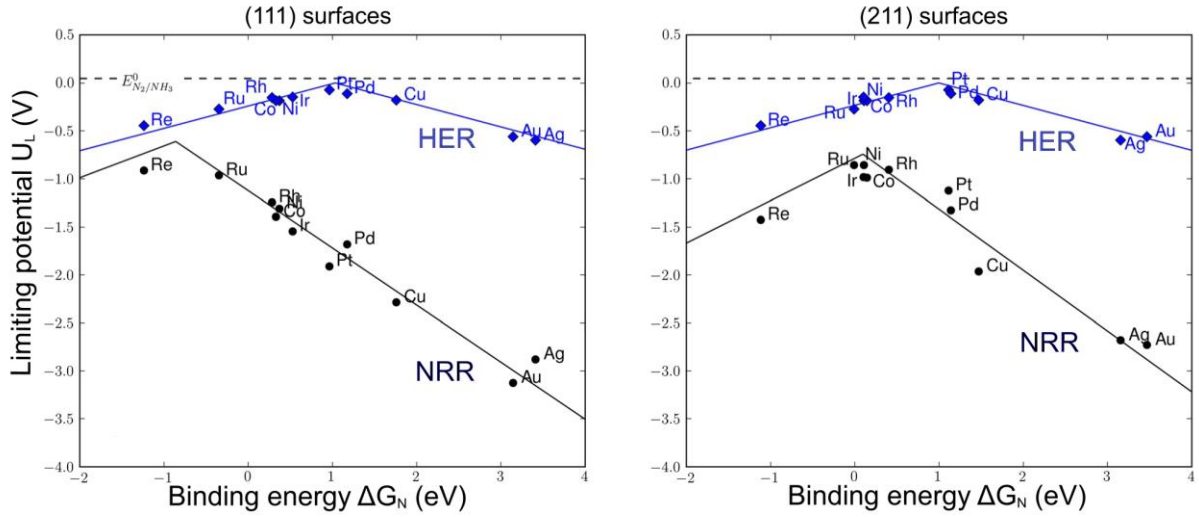

Figure 2.1. HER and NRR limiting potential, U_L, versus the nitrogen binding energy, ΔG_N, for (111) and (211) metal surfaces. Adapted from [11].

The volcano plots of Figure 2.1 demonstrate the main difficulty of NRR on single metal catalyst surfaces. The limiting potential required for NRR is always more negative than the limiting potential

required for HER for any single metal [20]. This leads to poor selectivity and faradaic efficiency (FE) for the formation of NH_3, since most of the applied current will go towards H_2 formation. For this reason, it is challenging to discover a favorable catalyst for NRR.

A promising strategy for the discovery of an optimal catalyst is alloying. A bimetallic alloy can have entirely new adsorption properties from those of its constituent metals, which allows for the creation of new catalysts with improved selectivity and stability [15]. The difference in catalytic properties originates from the various bimetallic surfaces that can be created and interact in a different way with the adsorbed reaction intermediates. As a result, there is an endless number of combinations of metals that could potentially be optimal catalysts. Alloying as a strategy to improve product selectivity of electrocatalytic reactions has been for example successfully applied to the reduction of CO_2 to ethylene [16]. The variables that can change are the type of metal, the composition of the alloy, the current density and the morphology of its surface. However, the theoretical prediction of active catalysts still remains very challenging. Furthermore, the conventional screening processes of the manufactured catalysts are very time consuming as they involve experiments where only a single catalyst is tested at a time. A more efficient way to test all these different configurations is running them at the same time in parallel, something that can be achieved with high throughput experimentation (HTE).

2.2. High throughput experimentation (HTE)

High throughput techniques provide an alternative solution to single experiments when there is a large number of different material variables that can be changed between each experiment. It allows researchers to conduct experiments with multiple combinations of test variables at the same time by running them in parallel or by using a programmed automated procedure [13]. As a result, the overall time requirements for the same number of experiments is orders of magnitude lower for a project that applies high throughput experimentation compared to a conventional one. A typical strategy applied when using high throughput techniques is that initially a wide range of materials is screened in quick succession. Researchers aim to get initial results that would serve as a starting point for more in-depth experiments with the most promising materials [13].

High throughput experimentation is very well suited for electrochemical research because the number of promising materials exceeds by far the number of materials that can be tested. A requirement of applying high throughput techniques to electrocatalysis is that multiple catalysts must be manufactured simultaneously instead of only one at a time [24]. This increases the accessibility of binary and ternary compounds that would have been difficult to produce through conventional techniques [13].

High throughput and combinatorial strategies have been successfully applied to the field of electrocatalysis and the most prominent of those applications will be discussed here. One such example is the manufacture of an array with 645 distinct electrodes by Reddington et al. for direct methanol fuel cells (DMFCs) [25]. The electrodes were used as anode materials and they were manufactured out of a

combination of five elements (Pt, Ru, Os, Ir and Rh). The array of the catalysts was designed by using an inkjet printer to deposit metal salt inks on a conductive Toray carbon paper. The resulting quaternary array is presented in Figure 2.2:

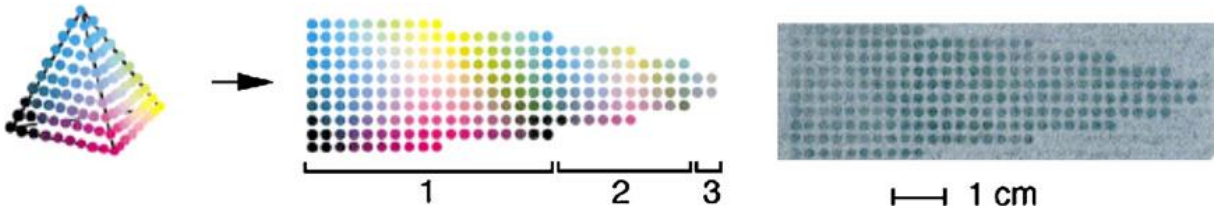

Figure 2.2. Left: Schematic representation of the quaternary map that contains 220 distinct spots of different composition. Right: Borohydride-reduced, inkjet-printed metal array on Toray carbon paper. Adapted from [25].

Another technique that was implemented in this project to accelerate the experiments was the fluorescent optical detection system. Since the oxidation reaction of methanol to carbon dioxide involves the release of six protons, the fluorescent detector provides a visual indication when the concentration of protons is increased in the electrolyte [26]. This allowed for a quick way to map the activity of the array with respect to the oxidation of methanol. They were able to discover that a composition of $Pt_{44}Ru_{41}Os_{10}Ir_5$ improved the current density of the fuel cell by 40% compared to the commercially established $Pt_{50}Ru_{50}$ catalyst.

Improved catalysts for the cathode electrode of fuel cells have also been investigated, aiming to increase the open circuit potential of the oxygen reduction reaction (ORR). A notable approach utilizing high throughput techniques has been demonstrated by Cooper et al., where a combinatorial library was designed from metal systems of Pt, Ru, Co, Ti, Cu, and Cr [27]. These material libraries were created through plasma sputtering on a silicon wafer with discrete gold electrodes, shown in Fig. 2.3. The material libraries were screened using cyclic voltammetry, with all electrodes running simultaneously. By rapidly screening these catalyst compositions, the researchers managed to identify a composition of $Pt_{28}Co_{36}Cr_{36}$ that exhibited a higher onset potential compared to the conventional Pt catalyst.

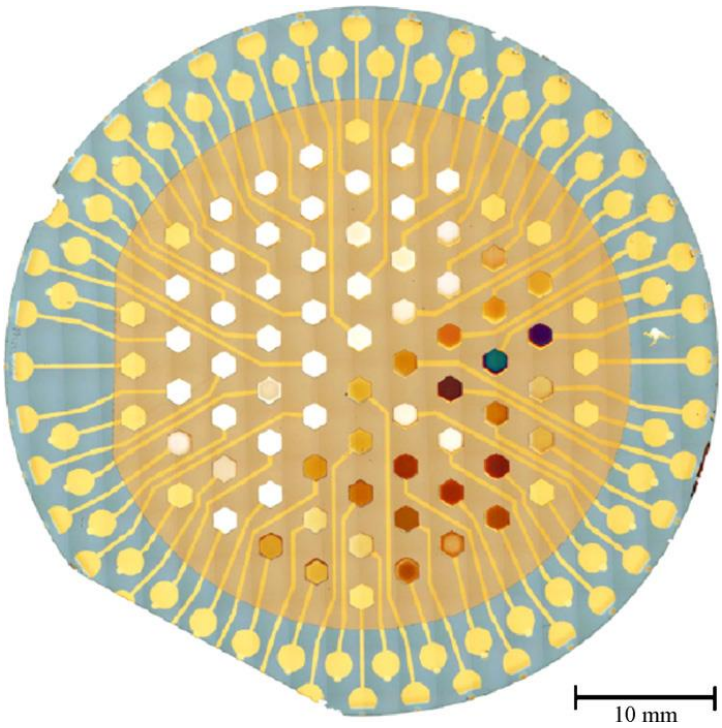

Figure 2.3. Combinatorial library schematic with gold electrodes on a silicon wafer substrate. The gold contact points in the perimeter of the wafer are connected to a multichannel potentiostat. The hexagonal points in the interior of the wafer house the different alloy compositions. Adapted from [27].

The use of high throughput techniques can also be seen in the field of polymer electron membrane (PEM) fuel cells. Alloys with random compositions of $Pt_{1-x}M_x$ (M = Ru, Mo, Co, Ta, Au, Sn) were created using magnetron sputtering for use in a 64-electrode PEM fuel cell [28]. This fuel cell was used to test the performance of the catalysts for the hydrogen oxidation reaction (HOR), while at the same time checking the tolerance of these materials to carbon monoxide poisoning. It was found that PtRu and PtMo enhanced the catalytic activity of the HOR and improved the CO tolerance of Pt. The researchers concluded that the use of high throughput strategies allowed them to prepare and test each binary set of alloys in a timespan of two weeks, a process that would have taken considerably longer through conventional experimental procedures.

All of the high throughput strategies discussed previously are very valuable for the fields of electrocatalysis and materials research. They have allowed for significant advances in these fields by providing the tools for rapid manufacture and screening of multiple catalyst compositions simultaneously [13]. However, each application comes with unique challenges for the cell design. The two main electrochemical cell designs used in electrocatalytic research will be discussed in the following section.

2.3. GDE vs H-cell design

The electrochemical cell that was designed in this project involves the use of gaseous reactants. Two cell configurations that are suitable for applications with gaseous reactants and commonly used in the field of electrocatalysis are gas diffusion electrodes (GDEs) and H-cells [17]. In both of these designs the gas reactant (CO_2, O_2, N_2) is supplied to the surface of the catalyst that is in contact with an electrolyte. The electrolyte can either be a liquid or a solid material and is responsible for the transfer of ions released during the electrochemical reactions. For an H-cell configuration, the gas is bubbled into the electrolyte and is allowed to diffuse through the boundary layer of the electrolyte with the catalyst surface [29]. However, in a GDE configuration the gas enters the cell through an adjacent gas phase and then diffuses through a gas diffusion layer (GDL) to reach the catalyst layer [17]. A schematic representation of a GDE and an H-cell for a typical CO_2 reduction system can be seen in Figures 2.4(a) and 2.4(b) respectively.

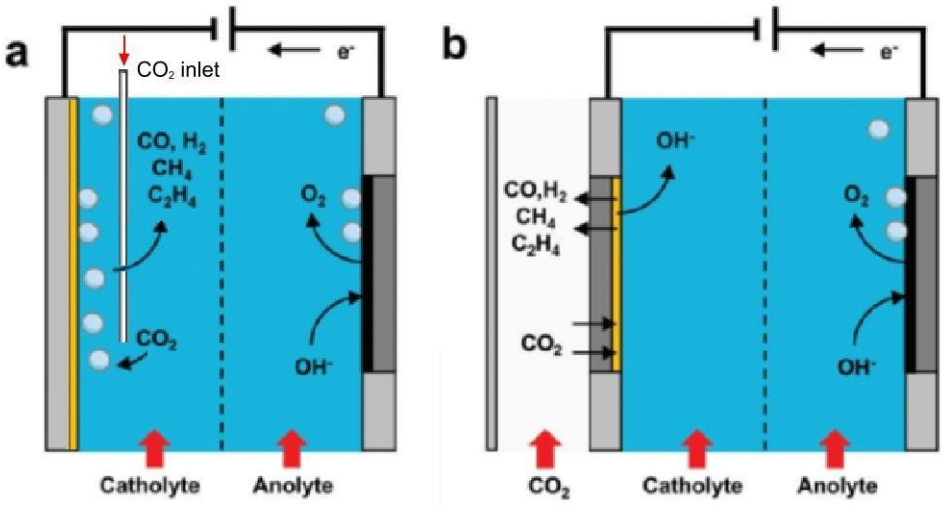

Figure 2.4. Schematic view of two cell designs for CO_2 reduction. (a) Schematic view of an H-cell where the catalyst (yellow area) is deposited on a solid substrate and the gas is bubbled directly inside the electrolyte through a tube. (b) Schematic view of a GDE where the catalyst is deposited on a gas diffusion layer where the gas is supplied from an adjacent compartment. Adapted from [17].

For the H-cell that is depicted in Figure 2.4(a), the reactant gas is bubbled inside the catholyte compartment and flows over the catalyst surface (yellow area), where the reaction can occur. The products of this reaction are released inside the electrolyte and flow outside of the cell, where they are collected. However, in the GDE configuration of Figure 2.4(b), the catalyst (yellow area) is deposited on a hydrophobic substrate, aiming to separate the gas compartment from the catholyte compartments and prevent the former from flooding. As a result, a gas-liquid interface is formed between the microporous layer inside the GDL and the catalyst layer that is in contact with the electrolyte [30].

The most significant advantage that the GDE configuration offers over the H-cell is that the diffusion length of the gas until it reaches the catalyst layer is much shorter in the GDE design. In fact, the diffusion length for the GDE (~50 nm) is three orders of magnitude smaller than the diffusion length in an H-cell (~50 μm) [17]. Consequently, a considerably larger flow of reactant gas can reach the catalyst layer, which means that higher current densities can be reached because mass transport limitations are prevented [31]. Achieving higher current densities is crucial for the transition of these technologies from the lab scale to the industrial scale.

Furthermore, in an H-cell the catalyst is usually deposited on an electrode, where only the outer layer of the material has access to the gas reagent. Due to the long diffusion length, the gas is unable to reach the bulk of the catalyst material, which severely reduces the surface area available for the reaction to occur [32]. On the contrary, the catalyst layer in a GDE cell is deposited on a porous structure that allows gas to diffuse through it. The porous structure, has a much larger surface area where an electrochemical reaction can occur compared to the surface area of the H-cell. Additionally, having a smaller diffusion pathway allows the gas products to easily diffuse back into the gas phase and reduces the risk of them sticking on the catalyst surface and blocking the catalytically active sites [30].

3
Materials and methods

In this chapter the high throughput cell design for screening 16 different catalysts simultaneously will be presented. Additionally, all the supporting components of the HTP cell will be described. Next, the experimental setup that was used for conducting the electrochemical experiments will be presented, along with the potentiostat and the rest of the supporting instruments. Then, the physical characterization methods (SEM, XRD) as well as the detection methods (GC, NMR) utilized in this project will be discussed. Furthermore, the procedure that was followed for the preparation of the samples through magnetron sputtering will be shown, along with a calculator that was developed to predict the composition of the bimetallic alloys. Finally, the design of experiments will be presented, detailing the choice of the initial bimetallic catalysts that were used for the validation experiments of the HTP cell.

3.1. High throughput cell design

The first design decision that had to be made in this project was the choice between a GDE and an H-cell. A GDE cell offers a better pathway for the nitrogen gas to the catalyst surface by reducing the diffusion length in the GDL and minimizing mass transport limitations. Furthermore, a gas dispersion system is not required in a GDE cell unlike in an H-cell. This reduces the overall volume of the cell and the electrolyte, which makes NH_3 detection easier (see Section 3.5). Additionally, it is easier to achieve homogeneous mass transport across the whole cross section of the cell due to the way that the reactant gas is supplied to the catalyst surface. Depositing the catalyst on a porous structure also increases the surface area of the catalyst layer, which leads to lower overpotentials. Finally, gas flow in a GDE cell is lower compared to an H-cell because of the short residence time of bubbles in the H-cell design. The lower flow rate makes it easier to detect NH_3 present in the gas phase [33]. After outlining the advantages of the GDE cell over the H-cell design, it was clear that the former would be a more suitable design for this project. Consequently, the chosen design would be a GDE cell configuration with three separate compartments, the gas, catholyte and anolyte compartments.

3.1.1. Carbon GDE cell design

This section describes the carbon GDE cell iteration, while the following section describes the ePTFE cell design, which was the substrate material used for the final high throughput cell in this project. These designs will be evaluated in terms of gas and liquid leakage, bubbles forming in the cell compartments,

passivation of the electrical contacts, the design of the external electrical contacts and whether the cell can be easily and rapidly assembled.

The GDL and the type of material it is made of is an important component of the GDE configuration. The two candidates were a carbon paper by Freudenberg and a supported ePTFE by Pieper Filter GmbH, shown in Figures 3.1(a) and 3.1(b) respectively. This GDL would act as a support for the catalyst, with the metals deposited on the microporous hydrophobic side of the material. The carbon paper is a material that is electrically conductive, while the supported ePTFE isn't. This means that screening 16 distinct bimetallic catalysts simultaneously would also require 16 distinct carbon papers, since each one of the catalysts requires a separate connection to the potentiostat. However, the carbon GDL would offer lower resistance of the conductive layer and an easier electrical contact from the dry backside of the GDL rather than the side that is in contact with the electrolyte, which is necessary with a non-conductive substrate such as ePTFE.

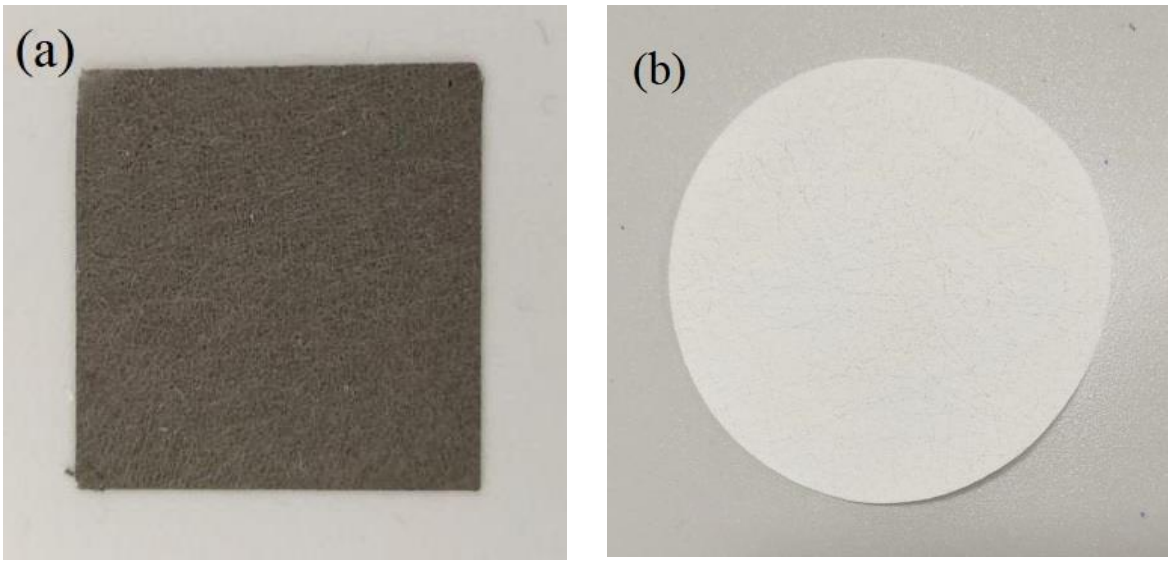

Figure 3.1. (a) Supported side of the carbon paper GDL. The catalyst is deposited on the microporous hydrophobic layer on the opposite side. (b) Hydrophobic side of the backed ePTFE GDL. This side consists of a 0.45 μm PTFE layer, which is supported on a porous polypropylene fleece, similar to the carbon paper GDE, supporting the PTFE layer.

The carbon GDE cell will be presented here, while the final High-Throughput cell design is presented in Figure 3.14. The three main parts of the carbon GDE cell (gas, catholyte, anolyte) were designed in Autodesk Inventor Professional 2019 and 3D printed in a Formlabs Form 2 printer, using the Clear Photopolymer resin by Formlabs. Subsequently, they were rinsed in a Form Wash automatic cleaner with isopropanol and dried in a Form Wash dryer for 15 minutes at 60 ^{o}C. First of all, the gas part (Figure 3.2) is the one that facilitates the nitrogen transport in and out of the cell, as well as any reaction products. It consists of a gas inlet that splits into 4 channels below the surface of the part. These channels connect the 16 holes located in the center of the cell. Each one of these holes provides a

pathway for the gas to travel through and reach the GDL. The 4 channels converge into one at the gas outlet. The 4 additional holes at the corners of the part is where M6 stainless steel screws from Fabory are placed.

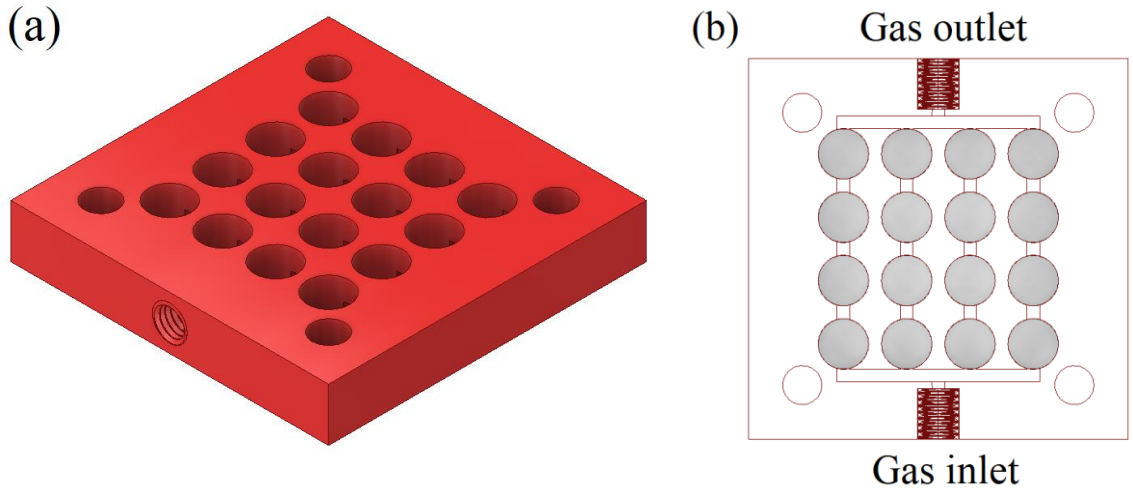

Figure 3.2. (a) 3-dimensional isometric view of the gas part. (b) 2-dimensional top view of the gas part, showing the gas inlet, gas outlet and the 4 channels that connect the 16 holes at the center of the cell.

The next part of the cell that is placed on top of the gas part is the PCB. The purpose of this part is to establish an electrical contact between each one of the 16 catalysts and a multichannel potentiostat. The PCB presented in Figure 3.3 was designed using Autodesk EAGLE and was supplied by JLCPCB. It consists of 16 gold rings with an outside diameter of 7.6 mm and an inside diameter of 6 mm. Each one of the 16 gold rings is electrically connected to one of the external electrical contacts, which in turn have to be connected to a separate channel of the potentiostat. Considering that the area available for a cable to attach to the external contacts is very small, copper tape was attached to each external contact and then the cables of the potentiostat were attached to the copper tape. However, the copper tape proved to be problematic because it caused electrolyte leakage and led to stability issues with the measured voltage.

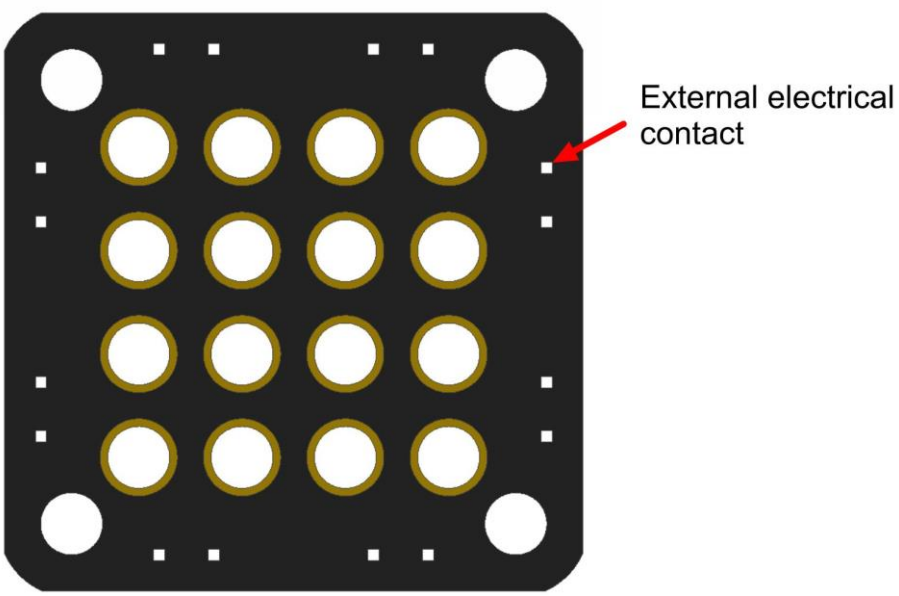

Figure 3.3. Printed circuit board (PCB) schematic representation. The black area of the PCB is made out of a non-conductive material, intending to electrically isolate each gold ring from the rest.

The next part that is required after the PCB holds the 16 individual catalysts in place. This part is shown in Figure 3.4 and will henceforth be referred to as the ‘grid’. The carbon GDLs are 8 mm in diameter and are placed directly on top of the gold rigs of the PCB, with the grid helping in properly aligning them on the PCB. Most importantly though, using a grid allows each GDL to be electrically isolated from the rest. If only a single carbon GDL was used, that would lead to all of the gold rings being electrically connected to each other. The carbon GDLs are the Working Electrodes (WEs) in this configuration. Additionally, a 1mm thick gasket ring from rubber EPDM is placed on each GDL to provide sealing and prevent the electrolyte from leaking. The outer diameter of the gasket ring is 8mm while the inner diameter is 6 mm. Figure 3.4 shows the grid, the carbon GDLs and the gasket rings.

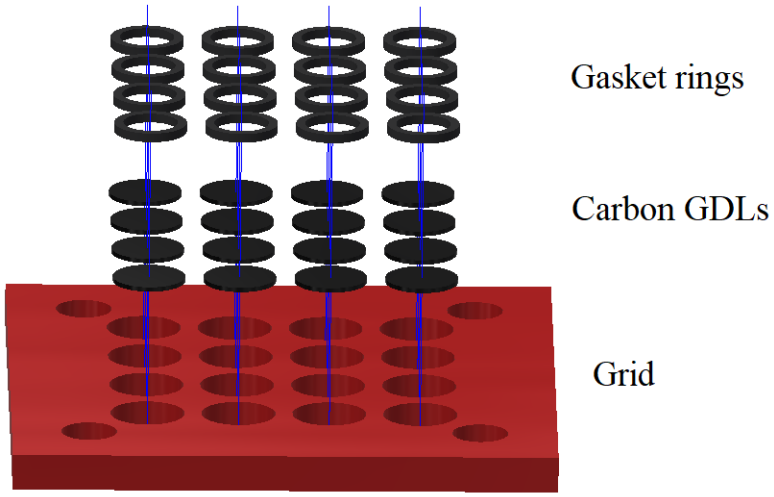

Figure 3.4. Schematic representation of the correct alignment of the grid with the carbon GDLs and the gasket rings.

The catholyte part is the next part of the cell and it is placed on top of the grid. Similar to the design of the gas part, the catholyte part shown in Figure 3.5(a), contains an inlet and an outlet for the electrolyte, with the 16 holes in the middle connected by 4 channels. However, the catholyte part has 16 overhangs of 6 mm inner diameter and 8 mm outer diameter, which can fit inside the grid. The top area of each overhang is pressed onto the gasket rings to prevent any electrolyte leakage. Furthermore, the 16 holes through the catholyte part create a pathway for the ions to travel from the catholyte to the anolyte.

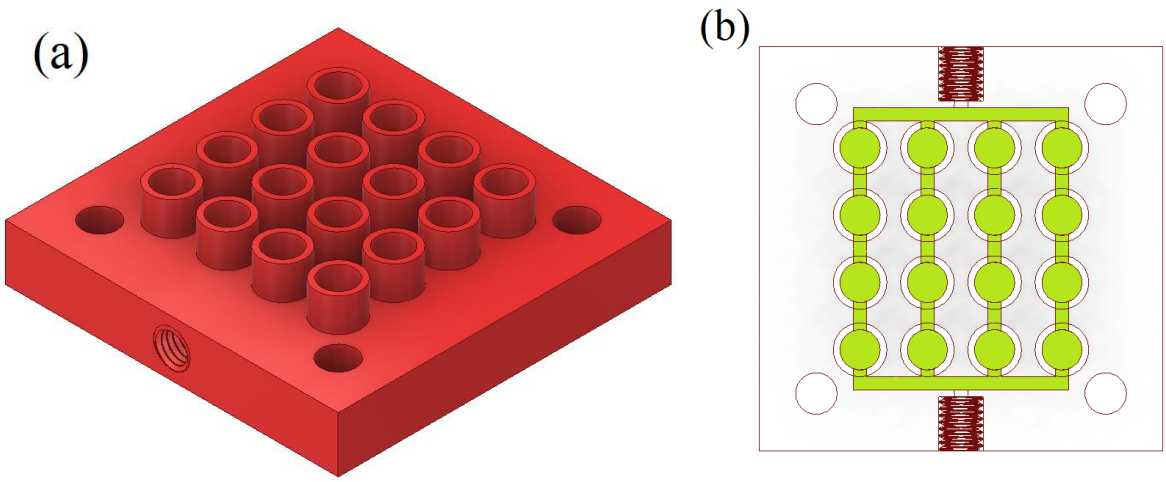

Figure 3.5. (a) 3-dimensional isometric view of the catholyte part. The 16 overhangs are connected by 4 channels below the surface of the part, similar to the channels of the gas part. (b) 2-dimensional top view of the gas part. The green area in the channels and the 16 holes is filled with electrolyte to facilitate the transfer of ions from catholyte to anolyte.

Finally, the last part of the cell is the anolyte compartment. This part is identical to the gas part of Figure 3.2, except for the 16 holes in the middle that are 6 mm in diameter instead of 8 mm. However, unlike the gas part that is used as a pathway for the gas to the catalyst layer, the anolyte part is filled with electrolyte to complete the pathway for the ions originating in the catholyte compartment. The Counter Electrode (CE) is a spiral nickel wire and it is placed between the catholyte and the anolyte compartments. The schematic of the anolyte part is presented in Figure 3.6:

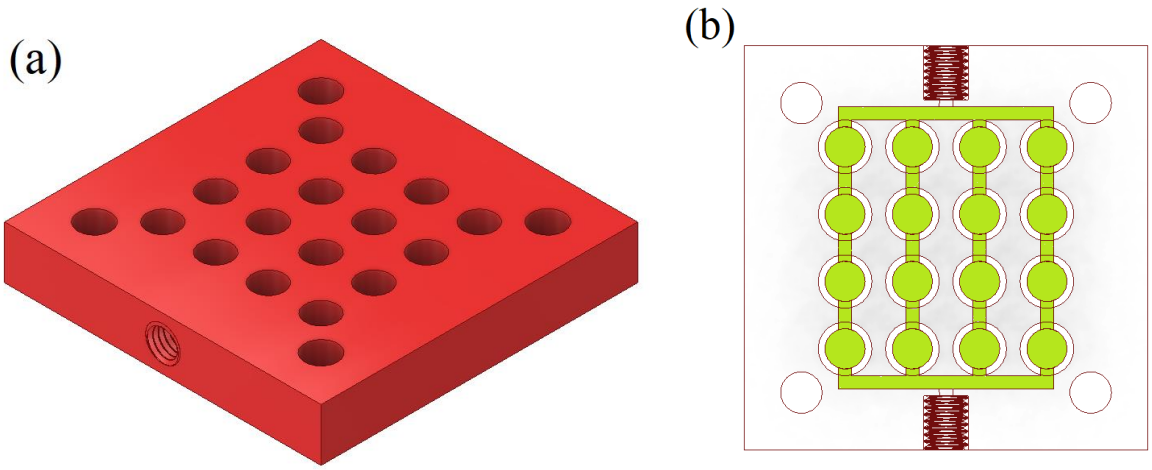

Figure 3.6. (a) 3-dimensional isometric view of the anolyte part. Unlike the catholyte part, the 16 holes in the middle are not through and the part but are closed, similar to the gas part. (b) 2-dimensional top view of the gas part. The green area represents the electrolyte that receives the ions coming from the catholyte.

The completed cell that was used to test the viability of the carbon GDE design is shown in Figure 3.7. No electrochemical experiments were conducted with this cell, only experiments to test the structural stability of the carbon GDL, the overhang and whether the cell was leak tight.

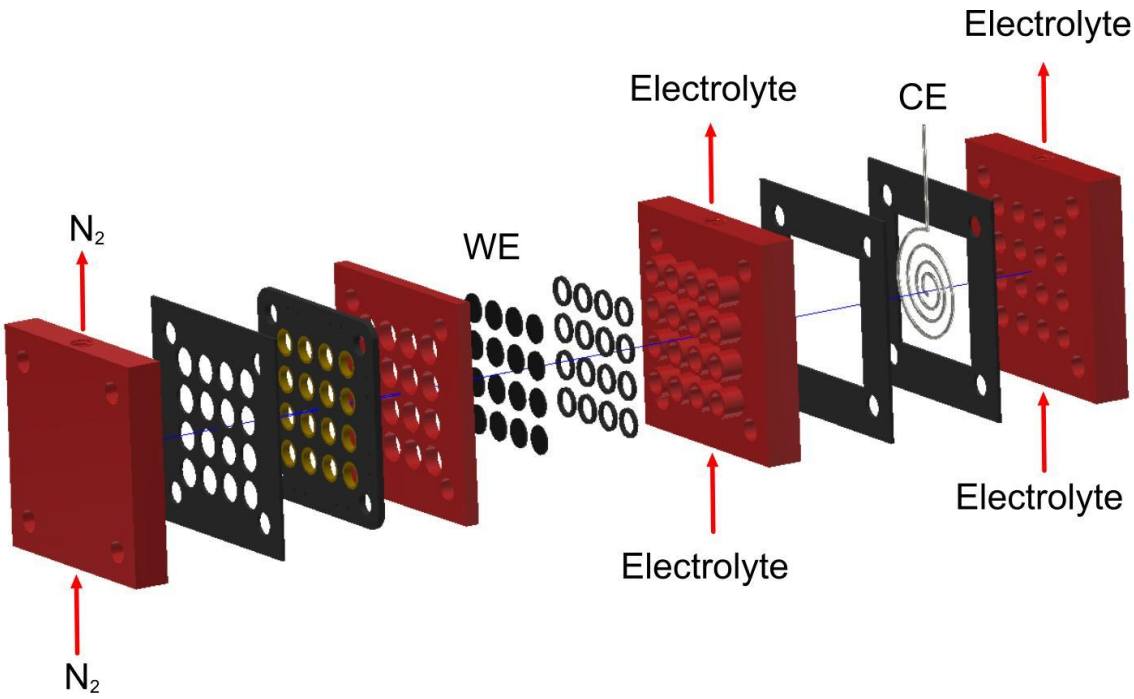

Figure 3.7. Carbon GDE cell assembly. The parts of the cell from left to right are: gas part, EPDM gasket, PCB, grid, carbon GDL (x16), gasket ring (x16), catholyte, EPDM gasket, spiral Ni wire, EPDM gasket, anolyte. The area between the carbon GDL and the anolyte contains the electrolyte.

This experimental configuration highlighted the problems that accompany a design with 16 distinct GDLs. In order for the cell to be leak tight, each one of the contact points between the carbon GDLs and the gasket rings, as well as the contact points between the gasket rings and the catholyte overhangs, has to be sealed correctly. Such a configuration proved very difficult and time consuming to assemble, due to the high number of individual carbon GDLs and gasket rings. Additionally, some of the carbon GDLs were damaged by the overhang of the catholyte part, causing electrolyte to leak into the gas compartment. Overall, considering that the carbon GDL material was difficult to cut in a circular shape, leading to carbon GDLs with inconsistent dimensions, this cell design was ultimately abandoned.

3.1.2. Initial ePTFE cell design

The configuration that was designed for the ePTFE cell was very similar but simpler compared to the carbon GDE. Once again, the cell configuration consists of three main cell parts (gas, catholyte, anolyte) and a PCB for the electrical connections. In this case, no grid part is required to separate and electrically isolate the GDLs, since the ePTFE is a non-conductive material. This is very advantageous as it allows the design of a cell with far less components and only a single ePTFE GDL to support all catalysts. The ePTFE GDLs used in the current design are shown in Figure 3.1(b) and it is the PXTPX405450 type TM PTFE membrane from Pieper Filter GmbH. This membrane type has a diameter of 54 mm and the

hydrophobic PTFE side has a pore diameter of 0.45 μm. The PTFE membrane is laminated on a polypropylene fleece used as a carrier material.

In the ePTFE cell design, the gas and anolyte parts are identical to the anolyte part used in the carbon GDE design in Figure 3.6. The catholyte part is the same as the gas and anolyte parts in every regard except for the 16 holes in the middle, which run through the part to provide a pathway for the ions in the electrolyte. The cell assembly for the initial ePTFE cell design is presented in Figure 3.8:

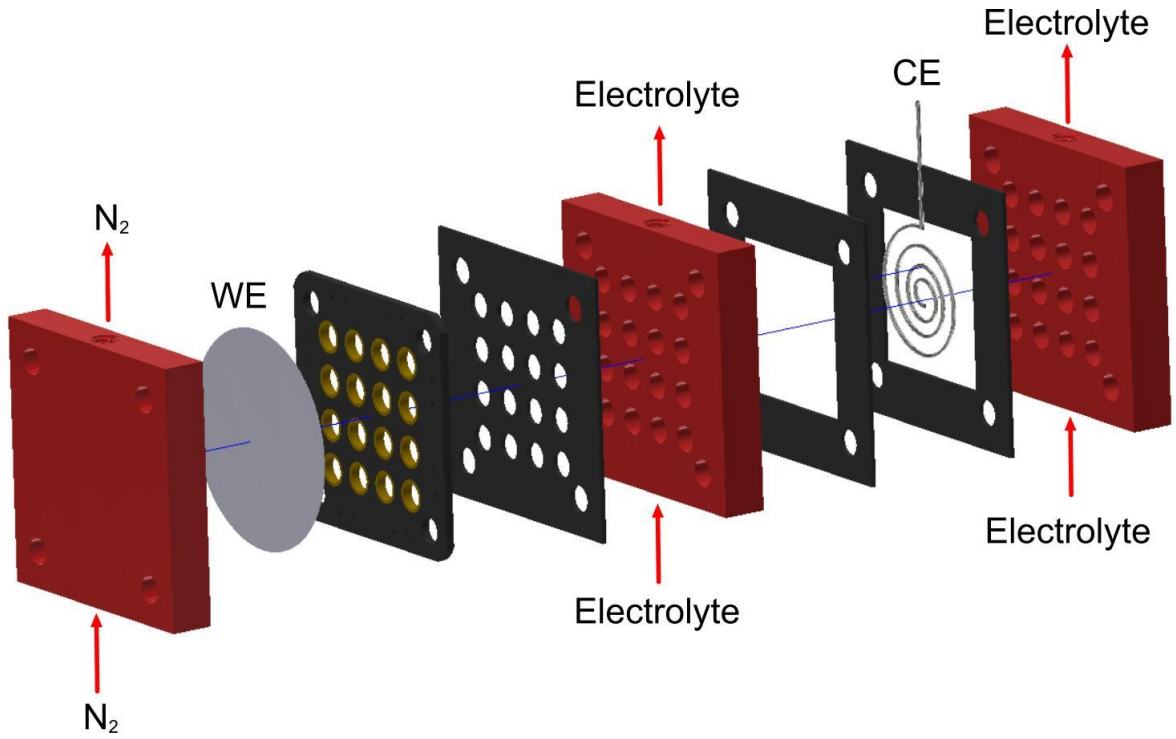

Figure 3.8. Initial ePTFE cell assembly. The parts of the cell from left to right are: gas part, ePTFE, PCB, EPDM gasket, catholyte, EPDM gasket, spiral Ni wire, EPDM gasket, anolyte. The area between the ePTFE and the anolyte is filled with electrolyte.

From the schematic in Figure 3.8 it is notable that there is no EPDM gasket present between the ePTFE and the PCB. This is because the ePTFE can provide good sealing and is also hydrophobic, preventing electrolyte from leaking between those two surfaces. Furthermore, comparing the current design with carbon GDE of Figure 3.7, it is evident that it is comprised of far fewer components, which drastically decreases the complexity and the assembly time of the ePTFE design. Overall, the initial ePTFE design was used for leakage tests and passivation experiments.

However, some problems were encountered with the initial ePTFE cell design. Gas bubbles were trapped inside the 4 channels of the catholyte and anolyte compartments. Furthermore, the ePTFE with the support fleece caused gas leakage through the sides of the cell, most likely because the polypropylene side of the fleece did not seal well. Also, the gold contacts of the PCB were in contact with the

electrolyte, which would cause them to take part in the electrochemical reactions. These problems were solved in the final ePTFE cell design that will be discussed in the following section.

3.1.3. Final ePTFE cell design

The final ePTFE cell design solved the problems encountered in the previous design and will be called from now on the high throughput cell design. This design still has three main cell parts (gas, catholyte, anolyte) and a PCB, but with additional components added in the overall cell configuration that will be explained in this section. The technical drawing of the three main parts for the HTP cell configuration is presented in Appendix A2. First of all, the gas part no longer has 4 channels connecting the 16 holes in the middle, but instead it only has a single channel creating a serpentine flow path through all 16 holes. This ensures equal flow of nitrogen to each catalyst dot. The serpentine flow is created below the surface of the gas part, allowing the holes to create 16 distinct flow paths towards the catalyst layer. The gas part design is presented in Figure 3.9:

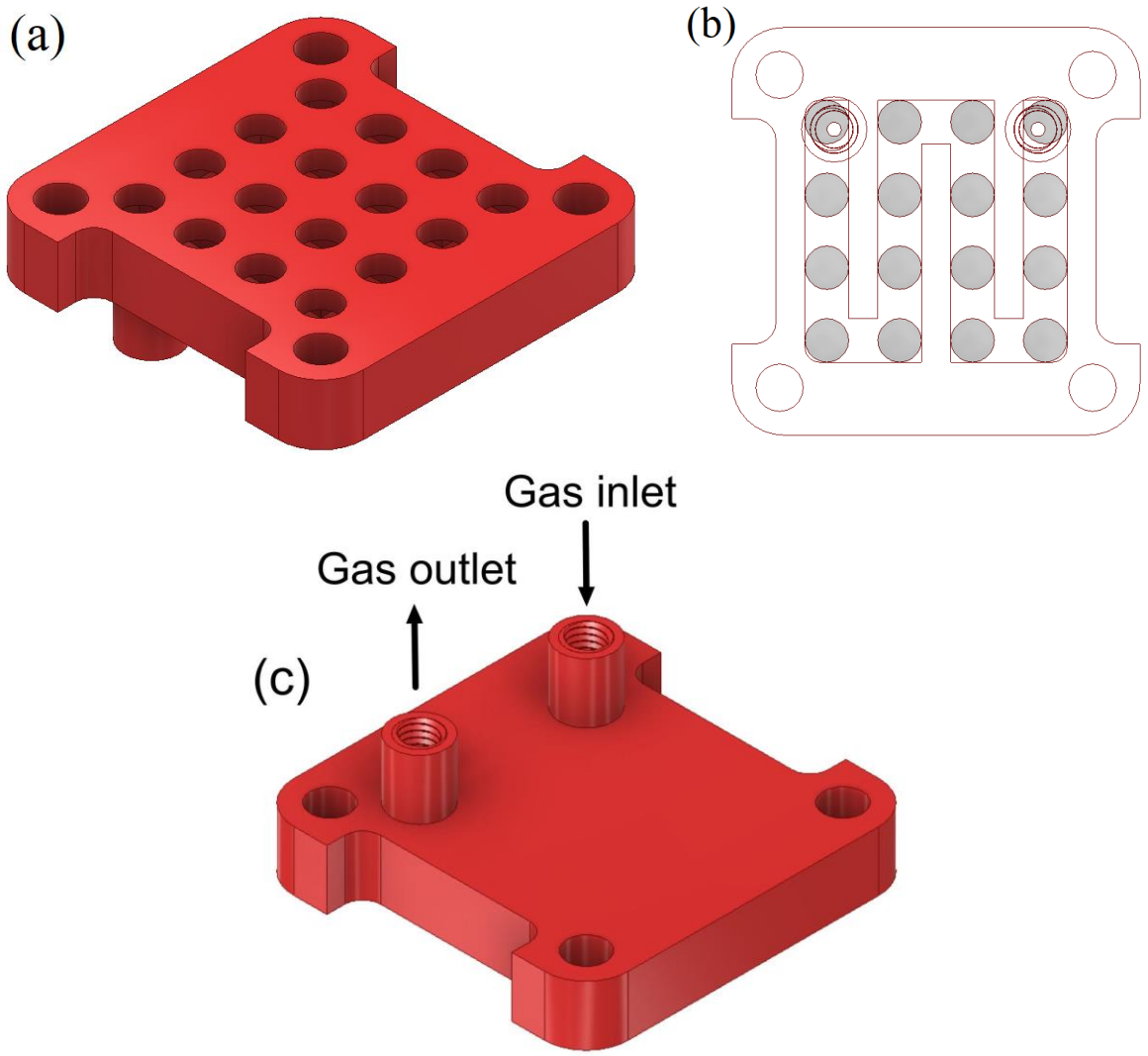

Figure 3.9. (a) 3-dimensional isometric view of the gas part. The area on the two sides of this square shape has been removed to make additional space that will accommodate the Dupont connectors of the PCB. (b) 2-dimensional top view of the gas part, showing the serpentine flow path running through all 16 holes. (c) 3-dimensional isometric back view of the gas part. Two structures with M6 threads for the connectors of the inlet and outlet of the gas are designed over the inlet and outlet of the serpentine flow path.

In Figure 3.9(c) a structure has been designed over the top left and the top right holes that is used as the inlet and outlet for the gas. This structure is a cylindrical part that contains an M6 thread and is attached to the gas part at a 90^{o} angle. An M6 connector with 1/16 inch tubing and ferrule size can be screwed to this thread to create a leak tight connection.

Next, the catholyte and anolyte compartments have been significantly changed from the previous designs. To prevent bubbles getting stuck in the channels of the catholyte and anolyte compartments as in previous designs, the 4 channels and 16 holes of these compartments have been removed. The design shown in Figure 3.10 guarantees that electrolyte will be distributed evenly across all catalyst dots on the ePTFE GDE. Furthermore, both parts are much thinner in this design, only 3 mm compared to the 10 mm of the initial ePTFE and the carbon GDE cell designs. This was necessary in order to reduce the overall volume of the electrolyte in these two parts, since it would allow for a faster detection of ammonia with NMR (see Section 3.5).

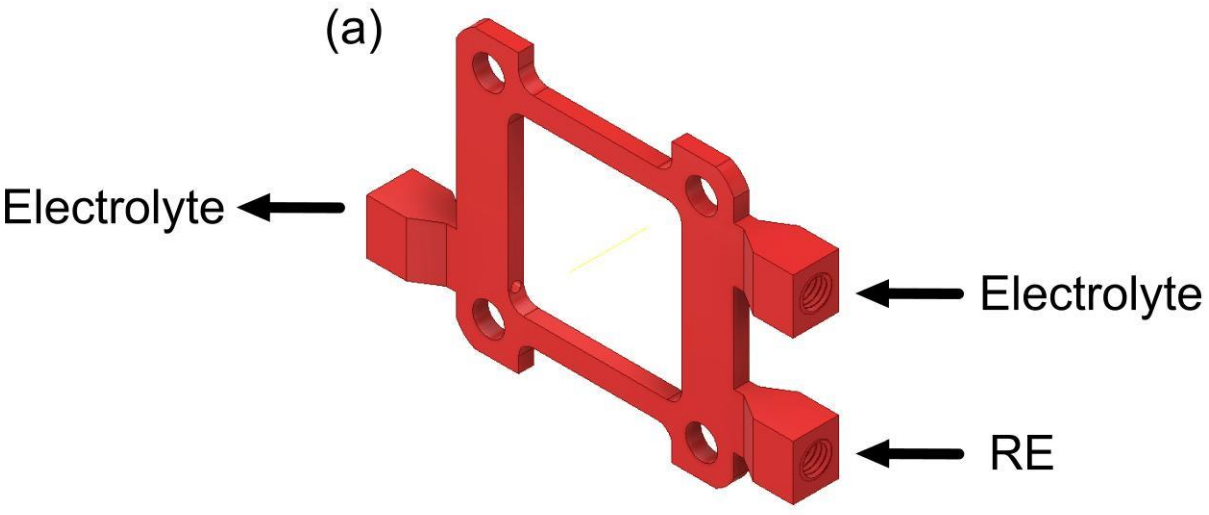

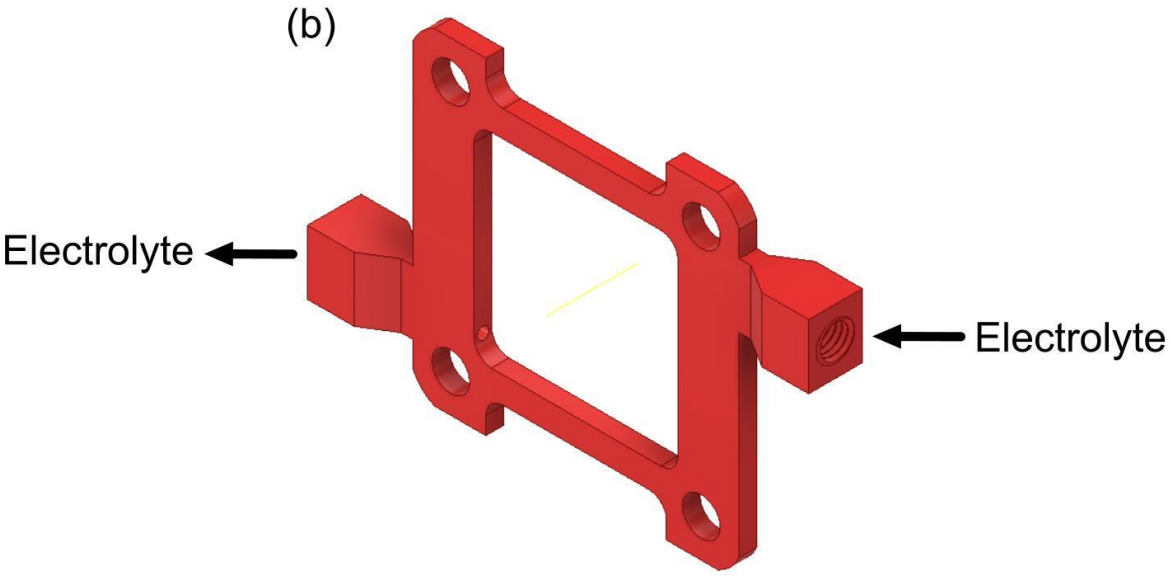

Figure 3.10. (a) 3-dimensional isometric view of the catholyte. This part has three threaded areas where connectors can be plugged in, two for the inlet and outlet of the electrolyte and one that houses the reference electrode (RE). (b) 3-dimensional isometric view of the anolyte. Only two threaded areas are required for this part, one for the inlet and one for the outlet of the electrolyte.

By placing the threaded area for the connectors on the edges of the parts, they can extend out of the main square area of the cell. In this configuration they don't block any other cell components, they make it easier for the connectors and the RE to be plugged in, but most importantly they allow for thinner catholyte and anolyte parts. After assembling the cell, the catholyte and anolyte compartments were filled with electrolyte through these connectors. Furthermore, it can be seen in Figures 3.10 (a) and (b) that a rectangular area on the top and bottom of these parts has been removed, similar to the removed area of the gas part. This was done to provide additional space for the Dupont connectors implemented in the PCB design.

For the new PCB design, it was crucial that the gold electrical contacts of the PCB were not in contact with the electrolyte. Therefore, the gold contacts that are pressed against the catalyst to electrically connect the catalyst, were placed only on the side of the PCB that was pressed against the catalysts on the ePTFE. As shown in Figure 3.11(a), the total area of the gold contacts was drastically decreased. For each one of the 16 dots of the PCB, the gold rings were replaced by 4 much smaller gold rectangles, connected by a circular wire, shown in the zoomed in image of Figure 3.11(b). Then, each wire is connected to an external contact, which have been placed only on two out of the four sides of the PCB. An array of 8 Dupont connectors is placed on each side of the PCB and then connected to a separate channel of the potentiostat. The Dupont connectors have replaced the copper tape, providing a more reliable connection between the PCB and the potentiostat and a faster assembly of the cell.

(a) (b)

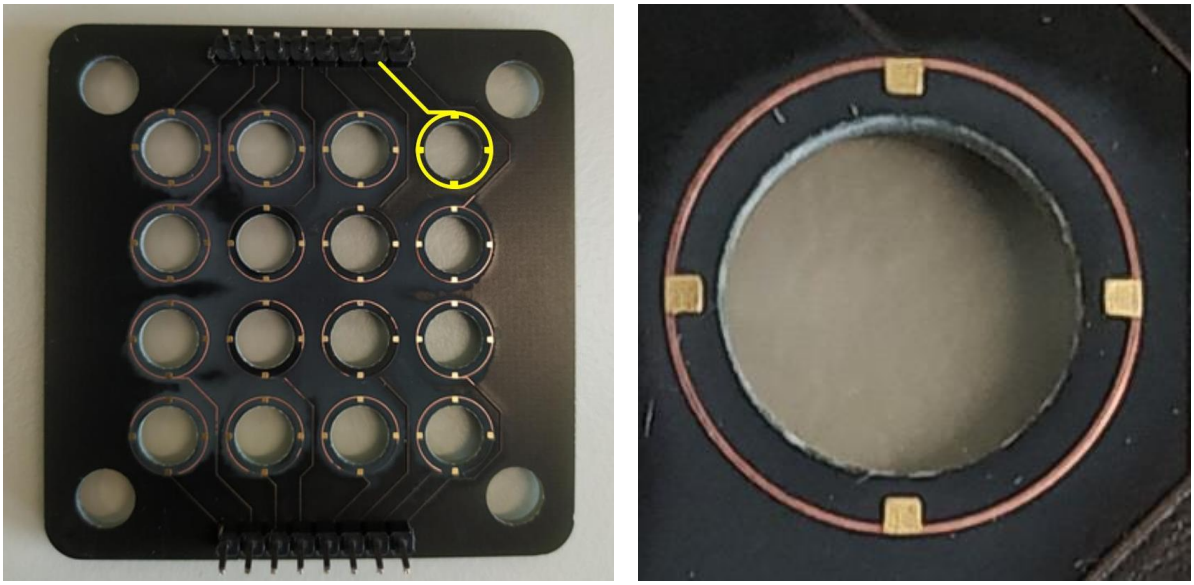

Figure 3.11. (a) Picture of the new PCB design. The yellow highlighted area shows the positioning of the 4 gold rectangular contacts and how they are connected to the external electrical contacts. This side of the PCB is in contact with the ePTFE with the catalysts while the opposite side is in contact with the electrolyte. There are no gold contacts on the opposite side of the PCB, only the black non-conductive substrate. Pin headers have been welded to the external contacts to create a reliable connection with the potentiostat. (b) Zoomed in picture of one gold contact.

For the assembly of the Dupont connectors, first a female crimp pin, shown in Figure 3.12(a), is attached to a wire using a crimping tool. Next, the female crimp pins are inserted into an array of female housing connectors, shown in Figure 3.12(b). The other side of the wire can be connected to one channel of the potentiostat. In order to connect the female housing with the PCB, the pin headers shown in Figure 3.12(c) are required. One side of the pin headers is soldered on the external contacts of the PCB, while the other is attached to the female housing with the female crimp pins. This leads to a modular configuration, where the female housing can be easily and swiftly attached to the PCB to connect and disconnect the catalysts.

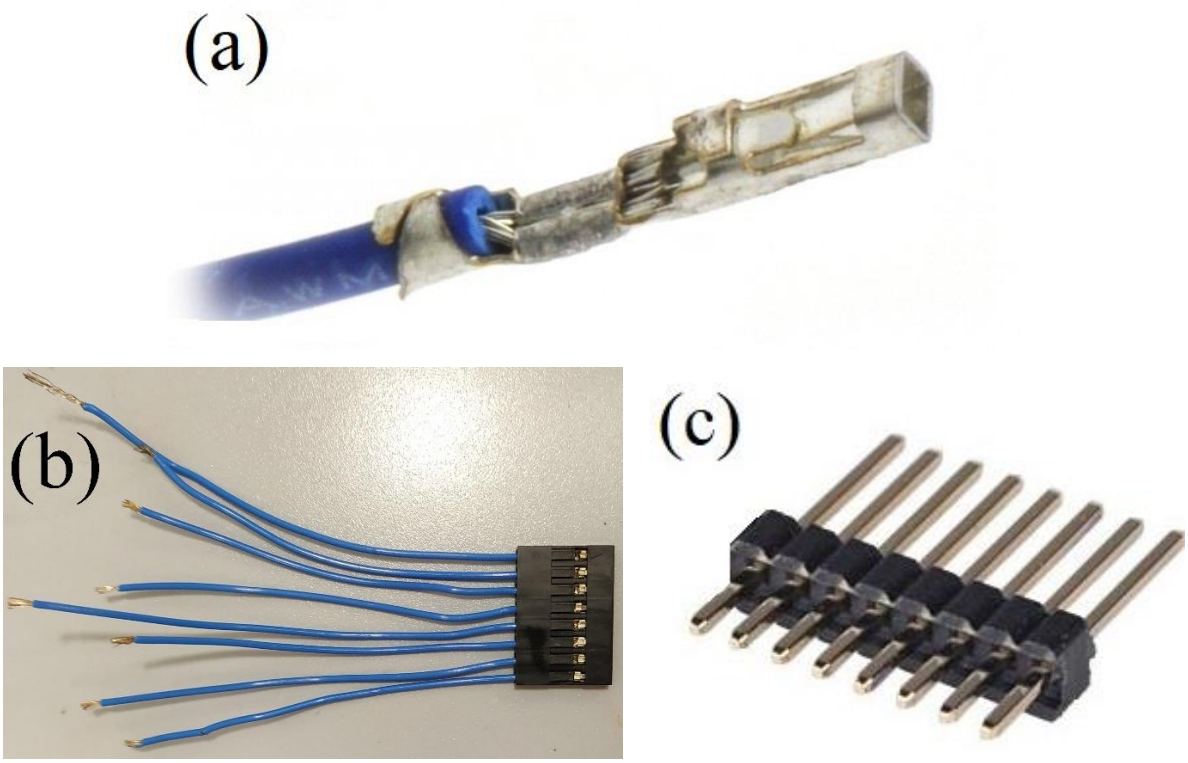

Figure 3.12. Supporting components of the PCB. (a) Female crimp pin (right) that has been attached to a wire (left). (b) Female housing connectors with the crimped wires attached to them. (c) Pin headers. The short side is welded to the PCB, while the long side is connected to the female housing connectors.

A 0.25 mm nickel wire from MaTecK was used as a counter electrode. The Ni wire is positioned between two rubber EPDM gaskets and placed inside the anolyte compartment. As shown in Figure 3.13(a), the Ni wire was bent into a spiral shape to provide a larger surface area for the electrochemical reaction (oxygen evolution for the NRR experiments) to occur on it. The catholyte and anolyte compartments were separated by a Zirfon Perl UTP 500 membrane from AGFA, shown in Figure 3.13(b). The main purpose of the Zirfon membrane is to separate the liquid electrolyte of the catholyte and anolyte compartments and only allow the transfer of ions between them. The Zirfon membrane is a good choice for this cell configuration, due to its high chemical stability in alkaline environments, mechanical stability and very low ionic resistance [34].

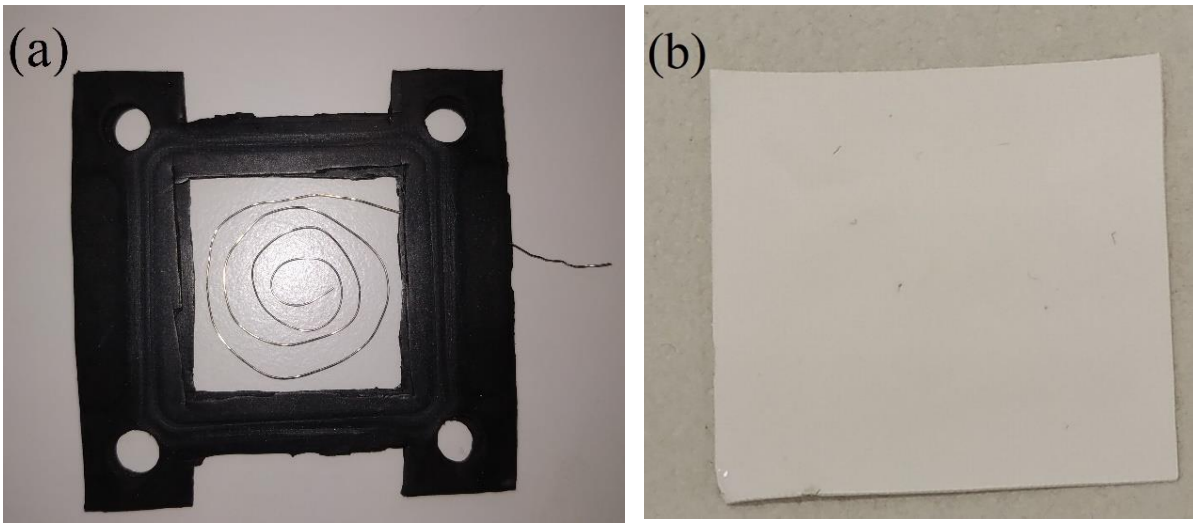

Figure 3.13. (a) Picture of the spiral Ni wire between two gaskets. The CE is connected to the potentiostat through the part of the Ni wire to the right that extends outside of the cell. (b) Picture of the Zirfon membrane that separates the catholyte from the anolyte.

Having looked into each of the main cell parts in detail, the high throughput cell design along with all of the supporting components will be displayed in Figure 3.14:

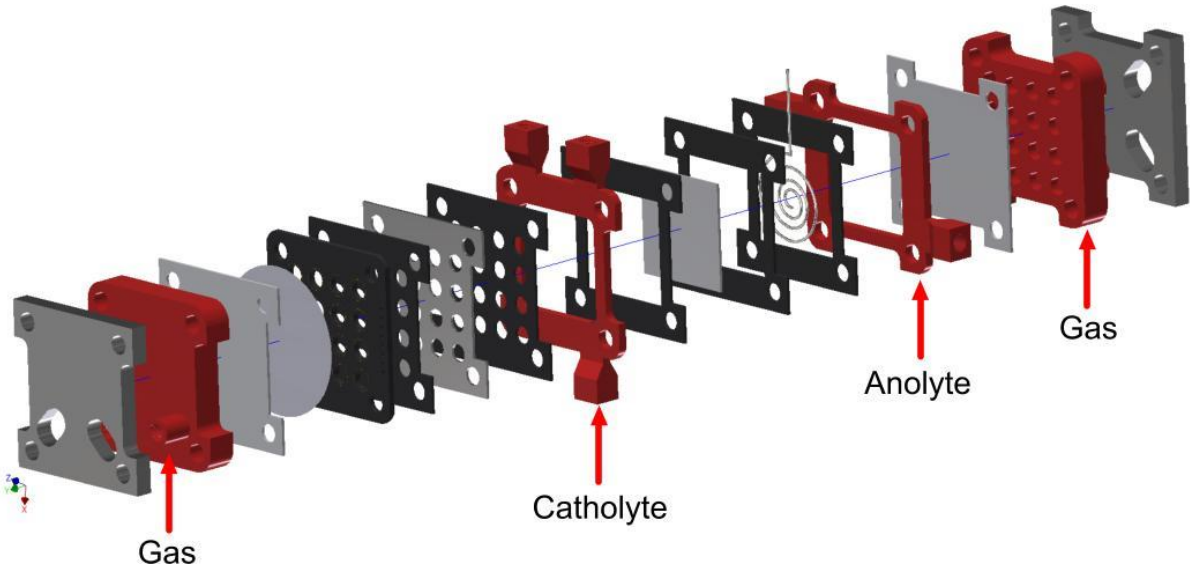

Figure 3.14. Expanded view of the high throughput cell design. From left to right, the parts that comprise the cell are: (1) stainless steel end plate, (2) gas part, (3) ePTFE gasket, (4) pure ePTFE with catalysts, (5) PCB, (6) EPDM gasket, (7) stainless steel plate, (8) EPDM gasket, (9) catholyte part, (10) EPDM gasket, (11) Zirfon membrane, (12) EPDM gasket, (13) spiral Ni wire, (14) EPDM gasket, (15) anolyte part, (16) ePTFE gasket, (17) gas part, (18) stainless steel end plate. The area between the pure ePTFE on the left and the ePTFE gasket on the right is filled with electrolyte.

The high throughput cell assembly in Figure 3.14 has a total of 18 components. First of all, this cell configuration includes two gas parts, one on the far right and one on the far left of the configuration. The gas part on the left is responsible for transferring the reactant gas (N_2) to the GDL and onto the catalysts, while the gas part on the right acts as an exit for oxygen produced at the anode. During the NRR experiments, oxygen evolution reaction (OER) occurs at the surface of the Ni wire, causing bubbles to form on it. The second gas part placed on the right side of the cell creates a pathway for the accumulated gas in the anolyte to escape out of the anolyte.

A stainless steel endplate is placed on each side of the cell to distribute the clamping force more equally across the cell, which improves sealing. The stainless steel end plates also prevent the bolts and the washers of the screws from damaging the 3D printed cell parts.

Next, a 1 mm thick ePTFE gasket, supplied from GORE® GR Sheet Gasketing, is placed on both gas parts. This layer - henceforth called thick ePTFE – prevents N_2 leakage through the sides of the cell, something that was an issue with the backed ePTFE. It also prevents flooding of the gas part effectively. At the same time, it allows gas to diffuse through the thick ePTFE towards the catalyst layer. EPTFE is also a sealing material so no additional EPDM gaskets are required between these parts. Furthermore, the thick ePTFE piece solved the passivation problem of the gold contacts of the PCB, but this effect will be discussed in detail in Section 4.5.

Following the thick ePTFE, the round pure ePTFE with the catalysts is placed directly on top of it. The backed ePTFE of the previous cell design was replaced with the PXSUX205450 pure ePTFE from Pieper Filter GmbH. This ePTFE has the same diameter as the backed ePTFE (54 mm), but it doesn't have a support fleece, instead it consists of 100% ePTFE, which minimizes N_2 leakage outside the cell. A 1 mm thick stainless steel plate is placed between the catholyte part and the PCB to provide a more equal force distribution over the entire area of the PCB, which is necessary for the passivation of the electrical contacts. EPDM rubber gaskets are placed on each side of the stainless steel plate to prevent electrolyte leakage. This configuration was the high throughput cell design that was used to conduct all of the electrochemical experiments presented in Section 4, except for the passivation experiments.

3.2. Experimental setup

The experimental setup consists of the high throughput cell, the potentiostat and is completed with the addition of the mass flow controllers (MFCs). Nitrogen is supplied to the gas parts of the cell from a wall socket, making it difficult to accurately control the flowrate of the gas. To this end, two Bronkhorst EL-FLOW® Prestige mass flow meters/controllers were used in this project to control the flowrate of the two gas streams entering the cell. The flowrate of both MFCs was set to 1.2 mL/min. The schematic of the complete experimental setup can be seen in Figure 3.15:

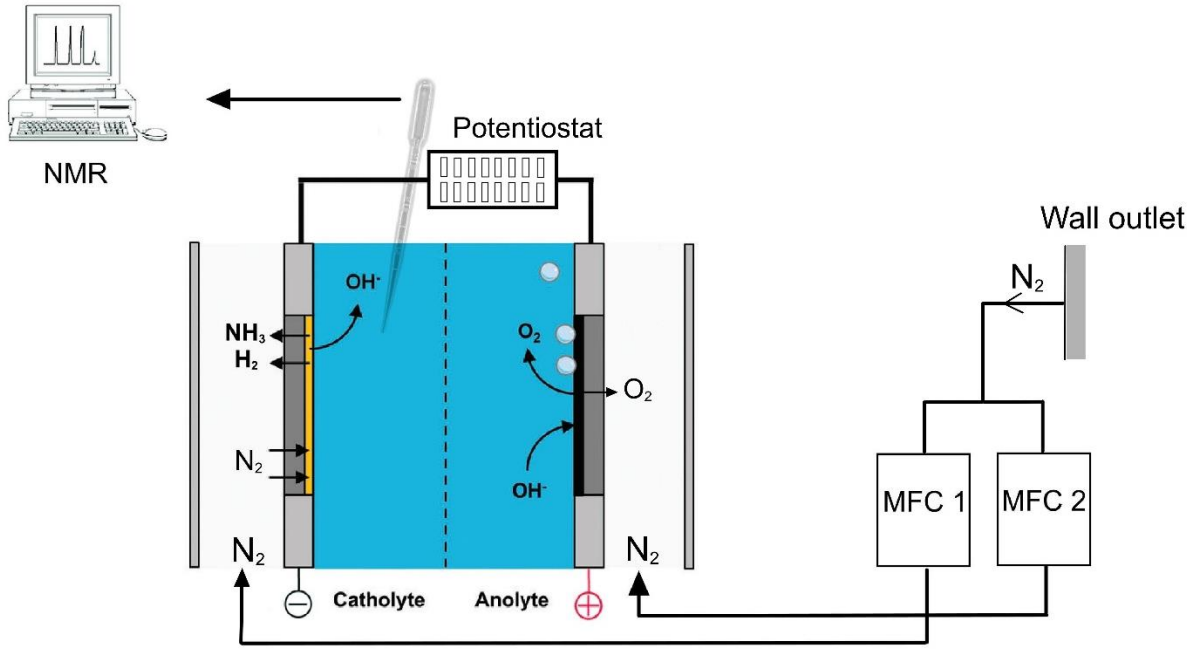

Figure 3.15. Schematic of the overall experimental setup. Nitrogen is supplied to the MFCs from a wall outlet and then enters the two gas compartments of the cell. The current applied to the cell is controlled with the Arbin potentiostat. NRR and HER can occur on the catalyst surface inside the catholyte compartment, while OER occurs on the Ni CE surface in the anolyte compartment. Any NH_3 produced on the catalyst surface can diffuse back into the gas part or inside the electrolyte in the catholyte compartment. Liquid samples can be taken from the electrolyte and analyzed in NMR to detect any NH_3 production. In this configuration, 16 different WEs are used, each one connected to a separate channel of the potentiostat.

The four main parts of the cell can be seen in Figure 3.15: the gas part where N_2 is introduced at their inlet, the catholyte and the anolyte. The PCB and the ePTFE with the catalysts are placed between the gas part on the left and the catholyte. NRR and HER can occur on the catalyst surface and OER occurs on the spiral Ni wire in the anolyte. These reactions were presented in Eq. (2.1)-(2.3). The NH_3 produced on the catalyst surface can either escape back into the gas part or diffuse inside the electrolyte of the catholyte compartment. NH_3 in the electrolyte was detected with NMR by taking liquid samples. The O_2 produced in the anolyte can diffuse through the ePTFE and into the right gas part, escaping the cell.

3.2.1. Chemicals

Acetone (99%) and 2-propanol (99.8%) from VWR chemicals were used during the cleaning process of the glass slides for the sputtering of the metal catalysts (see Section 3.5). Potassium hydroxide (KOH) solution, 45 wt.% in H_2O was purchased from Sigma Aldrich. 95% sulfuric acid (H_2SO_4) was also

supplied from Sigma Aldrich. $^{14}NH_4Cl$ (99.995%), maleic acid (≥ 99 %) and H_2SO_4 (≥ 97.5%) were obtained from Sigma Aldrich. Gadolinium(III) nitrate hexahydrate (99.9%) was obtained from Fisher Scientific. DMSO-d_6 (99.9% D, 0.03 % V/V Tetramethylsilan was obtained from Cambridge Isotope Laboratories. Ultrapure water from a Milli-Q® Advantage A10 water purification system was used when diluting the solutions and during the cleaning procedures (resistivity: 18.2 MΩ at 25 °C). An RS modified silicon conformal coating aerosol was used to coat the surface of the PCB with a passivated layer.

3.2.2. Electrochemical measurements

The first step for conducting a typical electrochemical experiment was the assembly of the high throughput cell. The components of the cell are stacked on top of each other in the same order as shown in Figure 3.14, starting with the stainless steel end plate on the left and ending with the stainless steel plate on the right. Next, the catholyte and anolyte compartments are filled with 0.1 M KOH electrolyte and the connectors of these parts are sealed. An Arbin Instruments BT-2000 multichannel potentiostat was connected to each of the 16 distinct external electrical contacts of the PCB. Each channel of the potentiostat has four cables, which are connected in a specific way to the pins of the channel connector shown in Figure 3.16(a) to implement a 3-electrode configuration. Based on Figure 3.16(b), the red and white wires have to be connected to the working electrode (WE), the green wire to the reference electrode (RE) and the black wire to the counter electrode (CE). Figure 3.16(c) shows a configuration where seven channels are connected to seven WEs, but only one RE and one CE.

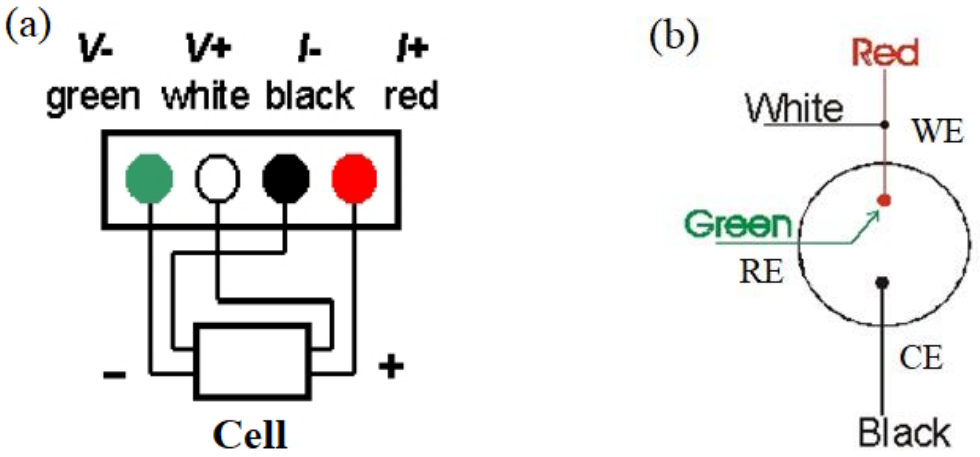

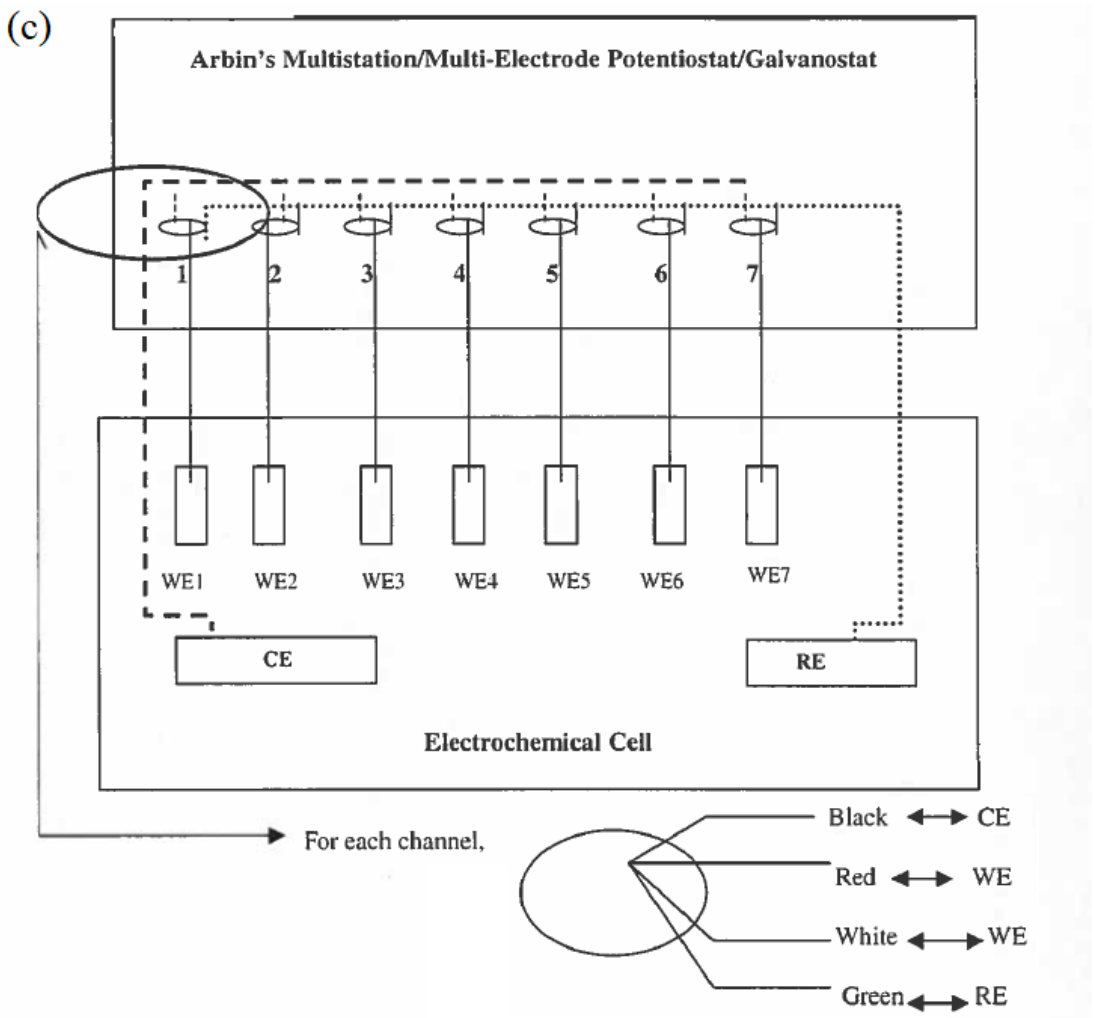

Figure 3.16. Schematics from the manual of the Arbin Instruments BT-2000 potentiostat. (a) Cable color for each of the 4 pins of a channel. (b) Connection of the red and white cables to the WE, the green cable to the RE and the black wire to the CE. (c) Schematic of seven channels of the Arbin potentiostat. Each of the channels is connected to a different WE, but all channels are connected to a single RE and a single CE.

It should be noted that the RE is placed as close to the WE as possible to minimize the Ohmic drop or IR drop [35].

The connections of each external contact of the PCB for the high throughput cell were created based on the information of the three schematics in Figure 3.16. The 16 WEs of the high throughput cell are the catalyst dots that are in contact with the gold contacts of the PCB. A Mini HydroFlex® hydrogen reference electrode with a 2 mm diameter probe that could be plugged into the cell from one of the connectors of the catholyte part was used. The CE in the high throughput cell was the spiral Ni wire.

The type of experiments that were conducted with this setup were chronopotentiometry experiments, where a constant current is applied and the response of the potential is recorded. For a typical electrochemical experiment, a current of -500 μA is applied to each channel of the cell for 1 h. The choice of this value for the applied current was twofold. First, since the HER is favored on most

catalyst surfaces over the NRR, a lower applied current will limit the amount of current going towards the HER and consequently increase the FE. The second reason for the choice of -500 μA current is due to the quantification limit of the NMR, which is discussed in Section 3.5.

When an experiment was concluded, a cleaning procedure was implemented to prevent any NH_3 and NO_3^- leftovers of the current experiment carrying on to future experiments. The cleaning procedure involved the following steps [36]:

i) 20 min sonication in 0.5 M H_2SO_4
ii) 20 min sonication in 0.5 M KOH
iii) 20 min sonication in ultrapure water
iv) storage in ultrapure water

3.3. Characterization methods

The physical characterization methods that were utilized during this project are Scanning Electron Microscopy (SEM) and X-ray Diffraction (XRD). SEM was performed on a JEOL JSM-6010LA scanning electron microscope with fully integrated Energy-Dispersive X-ray spectroscopy (EDS). In this project SEM was used to image the surface of the catalysts on the ePTFE, while EDS would reveal the elemental composition of the catalysts. XRD was performed on a Bruker D8 DISCOVER diffractometer with a Cu K-alpha$_1$ and K-alpha$_2$ radiation source. This method was used to determine the crystal structure of the catalysts.

3.4. Detection methods

Gas Chromatography (GC) and Nuclear Magnetic Resonance (NMR) spectroscopy were used to quantify ammonia. GC was performed on a ThermoScientific Trace 1300 gas chromatograph, allowing to detect any NH_3 that diffuses into the gas part after being produced on the catalyst surface. H NMR spectra were acquired on a 400 MHz pulsed Fourier transform NMR spectrometer equipped with an autosampler. An autotunable temperature regulated Agilent OneNMR room temperature probe was used for all measurements. The temperature was set to 25 ^oC and the receiver gain was optimized automatically. The pulse sequence that was used in this work is: Excitation Sculpting (vNMRj: ‘waterES’). The waterES pulse sequence has the following structure:

Water ES: d1-P90-G1-S180-G1-G2-S180-P180-G2-aq

where G1 and G2 are z-gradients of different strengths, P90, P180 are hard pulses and S180 is a selective 180^o pulse. The z-gradients G1 and G2 had a duration of 1 ms and a strength of 1.7 G cm^{-1}. The 180° selective pulses had the shape "Wsupp" with a width of 2.5 ms and a power of 13dB.

3.5. Ammonia detection

As discussed in Section 3.2, the current that was applied to the cell was -500 μA. This value was selected based on the quantification limit NH_3, which is at 0.5 ppm (parts per million). This means that a higher concentration of NH_3 than 0.5 ppm should be present in the sample taken from the electrolyte after the experiment to be able to detect it and accurately quantify it in the NMR. This value corresponds to a 20.8 NH_3 μmol for a 10 min analysis time and a minimum signal-to-noise of 20. The number of moles produced during an electrochemical reaction can be calculated from Faraday's law shown in Eq. (3.1):

$$n = \frac{I\,t}{z\,F} \tag{3.1}$$

where n (mol) is the number of moles of NH_3 produced during the reaction, I (A) is the applied current, t (s) is the duration of the experiment, z is the number of protons transferred during the reaction and F (C mol^{-1}) is the Faraday constant, equal to 96485 C mol^{-1}. The number of protons taking part in the reaction per ammonia molecule is 3, the applied current is -500 μA and the during of the experiment is 3600 s. For these values and assuming a FE of 10% for a good NRR catalyst [8], the amount of ammonia produced is calculated to be $6.22 \cdot 10^{-7}$ mol per catalyst. Considering that 16 catalysts are tested at the same time, the total amount of NH_3 produced in the cell is $9.95 \cdot 10^{-6}$ mol.

Next, the mole fraction of NH_3 in the electrolyte is calculated. The total volume of the catholyte and anolyte compartments that can be filled with electrolyte is 10 mL. Ppm refers to the amount of a substance diluted inside a solution per 1 million parts of that solution. The 0.1 M KOH can be considered to have a molecular weight and density very close to the values of water, therefore MW_{KOH} = 18 g mol^{-3} and ρ_{KOH} = 1000 kg m^{-3}. With these values, the total amount of NH_3 present in the electrolyte is calculated as shown in Eq. (3.2):

$$\frac{C_{NH_3}}{C_{H_2O}} = \frac{\frac{n_{NH_3}}{V_{KOH}}}{\frac{n_{H_2O}}{V_{H_2O}}} = \frac{n_{NH_3}\,MW_{H_2O}}{\rho_{H_2O}\,V_{KOH}} = 17.9 \text{ ppm } NH_3 \tag{3.2}$$

The amount of NH_3 produced during a 1-hour long experiment is higher than the detection limit of the NMR, resulting in an accurate way to detect any potential NH_3 produced in the cell.

In a typical experiment, 525 μL of sample was mixed with 50 μL 0.5 M H_2SO_4, 50 μL DMSO-d_6, 25 μL 12.5 mM maleic acid and 25 μL 27 mM Gd^{3+} solution inside an eppi. 600 μL of this solution was transferred into a 5 mm thin wall NMR tube (Wilmad). NMR tubes were closed with Norell Sample Vault NMR tube caps (Sigma Aldrich). NMR tubes were cleaned with ultrapure water and ethanol using

an NMR tube cleaner. After cleaning, the NMR tubes were dried at 60 ºC for 1 h and stored in a dust-free environment.

Following is the procedure to calculate the FE of each injection for the NO_3^- reduction experiments that will be discussed in Section 4.6.6. The number of nitrogen moles, n_{N_2}, that enters the cell in every injection is calculated based on the ideal gas law shown in Eq. (3.3). The amount of nitrogen that reaches the GC is 1 mL/min and an injection occurs once every 6 min, therefore, the number of moles of nitrogen that reach the GC per injection is $2.45 \cdot 10^{-4}$ mol. Knowing the ppm of NH_3 in every injection, the moles of NH_3 produced, $n_{NH_3,\,measured}$, can be calculated from Eq. (3.4). Then, the maximum NH_3 that can be produced, $n_{NH_3,\,max}$, for the applied current is calculated based on Faraday's law, shown in Eq. (3.1). When applying Faraday's law, it should be noted that z=8 for NO_3^- reduction instead of z=3 that is used for N_2 reduction. Finally, the FE for each injection is calculated by dividing the measured NH_3 moles with the maximum NH_3 moles that can be produced, as shown in Eq. (3.5).

$$n_{N_2} = \frac{P\,V_{N_2}}{R\,T} \tag{3.3}$$

$$n_{NH_3,\,measured} = n_{N_2} \cdot ppm_{NH_3} \tag{3.4}$$

$$FE\,\% = \frac{n_{NH_3,\,measured}}{n_{NH_3,\,max}} \cdot 100 \tag{3.5}$$

3.6. Sputtering

Bimetallic catalysts were prepared by magnetron sputtering on an AJA International ATC 2400 sputtering system. Magnetron sputtering is a Physical Vapor Deposition (PVD) process that takes place under vacuum and it is used for the deposition of thin film of materials on a substrate. In sputtering an inert gas like argon is heated up to form a gaseous plasma. Then the charged ions of the plasma are bombarded on the surface of a source material (target). Due to the collision, some atoms of the target material are ejected from its surface and can be deposited on a substrate opposite of the target. The continued effect of this process leads to the deposition of a thin film of the target material on the substrate [37]. More than one targets can be active at the same time, allowing for the deposition of binary alloys on the substrate.

When two metals are sputtered simultaneously, every spot on the substrate will have a unique composition. To understand how this is achieved, first the schematic of the sputtering chamber will be presented. As shown in Figure 3.17(a), the sputtering chamber consists of four targets in a circular formation and a sample holder in the middle. The sample is positioned 15 cm above the targets during the deposition process. The substrate that the sputtered metals are deposited on is a pure ePTFE sample.

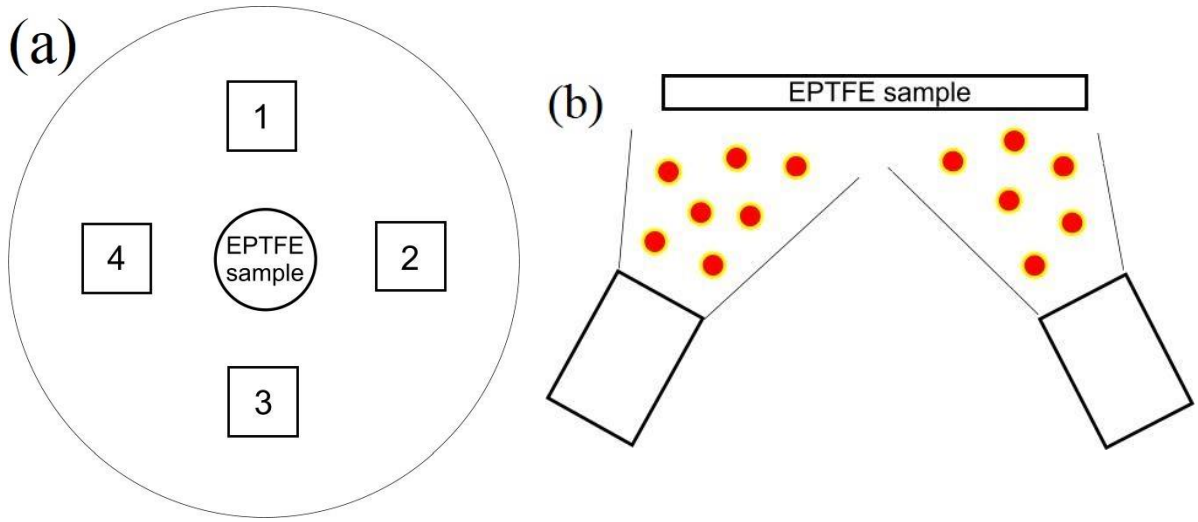

Figure 3.17. (a) Top view representation of the sputtering chamber. Four targets of different materials are placed in a circular formation around the sample holder in the middle. The pure ePTFE and a mask are placed on the sample holder in the middle, which is located at a deposition height of 15 cm. (b) Side view representation of the sputtering chamber during the deposition process. The ejected material from the targets is deposited in a cone-shaped area opposite to the target.

As shown in Figure 3.17(b), the ejected atoms of the targets travel in a cone-shaped area opposite to the targets, until they reach the ePTFE substrate. The highest deposition rate occurs closer to each target. As a result, each spot of the ePTFE sample will have a different deposition thickness.

In this project, the substrate was initially the backed ePTFE but for the majority of the depositions the pure ePTFE was used. The ePTFE piece was placed on a sputtering sample holder and a thin stainless steel foil was placed on top of it to act as a mask. The mask shown in Figure 3.18(a) has a thickness of 0.2 mm with an 8 mm hole diameter. The thickness of the mask was low to prevent any ‘shadow’ effects towards the edges of the dots, where metals were not easily deposited due to the angle of the target and the substrate. Sputtering the bimetallic catalysts on the pure ePTFE with the mask creates a sample as shown in Figure 3.18(b), which is the GDL with 16 distinct catalyst layers that are electrically isolated from each other.

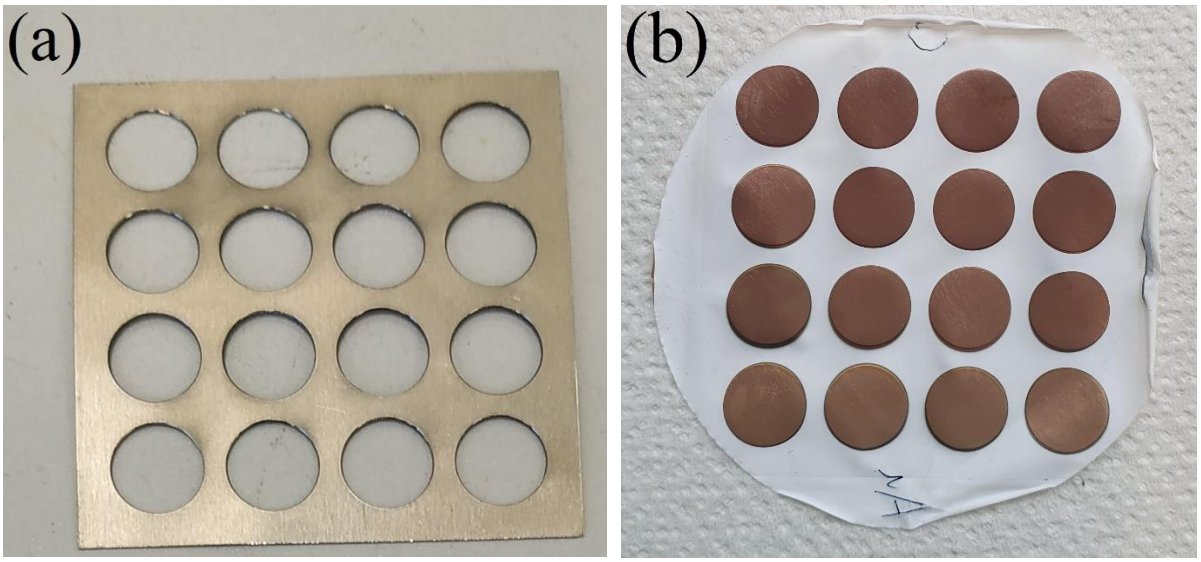

Figure 3.18. (a) Stainless steel mask that is placed on the pure ePTFE substrate. (b) Pure ePTFE substrate with 16 catalyst dots sputtered on it. The catalysts on this sample are binary alloys of Cu and Au.

By measuring the thickness of the deposited metal on different points of the surface of the sample, we can predict the composition of all 16 alloys of Figure 3.18(b). This is a very useful tool, as it provides an indication of the extent of the catalyst compositions that can be created without spending additional time and resources to test those samples in EDS.

First, the tilt angle of the targets shown in Figure 3.17(b) affects the amount of material deposited on the substrate. Since the deposition thickness decreases as the distance between the target and the sample increases, the largest difference between the left and the right side of the sample will occur when the target is facing directly upwards (tilt angle = 1). Every deposition carried out during this project had a tilt angle of 1 for each target to maximize the range of compositions that were created.

To calibrate the thickness of the sputtered metal gradient, the metal was first deposited on a ThermoScientific microscope glass slide, since it offered a flat surface where the thickness of a thin film could be accurately measured. The measurement of the thickness of the deposited metal thin film on the surface of the glass slide is conducted on a Dektak 3 surface profilometer. Before the sputtering process, the glass slide was sonicated for 5 min in acetone and then for 5 min in 2-propanol to remove any dust particles that could be stuck on its surface. After the sputtering process, the thickness of the metal thin film was measured in four spots that correspond to the position of the catalyst dots in Figure 3.18(b). A schematic of the glass slide on the sample holder after the sputtering process is shown in Figure 3.19:

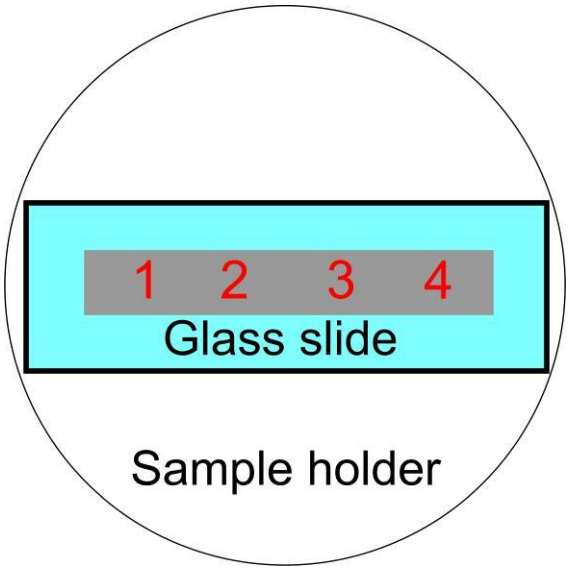

Figure 3.19. Schematic of a glass slide after the sputtering process on a sample holder. The light blue area represents the glass slide while the grey area represents a metal that has been sputtered on it. The thickness measurements are conducted on the 4 numbered areas on the glass slide. The distance between each numbered spot is 10 mm, which is the same value as the distance between the centers of the catalyst dots on the same row or column of Figure 3.18(b).

3.7. Composition calculator

The composition calculator is a MATLAB tool that was created to predict the power settings of the targets to achieve a desired composition at the center of the PCB. The deposition rate of the metal at the middle of the glass slide, Tooled Rate (TR, Å/s), is calculated by dividing the average value of the four measured thickness values with the deposition time. This provides the so-called tooling data for a specific metal. The deposition thickness also depends linearly on the power supplied to the target. If the power of the power supply connected to the target is doubled, then the deposition thickness of the material on the substrate will also double. The power value set to the power supply during the tooling is called Tooled Power (TP, W). Additionally, the molar volume, V_m ($m^3\ mol^{-1}$), of each material is known. The wish rate (WR, Å/s) is the new deposition rate of a metal that is required to achieve the desired composition. For a set power value and tooled rate of the first target, the power setting and the wish rate of the second target can be calculated based on Eq. (3.6)-(3.7):

$$WR_2 = \frac{TR_1 \cdot Comp_{2,\,middle} \cdot MV_2}{Comp_{1,\,middle} \cdot MV_1} \tag{3.6}$$

$$P_2 = \frac{WR_2 \cdot TP_2}{TR_2} \tag{3.7}$$

where $Comp_{1,\ middle}$ and $Comp_{2,\ middle}$ (%) are the desired composition values at the middle of the PCB of the first and second metal respectively, MV_1 and MV_2 are the molar volumes of the two metals, TR_1 and TR_2 are the calculated tooled rates at the center of the glass slide for each metal, WR_2 is the deposition rate of the second metal required to achieve the desired composition, TP_2 is the tooled power of the second metal and P_2 is the power value set to the power supply of the second target. For a desired total deposition thickness at the middle of the glass slide, d_{middle} (Å), the duration of the deposition of the two metals, t (s), is given by dividing the desired thickness with the total thickness deposited at the center of the glass slide, as shown in Eq. (3.8):

$$t = \frac{d_{middle}}{TR_1 + WR_2} \tag{3.8}$$

The first part of the composition calculator reduced the amount of time required to prepare for the sputtering of the bimetallic alloys by providing the power settings and the deposition time necessary to achieve a desired composition. The second part of the composition calculator predicted the composition of each one of the 16 bimetallic catalysts deposited on a substrate.

The composition of the catalyst dots on the pure ePTFE substrate depends on the position of the targets in the sputtering chamber. Based on the schematic of Figure 3.17(a), the targets of the sputtered materials can either be opposite each other at a 180^o angle (targets 1 and 3), or they can be at a 90^o angle (targets 4 and 1). This creates two possible distributions of the composition of the sputtered metals. The calculations for the 180^o angle case will be presented here. The first step is to calculate the thickness that will be deposited on each catalyst dot of a sample. The targets, the glass slide and the sample are located opposite each other, as shown in Figure 3.20. Catalyst dots that are located in the same row will have the same deposited thickness with the corresponding numbered spot on the glass slide, while the composition will be different for dots on the same column.

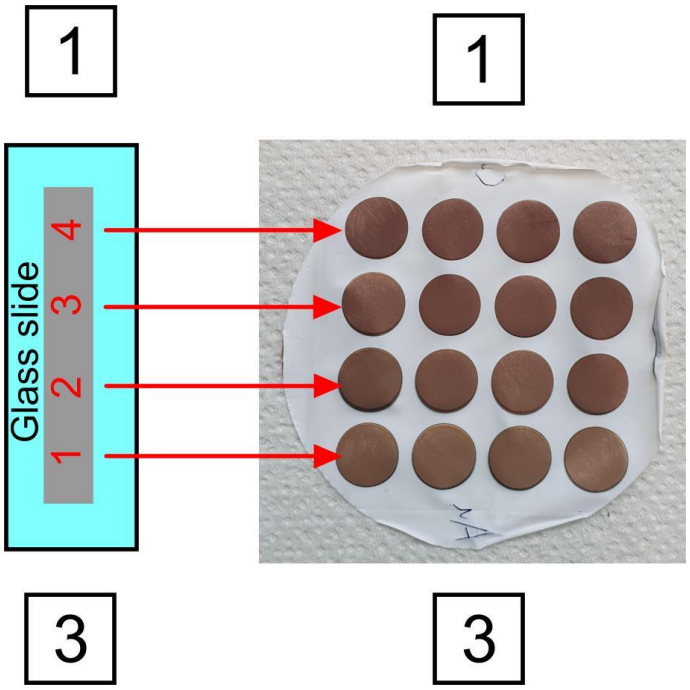

Figure 3.20. Schematic of the glass slide with respect to the sputtered sample. Each numbered spot on the glass slide will have the same thickness as each catalyst dot located on the same row. Targets 1 and 3 are located opposite each other at a 180° angle.

The thickness of each metal, d (Å), that is deposited on the pure ePTFE substrate depends linearly on the power setting of each target and the sputtering duration during the tooling process, $t_{tooling}$ (s), for each metal. The deposited thickness of each metal on the pure ePTFE substrate is calculated based on Eq. (3.9)-(3.10):

$$d_1 = d_{1,\,tooling}\,\frac{t}{t_{1,\,tooling}} \tag{3.9}$$

$$d_2 = d_{2,\,tooling}\,\frac{P_2 \cdot t}{TP_2 \cdot t_{2,\,tooling}} \tag{3.10}$$

where $d_{1,\,tooling}$ and $d_{2,\,tooling}$ are the measured thickness values from the tooling data for the first and second metal respectively. Finally, the composition of the catalyst dot can be calculated from Eq. (3.11)-(3.12):

$$Comp_2 = \frac{100 \cdot d_2 \cdot MV_1}{d_1 \cdot MV_2 + d_2 \cdot MV_1} \tag{3.11}$$

$$Comp_1 = 100 - Comp_2 \tag{3.12}$$

where $Comp_1$ and $Comp_2$ (%) are the compositions of the first and second metal respectively for one row of catalyst dots. The same procedure can be repeated three times to calculate the composition of the

catalyst dots on the remaining three rows of the sample. The same calculations apply to the case where the targets are placed at 90°. However, they have to be conducted 16 times, since in this case every catalyst dot will have a unique composition. The MATLAB code that was compiled to do this process for both cases can be found in Appendix A1.

3.8. Design of experiments

Before starting the sputtering of bimetallic catalysts, it was important to choose which metals would be sputtered, as there are countless combinations. We choose for the start to focus on catalysts that are active NRR catalysts, based on previously published literature data. The alloys presented in Table 3.1 show promising NRR activity. The reported FE as well as the NH_3 yield rate ($\mu g\ h^{-1}\ mg_{cat}^{-1}$) are shown for each bimetallic catalyst. From those we chose Pd_3Cu_1, PdRu, Ag_3Cu, AuCu and FeW, since these alloys could be produced by magnetron sputtering. Additional alloys that were not mentioned in literature were also created. These alloys included AuAg, AuRu, CuRu and AuPd.

Table 3.1. Single metals and bimetallic catalysts reported in literature to have good NRR activity. The FE and the NH_3 yield rate are also presented for each of the cited catalysts.

Catalyst	FE (%)	NH_3 yield rate ($\mu g\ h^{-1}\ mg_{cat}^{-1}$)	Reference
Pd_3Cu_1	1.22	39.9	[38]
PdRu	1.53	25.92	[39]
Ag_3Cu	13.28	24.59	[40]
AuCu	54.96	154.91	[41]
Cr_2O_3	7.33	33.3	[42]
VO_2	3.97	14.85	[43]
Mo_2C	8.13	95.1	[44]
Fe-doped $W_{18}O_{49}$	20.0	24.7	[45]
CoP	7.36	2.485	[46]
Au film on Ni foam	13.36	9.42	[47]
Au on TiO_2	8.11	21.4	[48]
Ru on ZrO_2	21	3.665	[49]

4
Results and discussion

This section will focus on the experimental results and the process of validating the high throughput cell. First, the SEM images of the sputtered catalysts on the pure ePTFE substrate will be presented, along with the XRD patterns of the catalysts. Next, the techniques implemented for the passivation of the gold contacts of the two PCB designs will be discussed. Finally, the electrochemical experiments for ORR, NRR and NO_3^- will be described, as well as some of the problems that were encountered during those experiments.

4.1. SEM characterization

The SEM images of a Pd_3Cu sample on pure ePTFE are shown in Figures 4.1 and 4.2.

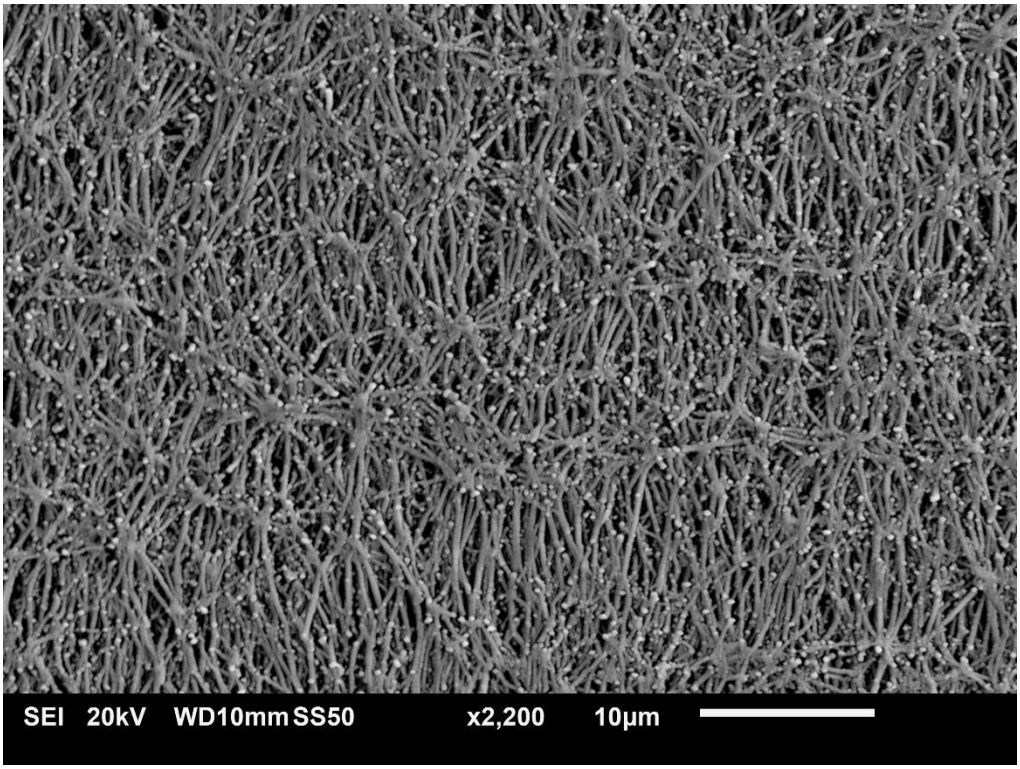

Figure 4.1. SEM image of a Pd_3Cu catalyst on pure ePTFE. The pores between the fibers of the pure ePTFE are not blocked by any metals that could attach over or around the fibers.

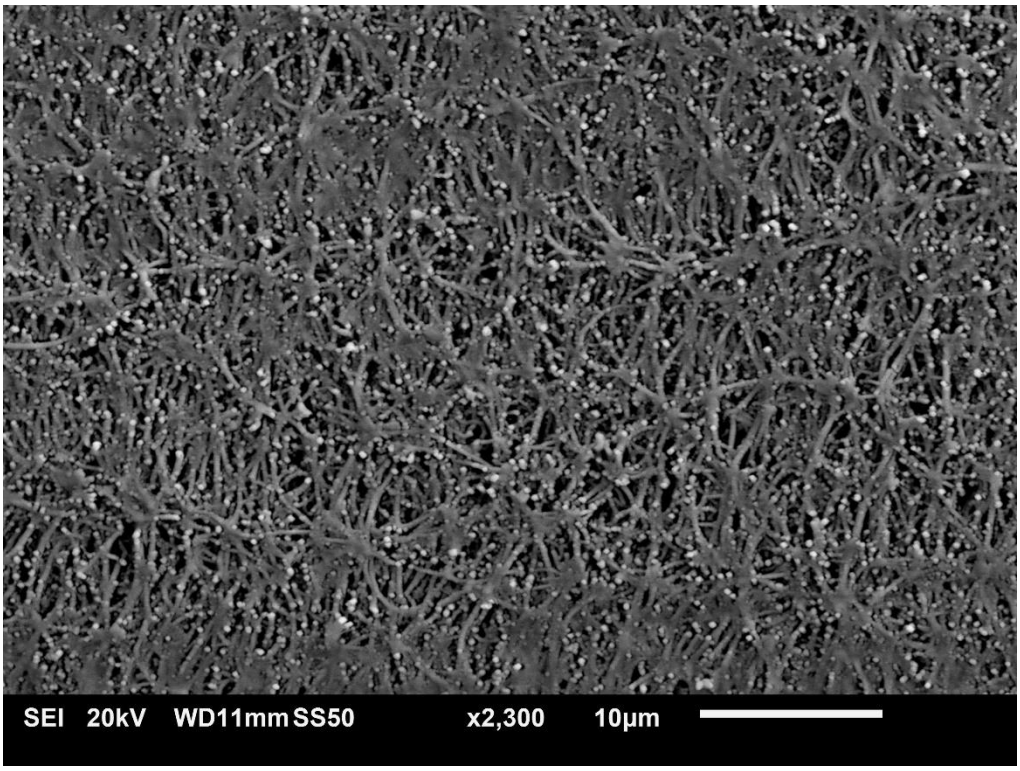

Figure 4.2. SEM image of a Pd_3Cu catalyst on pure ePTFE. Some of the pores around the fibers are covered by a metal layer of around 300 nm.

Figures 4.1 and 4.2 show the structure of the two different catalyst dots on the same Pd_3Cu sample on pure ePTFE. As shown in Figure 4.1, the pure ePTFE substrate has a fleece-like structure with small interconnected fibers. Between the fibers are the pores of the ePTFE that allow for gas to diffuse through them. In Figure 4.2 the same structure with the pure ePTFE fibers can be seen, but the pores between the fibers are now covered by the sputtered bimetallic catalysts. It appears that on top and around the fibers, small pockets of continuous layers of metal have formed. The images obtained from this sample can be compared to experimental results found in literature for a Pt sputtered coated Gortex membrane [50]. The Gortex membrane of the referenced study also has an ePTFE surface layer where the Pt catalyst is sputtered. Figures 4.3(a), (b) and (c) present the surface structure of the Gortex membrane sputtered with a Pt thickness of 50, 200 and 400 nm respectively.

(a) (b) (c)

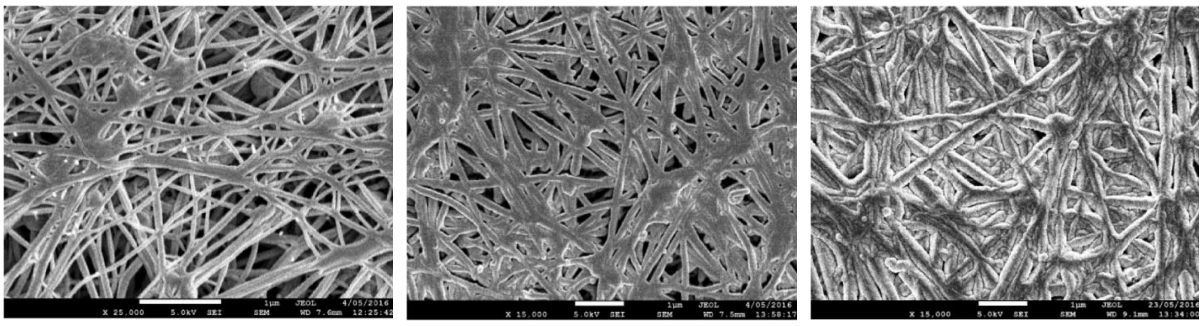

Figure 4.3. SEM images of the ePTFE surface of a Gortex membrane. Each sample has been sputtered with different thickness of Pt, (a) 50, (b) 200 and (c) 400 nm. Adapted from [50].

The SEM images of Figure 4.3 have many similarities to the images of Figures 4.1 and 4.2. Looking at Figure 4.1 and 4.3(a), they both depict a situation where only a very small amount of metal is present on the ePTFE surface. The fibers and the open pores between them are clearly visible and in Figure 4.3(a) some continuous layers can be detected. The ePTFE surface presented in Figure 4.3(b) is almost identical to the one in Figure 4.2, where a larger amount of sputtered metal leads to the creation of more continuous layers around the fibers. Still, there are enough open pores between the fibers for nitrogen to diffuse through it but the overall porosity of the ePTFE is not uniform over the surface of the sample. Finally, the SEM image of Figure 4.3(c) shows that the fibers of the ePTFE have thickened substantially compared to the previous cases. In certain areas the surface of the membrane looks completely covered by metal deposited around the fibers.

A SEM image of an AuCu sample created during this project is presented in Figure 4.4 to show the non-uniformity of the ePTFE surface coverage. Besides attaching around the fibers, the sputtered metal can also form a large continuous layer on top of the fibers, as is the case in this particular sample. Open pores can be detected scattered throughout the continuous metal layers and between the exposed fibers.

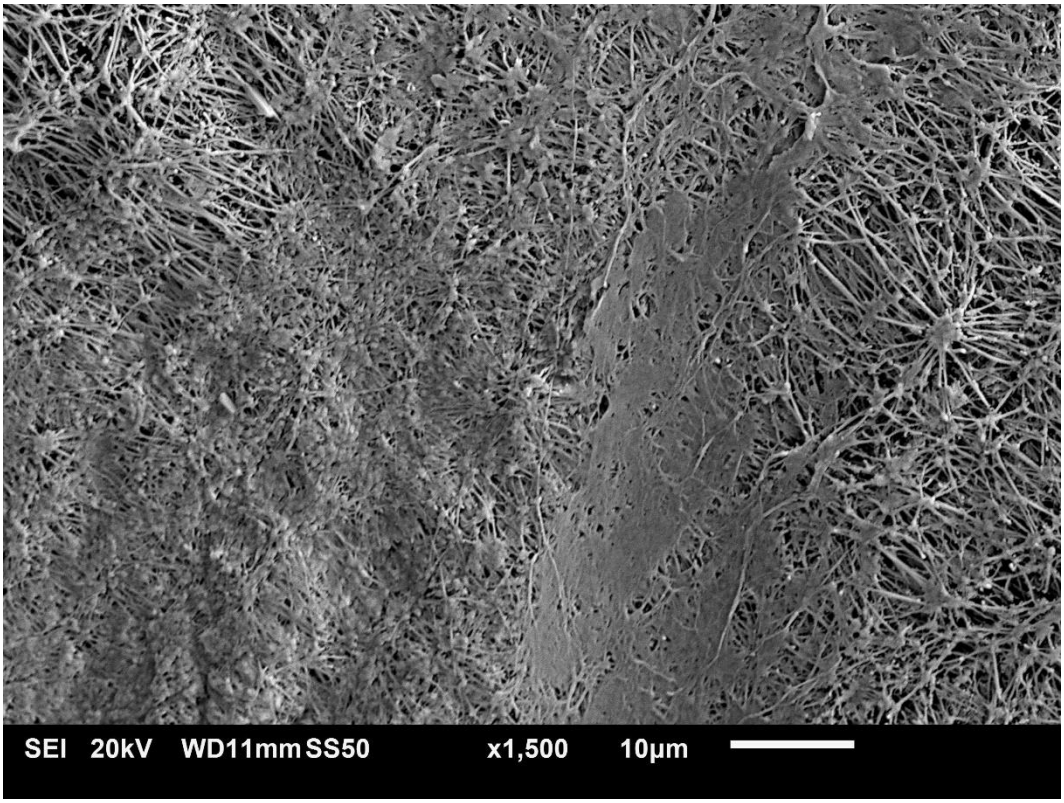

Figure 4.4. SEM image of an AuCu sample on backed ePTFE. It is clear that not every part of the surface is uniformly coated with a metal layer. On the far right of this image, the pores between the fibers are not open, while next to this area, a continuous layer of metal has formed over the fibers.

Based on the tooling data for the samples on Figures 4.1, 4.2 and 4.4 and the results from the composition calculator, the total thickness of the bimetallic thin film deposited on the ePTFE is 300 nm for all three of these catalyst dots. However, it is clear that the sputtered metal is not distributed evenly across the entire ePTFE surface and there are areas within each dot where the thickness of the sputtered thin film is higher. This non-uniformity of the sputtered metal can cause an inhomogeneous nitrogen supply, since some of the pores of the ePTFE could be blocked. Furthermore, the pure ePTFE material is difficult to handle and can easily bent. This can cause cracks on the surface of the ePTFE. Such a case is presented in Figure 4.5 and 4.6, where a zoomed-out SEM image of a PdCu sample is presented and then a zoomed-in image of one of the cracks.

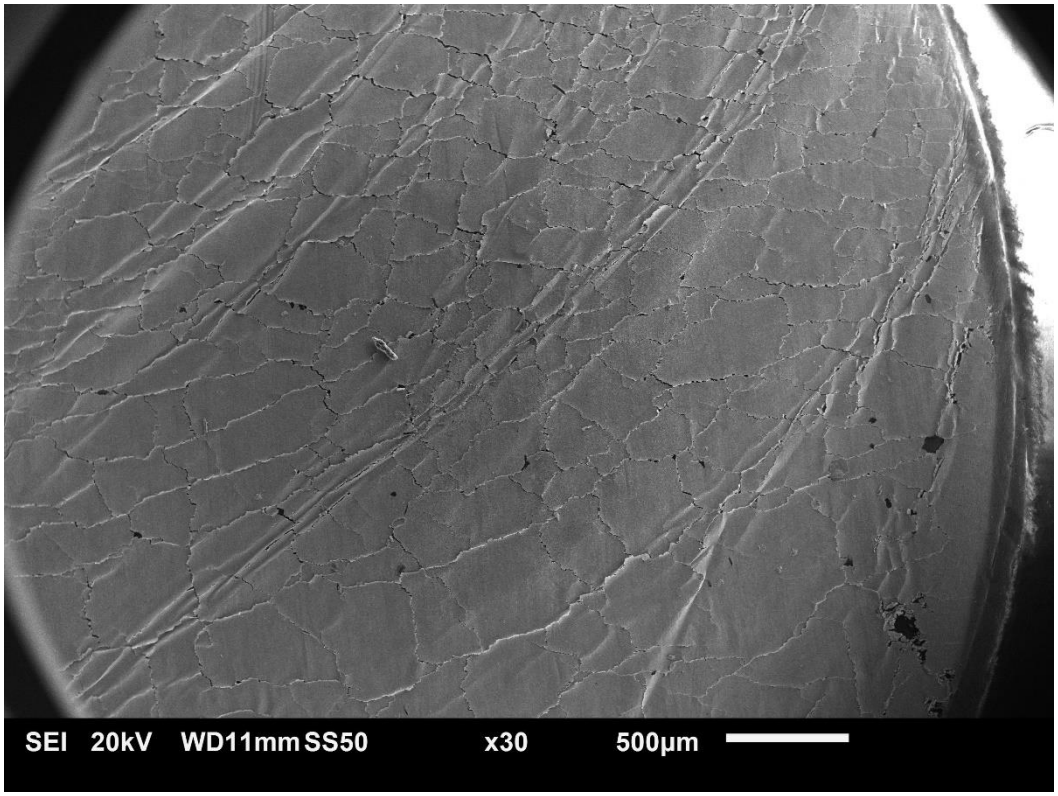

Figure 4.5. Fully zoomed out SEM image of a PdCu sample on pure ePTFE. Wrinkles and cracks on the deposited thin film can be identified throughout the entire surface of the sample.

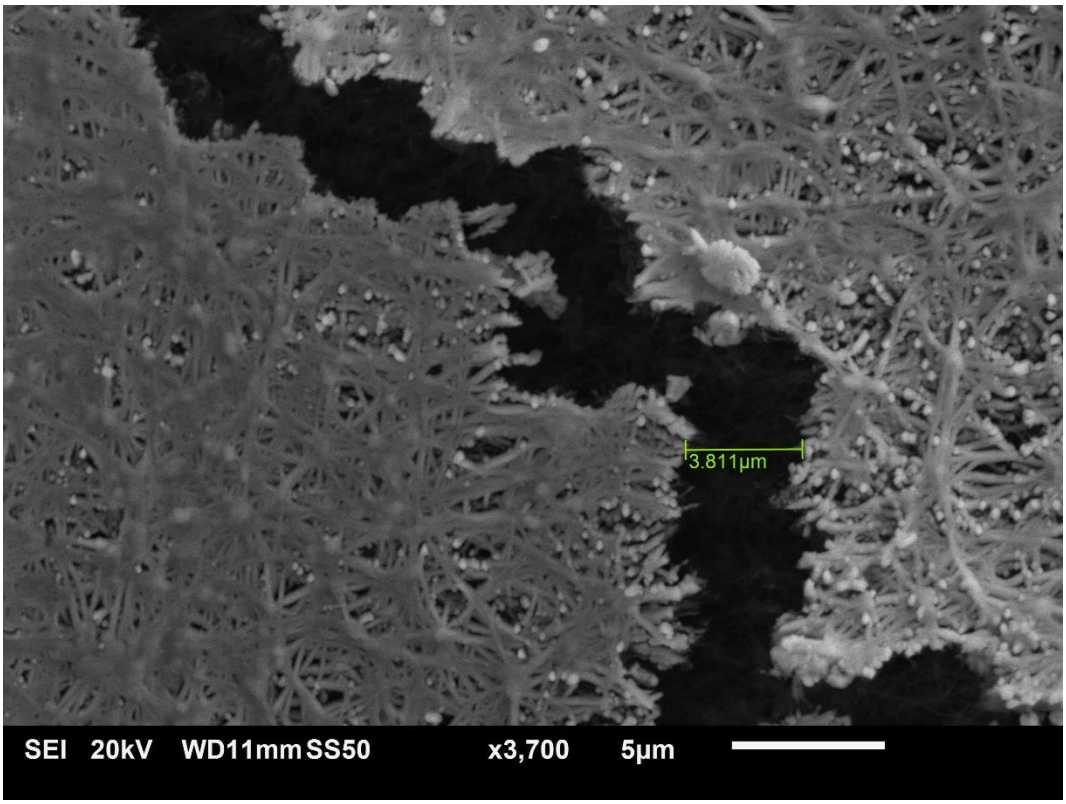

Figure 4.6. Zoomed in SEM image of a crack on the PdCu sample. The ePTFE fibers on the surface layer have been torn. Continuous layers are spotted on the ePTFE surface over the fibers.

When the pure ePTFE layer is bent, it causes the sputtered thin film catalyst dots on its surface to also bend. This causes the metal layers to crack and they force the fibers attached to them to fracture as well. Even though these cracks persisted for all samples, the ePTFE still maintained its hydrophobicity and no electrolyte leakage from the catholyte to the gas part was noticed during the experiments. However, these cracks could cause a problem with the electrical contact between the catalyst dots and the PCB, causing some areas of the catalyst surface to be electrically isolated.

4.2. EDS characterization

EDS was used to obtain the composition of every catalyst dot sputtered on an ePTFE sample. The composition values measured by EDS were compared with the predicted composition values from the composition calculator. For a sample where the targets are placed at a 180^{o} angle only 4 out of 16 catalyst dots have to be measured, since there are only 4 different compositions present on the sample. The EDS measurements for an AuAg alloy sputtered on pure ePTFE will be presented here. The Au and Ag targets are placed at an 180^{o} angle. Therefore, there will be four different compositions of the AuAg alloy present on the pure ePTFE sample. The predicted composition of the catalyst dots from the composition calculator and the measured composition by EDS are presented in Table 4.1:

Table 4.1. Measured composition by SEM and predicted composition by the composition calculator of an AuAg sample on pure ePTFE.

	Dot #	Au	Ag
Measured composition (SEM)	1	84.81	15.19
	2	70.31	29.69
	3	45.16	54.84
	4	27.62	72.38
Predicted composition (Composition calculator)	1	79.28	20.72
	2	59.71	40.29
	3	40.34	59.66
	4	21.18	78.82

It can be seen from Table 4.1 that there are differences between the measured and the predicted compositions of the catalyst dots. This can be attributed to the positioning of the sample on the sample holder. If the pure ePTFE sample is not placed at the center of the sample holder, then during the sputtering process a higher amount of one metal will be deposited on every catalyst dot. For the AuAg sample of Table 4.1, it is likely that the pure ePTFE sample was placed closer to the Au target, as the measured composition of Au is consistently higher than the predicted composition of Au. The measured and the predicted composition values can also be compared in Figure 4.7:

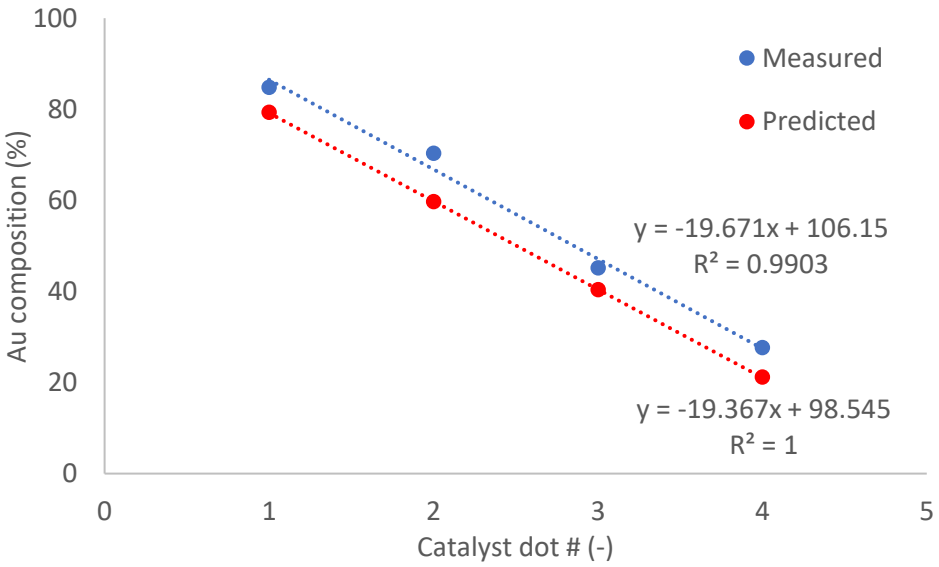

Figure 4.7. Measured and predicted composition of Au for four catalyst dots of a AuAg alloy on pure ePTFE. The equation of the trendlines and the R^2 values are also presented in the figure.

Even though the measured and predicted composition values of Au are different, the slope of the two trendlines is almost identical. The slope represents the thickness increase of Au per mm on the pure ePTFE sample, based on the calculations shown in Section 3.7. This indicates that the results of the composition calculator can be utilized to provide the maximum range of the compositions that can be achieved by magnetron sputtering.

4.3. XRD characterization

XRD was used to compare the crystal structure of catalysts deposited by sputtering, with the crystal structure formed by chemical synthesis methods described in literature. The XRD pattern of 16 catalyst dots on pure ePTFE can be recorded by programming a sequence to measure each dot in quick succession. The measured XRD pattern of a Pd_3Cu_1 dot on pure ePTFE is presented in Figure 4.8, while the XRD pattern of a Pd_3Cu_1 sample as reported in literature is presented in Figure 4.9:

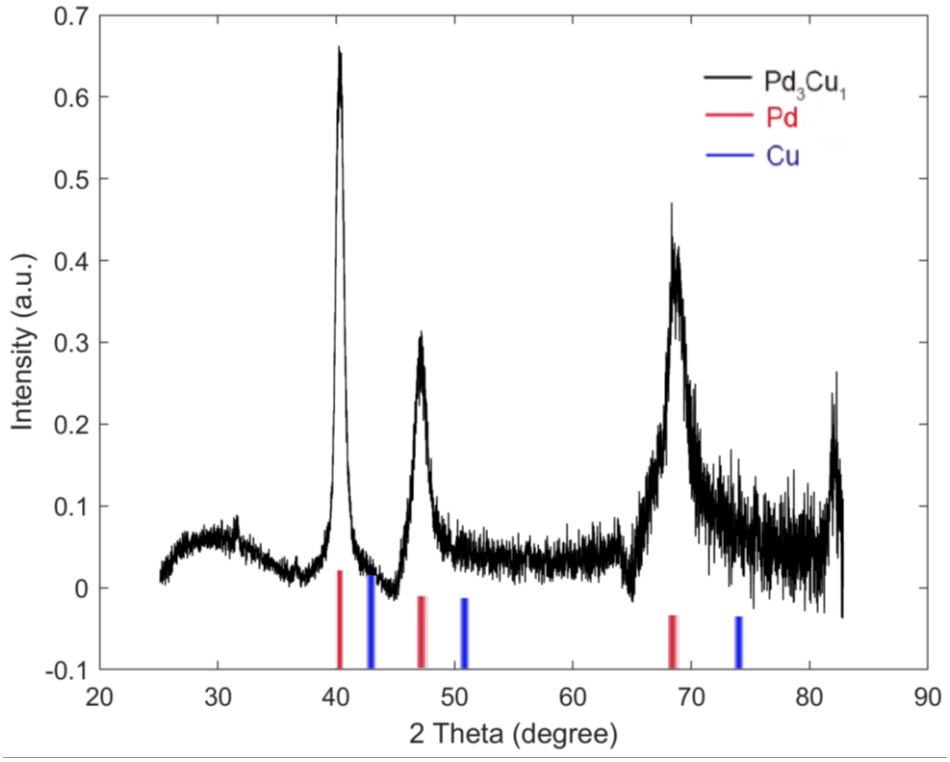

Figure 4.8. XRD pattern of a Pd_3Cu_1 sample on pure ePTFE. Four diffraction peaks can be identified at 40, 47, 69 and 82 degrees. The lines for the plain Pd and Cu are also shown.

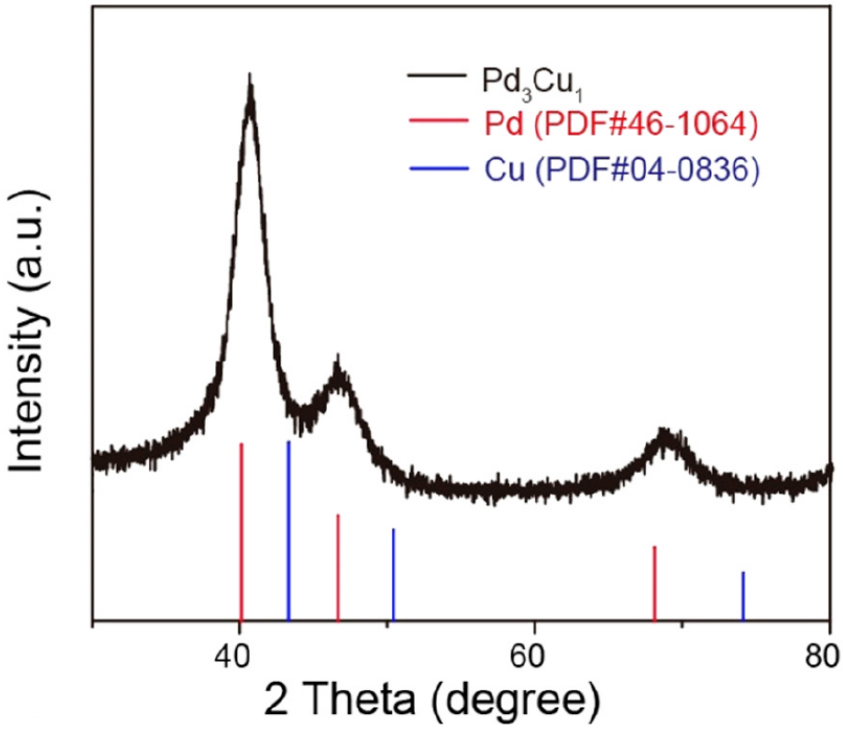

Figure 4.9. XRD pattern of a Pd_3Cu_1 sample reported in literature. Three diffraction peaks can be identified at 41, 47 and 69 degrees. The lines for the plain Pd and Cu are also shown. The diffraction peaks of the alloy are closer to the line of the pure Pd, which indicates the presence of a Pd-rich alloy. Adapted from [38].

In Figures 4.8 and 4.9 the XRD diffraction peaks can be identified at the same angles for both Pd_3Cu_1 samples. Slight deviations between the two samples can be attributed to inaccurate z-alignment of the XRD instrument. The only difference between the sample produced by magnetron sputtering and the one cited in literature is the intensity of the peaks. Such XRD patterns were obtained for all of the sputtered alloys and was compared with the literature data that was available. It was found that the XRD patterns for PdRu and AuCu exhibited the same diffraction peaks as the ones reported in literature for each alloy [39, 41]. These results show that the same crystal structure can be created through sputtering as with chemical synthesis methods for the catalysts cited in literature.

4.4. Anode and cathode of the potentiostat

After figuring out the cable color that corresponds to each electrode, it was important to check that the correct reactions were happening at the appropriate electrodes: oxidation at the anode (Ni wire) and reduction at the cathode (catalyst dots). To test this, a simple experiment was designed where two Ni wires were place inside a beaker filled with 0.1 M KOH electrolyte. The red and white cables are attached to one Ni wire, while the black cable is attached to the other. The reference electrode is also

placed in the beaker and connected to the green wire. When current is applied to this 3-electrode setup, oxidation will occur at one of the Ni wires and reduction on the other.

During water electrolysis, the moles of the produced hydrogen are double the number of moles of the produced oxygen. As a result, the reduction reaction can be identified by simply observing which Ni wire produces the most bubbles. Furthermore, when Ni is oxidized, some parts of its surface become slightly black or brown, which provides an additional way to confirm the results of this experiment. The sign of the applied current also affects which electrode is the cathode and which one is the anode.

Starting the experiment, 1 A current was applied to the Ni wires and the RE. During this test it was noticed that more bubbles were produced on the Ni wire attached to the black cable. Consequently, reduction occurred on that Ni wire, meaning that the black cable is the cathode for a positive current. For the -1 A experiment, more bubbles were produced on the Ni wire attached to the red and white cables. This was a clear indication that reduction occurred on that Ni wire, meaning that the red and white cables are the cathode for a negative current. The applied current for the experiments was -500 μA. Therefore, the configuration of the cables for the negative current was adopted.

4.5. Passivation of the PCB's electrical contacts

As mentioned in Section 3.1, the passivation of the gold contacts of the different PCB designs was of great importance. If the gold contacts are in contact with the electrolyte, then they will be taking part in the electrochemical reaction along with the catalyst dots, which might lead to false negative results or contamination issues. Therefore, a variety of techniques were tested to determine what was the most effective way of passivating the gold contacts.

The first option was coating the gold rings of the PCB with a thin non-conductive film of titanium dioxide TiO_2, which is known to be an electrically insulating material [51]. A PCB was coated with a thin uniform layer of TiO_2 (around 20 nm) using Atomic Layer Deposition (ALD), as shown in Figure 4.10(a). Another PCB was coated with a 500 nm layer of TiO_2 by magnetron sputtering, shown in Figure 4.10(b). EPTFE sputtering of a PCB was also tested, where an ePTFE layer of around 200 nm was deposited on the gold rings of the PCB, as shown in Figure 4.10(c).

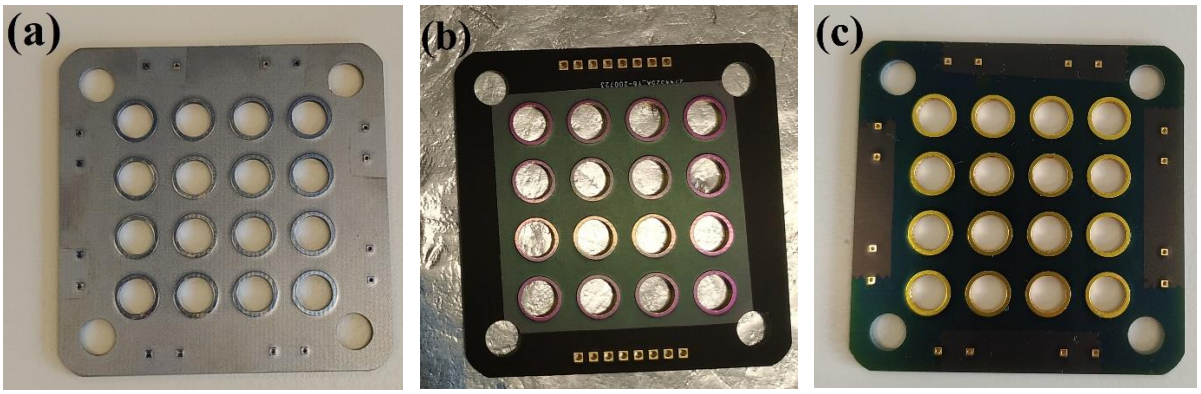

Figure 4.10. PCBs after attempting to passivate the gold rings through different techniques. (a) PCB coated with TiO_2 by ALD. (b) PCB coated with TiO_2 by magnetron sputtering. (c) PCB coated with ePTFE by magnetron sputtering.

In order to determine whether the passivation of the gold rings of the PCB was successful, a multimeter was used to contact two points of a single gold ring. The gold rings of all three of the PCBs in Figure 4.10 proved to be electrically conductive, suggesting that the deposited thin layers failed to passivate the gold rings. Next, techniques that would apply a thick conformal coating on the surface of the PCB were investigated. A PCB was coated with a thick layer (around 5 μM) of parylene, while another PCB was coated with a thick layer (several 100 μM) of silicon, using a RS modified silicon aerosol. However, these coatings could not be applied in a targeted area of the gold rings. As a result, the entire surface of the gold contacts was passivated, not only the surfaces that would be in contact with the electrolyte but also the surfaces that would be in contact the catalyst dots.

These unsuccessful attempts at passivating the gold contacts of the initial PCB design led to the new PCB design that was presented in Figure 3.11. In this design the gold contacts are smaller and they aren't in contact with the electrolyte, since the pure ePTFE that is pressed against the PCB from the gas side is hydrophobic and prevents the electrolyte from reaching the gold contacts. Due to uneven force distribution over the surface of the PCB, the dots close to the center of the PCB were not passivated. The stainless steel plate shown in Figure 3.14 provides a more equal force distribution over the surface of the PCB, facilitating a better contact between the PCB and the pure ePTFE for every dot. To prevent contamination issues and increase the stability of the PCB in the alkaline electrolyte, the back surface of the PCB was coated with the silicon aerosol.

The passivation of the gold contacts of the PCB was tested in the HTP cell design, which was assembled using a pure ePTFE piece without any catalysts sputtered on it. The electrochemical schedule that was applied to the passivation experiments involves applying -500 μA for 1 h. If the passivation of the gold contacts is successful and they are not in contact with the electrolyte, then the potentiostat will not be able to apply the specified current. Instead, a very small amount of current will be applied (around -1 to +2 μA) and the response of the potential will be recorded. An example of a passivation experiment where all 16 dots of the PCB are successfully passivated is presented in Figures 4.11 and 4.12:

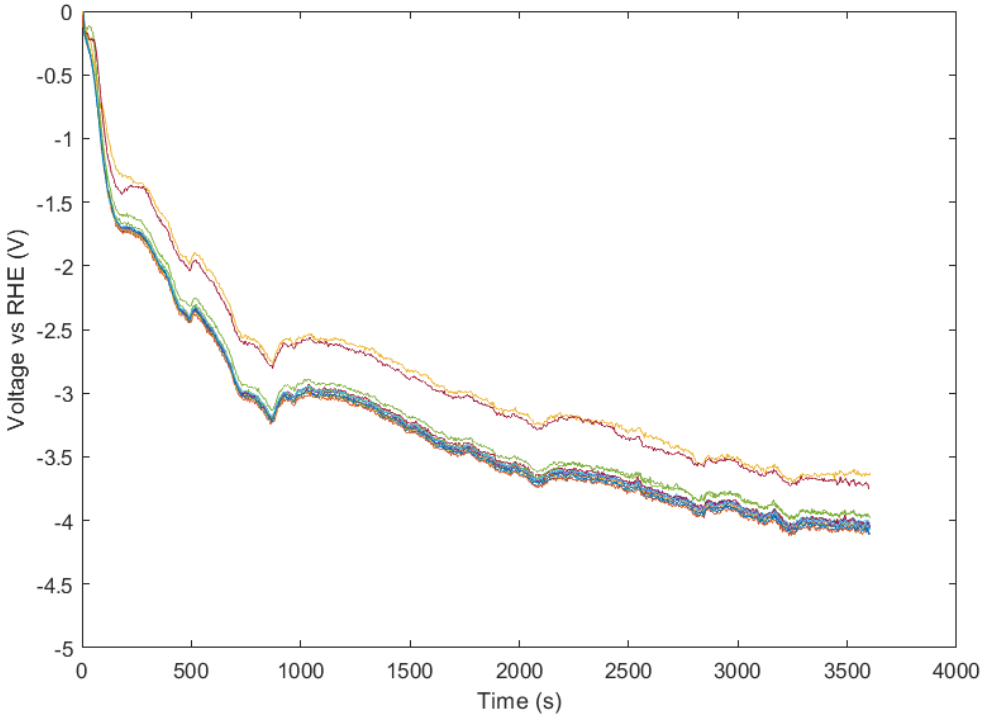

Figure 4.11. Response of the cell voltage for a PCB with passivated gold contacts over a 1 h period. All 16 gold contacts of the PCB are passivated.

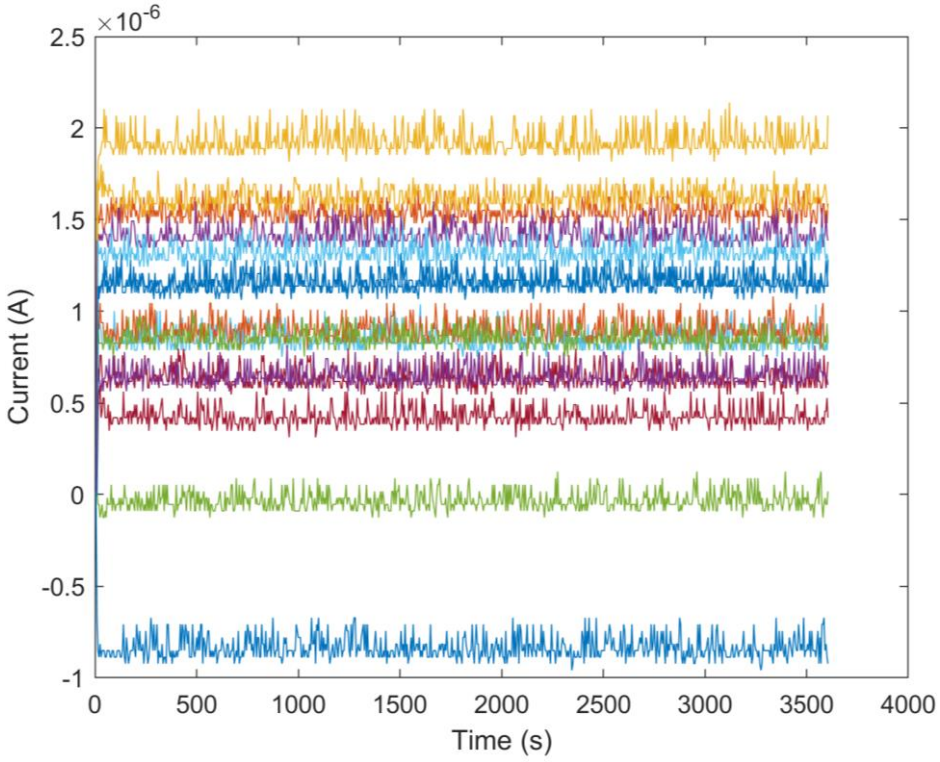

Figure 4.12. Applied current for a PCB where all 16 gold contacts are passivated over a 1 h period. The applied current ranges from -1 to +2 μA, even though the set value on the potentiostat for the current is -500 μA. This is an indication that the gold contacts of the PCB are passivated.

In Figure 4.11 the voltage is reported as 'Voltage vs RHE', because the reference electrode that is used in the HTP cell is a reversible hydrogen electrode. Every voltage value that is reported in this work from this point onwards is the voltage vs RHE. The voltage of the passivated cell has a value around -0.1 V at the start of the experiment and it gradually decreases to around -4 V over a 1 h period. This can be attributed to an increase in ionic resistance of the electrolyte or to bubbles that form inside the cell on the surface of the WE and CE. In figure 4.12 it can be seen that the applied current by the potentiostat for every channel has a value between -1 and +2 μA. However, the set value specified during the preparation of the electrochemical schedule is -500 μA, which the potentiostat is not able to apply. The gold contacts of the PCB are not in contact with the electrolyte but are only in contact with the ePTFE, which is a non-conductive material. As a result, a high voltage value is recorded for a small amount of applied current due to the high resistance of the pure ePTFE. These plots indicate that the gold contacts of the PCB are passivated and won't take part in the electrochemical reactions when a pure ePTFE sample with catalyst dots is tested.

4.6. HTP cell validation

4.6.1. NH_3 background

The NH_3 background concentration that was present in the cell parts, the ultrapure water and the electrolyte was quantified by NMR spectroscopy. If any NH_3 is left in these parts after an electrochemical experiment, it can provide false positives with regards to the catalytic activity of the samples that will be tested in future experiments. The cleaning processes of the cell and the NMR tubes that were described in sections 3.2 and 3.5 respectively aim to prevent this. Table 4.2 shows the NH_3 concentration before and after the cleaning processes were applied to the cell parts and the NMR tubes.

Table 4.2. NH_3 concentration in different chemicals and components of the HTP cell configuration, quantified by NMR spectroscopy.

	NH_3 before cleaning step (μM)	**NH_3 after cleaning step (μM)**
Ultrapure H_2O	0	3.78
0.1 M KOH	5.19	7.85
Cell	36.91	7.91

The cell measurement is conducted by filling the catholyte compartment of the HTP cell with 0.1 M KOH electrolyte, waiting for 1 h and then taking a liquid sample of the electrolyte from the catholyte compartment. A pure ePTFE without sputtered catalysts is used in the HTP cell. It is evident that the cleaning protocol implemented for the cell parts helped to reduce the NH_3 that was present in the cell.

However, the concentration of NH_3 in the ultrapure water and the 0.1 M KOH appears to increase after the cleaning step. This is caused by contamination of the glassware or the chemicals used during the NH_3 detection process. Overall, the concentration of NH_3 that could contaminate future experiments is 11.7 µM (cell + ultrapure H_2O).

This measured value for the NH_3 background corresponds to 0.12 ppm of NH_3. This value is lower than the 17.9 ppm, which is the expected value of NH_3 produced by an active catalyst (see Section 3.5). These results show that the cell is NH_3-free after every screening experiment and emphasize the importance of following the cleaning protocols to prevent false positives during the screening of bimetallic catalysts.

4.6.2. NH_3 crossover

The purpose of the NH_3 crossover experiment is to determine the amount of NH_3 that can diffuse from the catholyte to the anolyte compartment through the Zirfon membrane. The HTP cell is assembled and the catholyte and anolyte compartments are filled with ultrapure water. Next, a few drops of ammonium chloride solution (NH_4Cl) are added into the catholyte compartment and the HTP cell is sealed for 1 h. Liquid samples from the electrolyte are taken from both compartments at t=0 and t=1 h to measure the concentration of NH_3. The results are presented in Figure 4.13.

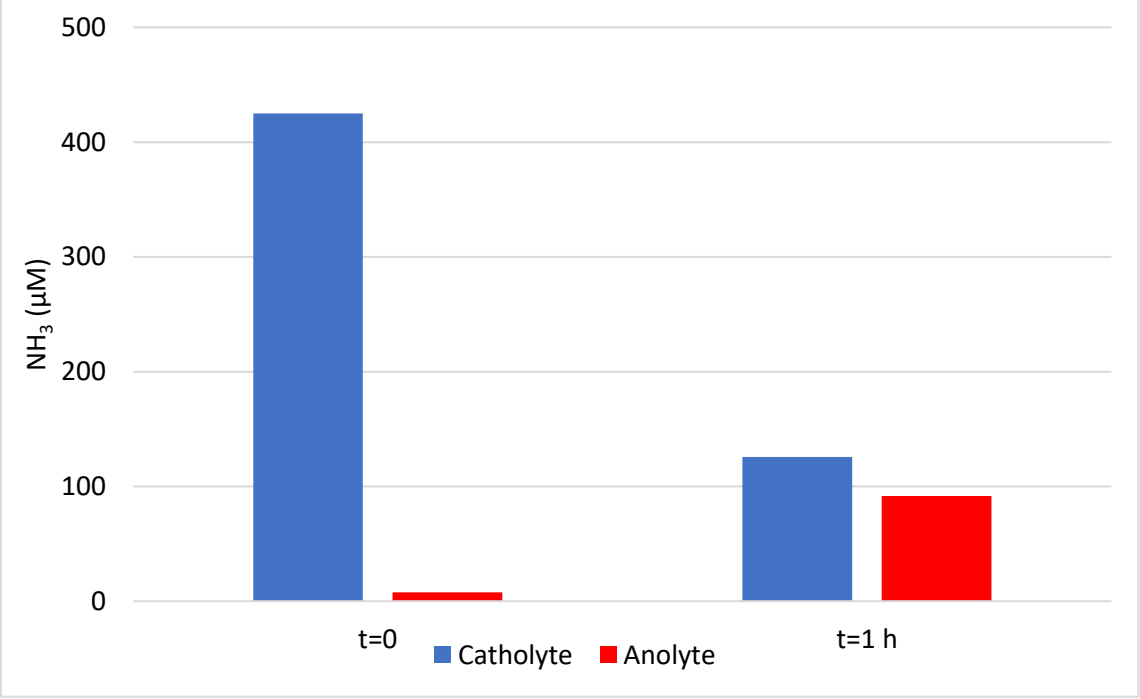

Figure 4.13. NH_3 concentration of the catholyte and anolyte compartments at the start of the experiment (t=0) and after 1 hour (t=1 h) inside the HTP cell with no current being applied.

The concentration of NH_3 in the catholyte compartment at the start of the experiment is 425 μM, while in the anolyte compartment it is 8 μM. After 1 h inside the HTP cell, it is clear that some NH_3 has diffused through the Zirfon membrane into the anolyte compartment. The final concentration is 126 μM of NH_3 in the catholyte compartment and 92 μM in the anolyte compartment. These values combined are much lower than the 433 μM of NH_3 present in the HTP cell at the start of the experiment. This could be caused by the loss of catholyte volume due to leakage or absorption of ammonia in the cell components. However, it is still clear that NH_3 can diffuse through the Zirfon membrane. For quantitative measurements, liquid samples should be taken from both compartments during the screening of the catalysts, as the NH_3 concentration of a single compartment might not provide sufficient information about the catalytic activity of a bimetallic catalyst. It is also noteworthy that the Zirfon membrane that was used in this study might not be ideal for the separation of NH_3, because after 1 h the concentration has almost equilibrated. More selective membranes have to be found, which is beyond the scope of this work

4.6.3. NH_3 loss

The NH_3 loss experiment was conducted for two reasons. First, to determine whether any NH_3 that is produced in the HTP cell does not absorb in the cell components. Second, to show that NH_3 does not oxidize after it crosses from the catholyte over to the anolyte compartment. The catholyte and anolyte compartments of the HTP cell are filled with ultrapure water. Then, an NH_3 solution with identical concentration is added into both compartments. Two distinct experiments are conducted, where no current is applied to the cell for the first experiment and a current of -500 μA is applied for the second experiment. The duration of each experiment is 1 h, with liquid samples taken from both the catholyte and the anolyte compartments of the cell at the beginning (t=0) and at the end of the experiment (t=1 h). The results of the experiments with no applied current and -500 μA current are presented in Figures 4.14 and 4.15 respectively:

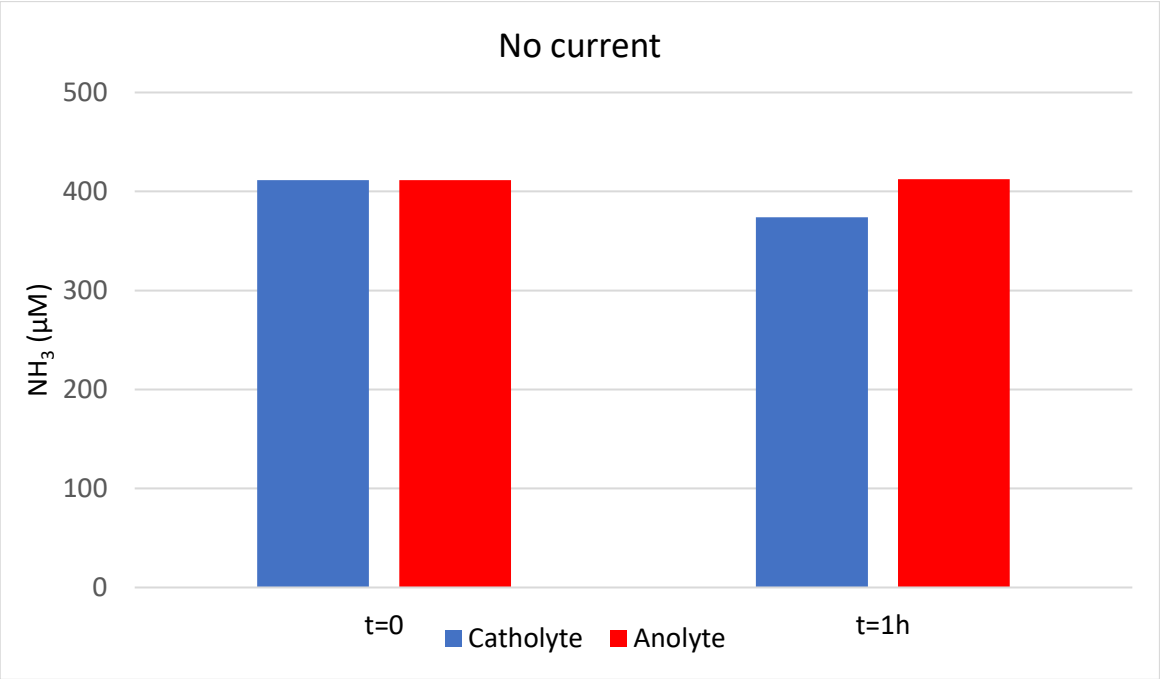

Figure 4.14. NH_3 concentration of the catholyte and anolyte compartments at the start of the experiment (t=0) and after 1 hour (t=1 h) inside the HTP cell with no current being applied.

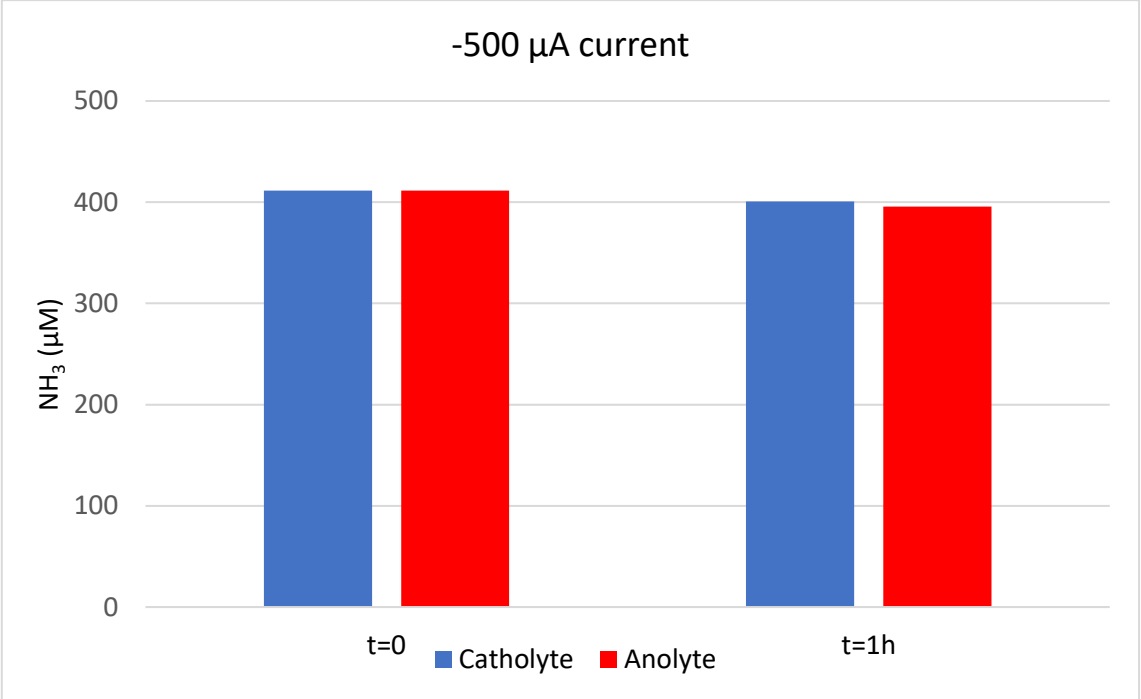

Figure 4.15. NH_3 concentration of the catholyte and anolyte compartments at the start of the experiment (t=0) and after 1 hour (t=1 h) inside the HTP cell with a -500 µA current being applied.

In both experiments, the initial concentration of NH_3 in the catholyte and anolyte compartments is 411 µM. In the experiment where no current is applied, the final concentration in the catholyte compartment is 374 µM, while in the anolyte it is 412 µM. This shows that the NH_3 cannot escape from

the cell through the connectors or the gas parts and no ammonia is absorbed. The lower amount of NH_3 in the catholyte compartment could be caused due to errors during the NMR measurements, something that is further emphasized by the results of the -500 μA experiment.

In the case where a current of -500 μA is applied to each dot of the cell, the final concentration of NH_3 is 401 μM in the catholyte compartment and 396 μM in the anolyte. If NH_3 was getting oxidized to NO_3^-, based on Faraday's law shown in Eq. (3.1), we would expect 230 μM of NH_3 from the anolyte compartment to be consumed during this experiment. However, the measured decrease of NH_3 in the anolyte is only 15 μM. This indicates that NH_3 isn't being oxidized significantly in the anolyte and the small decrease in concentration can most likely be attributed to measurement error. If any NH_3 was consumed due to electrochemical reactions, we would have expected a much larger decrease in its concentration, especially in the anolyte compartment.

4.6.4. ORR experiments

The first experiments that were conducted for the electrochemical validation of the HTP cell were oxygen reduction reaction (ORR) experiments. The HTP cell was not connected to the N_2 supply but instead the gas part connectors were unplugged and exposed to atmospheric air. As a result, ORR would occur on the catalyst surface. In this validation experiment, a pure ePTFE substrate was used with only 8 out of 16 AuRu dots sputtered on its surface. Consequently, only 8 gold contacts of the PCB were in contact with AuRu dots, while the other 8 were in contact only with ePTFE. Additionally, the gold contacts of the PCB are not passivated because the old PCB design shown in Figure 3.3 is used. This means that the gold contacts will be in contact with the electrolyte and conduct current on the dots that don't have a catalyst sputtered on them. This cell configuration, PCB and pure ePTFE with 8 out of 16 dots was only used in the experiment discussed in this section, every other experiment followed the HTP cell design presented in Figure 3.14.

The duration of the experiment is 1 h with a current of -500 μA applied to all 16 dots of the PCB. During the first 30 min of the experiment, the most dominant reaction taking place in the catholyte compartment is oxygen reduction. After 30 minutes, the nitrogen supply is connected to the HTP cell and switched on at a flowrate of 1.2 mL/min. From this point until the end of the experiment the dominant reaction in the catholyte is hydrogen evolution. The response of the potential is presented in Figure 4.16:

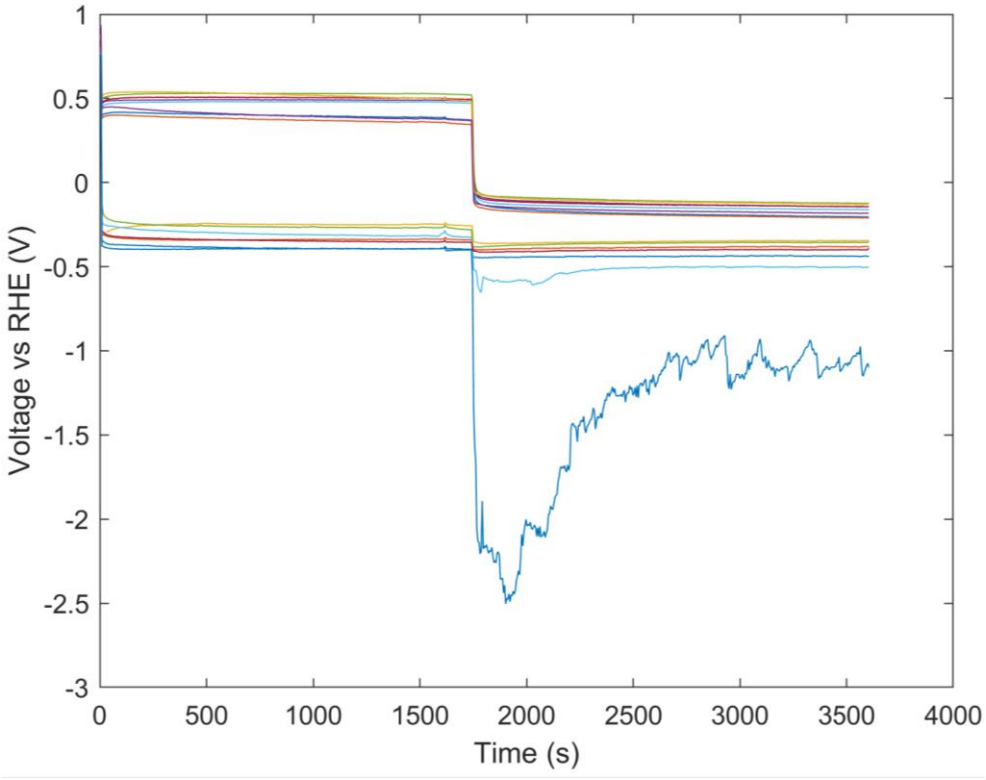

Figure 4.16. Voltage of all 16 dots of the HTP cell over a 1 h time period. The nitrogen supply is connected at around 1750 s and a sharp decrease in the cell voltage can be noticed at that moment.

Initially, the first 30 min of Figure 4.16 will be examined. Two distinct sets of voltage ranges can be detected, one ranging from 0.4 to 0.5 V and another from -0.3 to -0.4 V. The former corresponds to the 8 AuRu dots sputtered on the pure ePTFE sample, while the latter corresponds to the 8 dots that are only in contact with ePTFE. This is identified based on the type of reaction occurring on each set of dots. On pure ePTFE, HER will occur, as it is a reaction that occurs at lower potential compared to ORR, which occurs at the AuRu dots. The current that was applied to each dot of the PCB remained constant throughout the 1 h duration of the experiment at -500 μA. Furthermore, the voltage values being between -0.3 and -0.4 V suggests that the gold rings of the PCB are taking part in the electrochemical reaction.

The nitrogen is connected to the cell 30 min after the start of the experiment. The voltage of the AuRu dots drops quickly between -0.1 to -0.2 V, while the voltage of the dots in contact with ePTFE decreases between -0.4 to -0.5 V. Overall, the voltage of every AuRu dot has decreased by 0.6 V, going from a positive to a negative potential. This indicates that the dominant reaction in the catholyte compartment is no longer the oxygen reduction, but the hydrogen evolution. For the 8 dots that are only in contact with ePTFE the voltage decrease is much lower, only 0.1 V for each dot, which means that HER continues for these dots. The only exception is the dot for which the potential drops to -2.5 V and after fluctuating, reaches -1.1 V. The behavior that this dot experiences could be due to mechanical instabilities inside the cell. The pure ePTFE might not be contacting the PCB correctly, which could

also lead to bubbles accumulating on that dot. The bubbles would cause a higher resistance and a higher overpotential for that dot, which could explain the much lower voltage value compared to the other dots.

4.6.5. Experiments for different electrolyte concentrations

These experiments were conducted to show the effect of different electrolyte concentrations on the operating voltage of the catalyst dots. In these experiments, the nitrogen supply is connected to the HTP cell from the beginning of the experiment. The reaction that dominates on most of the catalyst dots is HER and not NRR, due to reasons discussed in Section 2.1. Two experiments are presented here, one with a 0.1 M KOH electrolyte and one with a 1 M KOH electrolyte. The pure ePTFE has 16 PdRu catalyst dots sputtered on its surface. The current applied to each catalyst dot is -500 μA for 1 h and the response of the voltage is presented in Figures 4.17 and 4.18 for the 0.1 M and the 1 M KOH respectively.

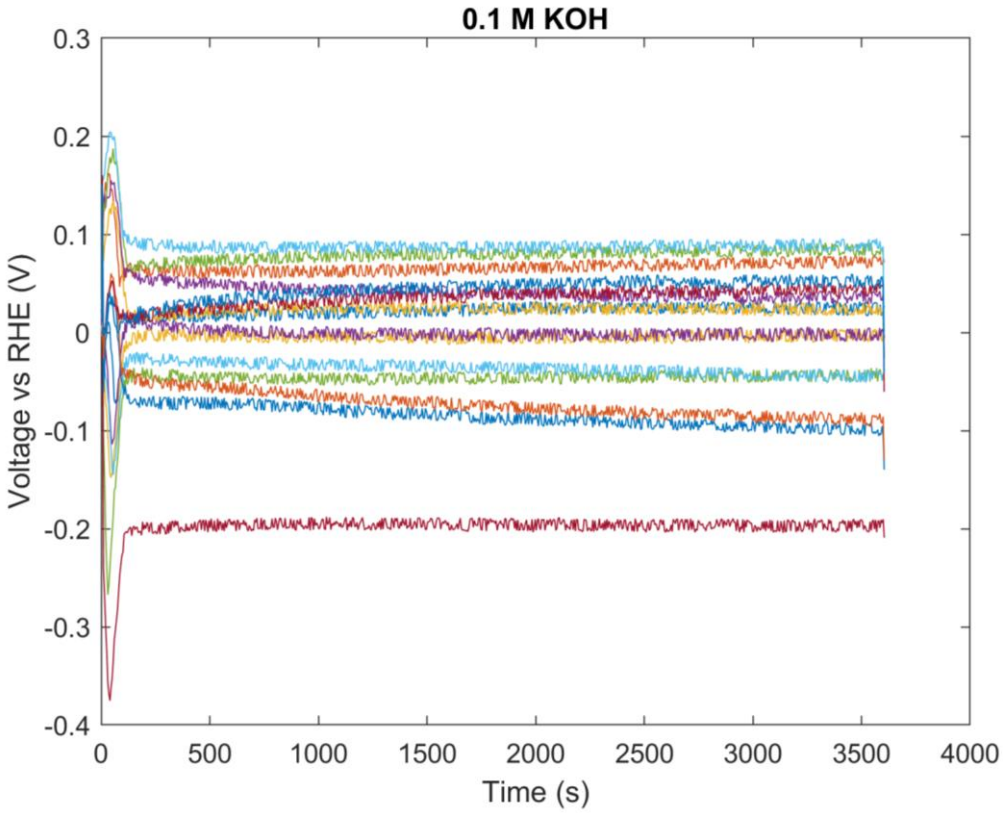

Figure 4.17. Chronopotentiometry of 16 PdRu catalyst dots on pure ePTFE at -500 μA over a 1 h time period. The concentration of the KOH electrolyte is 0.1 M.

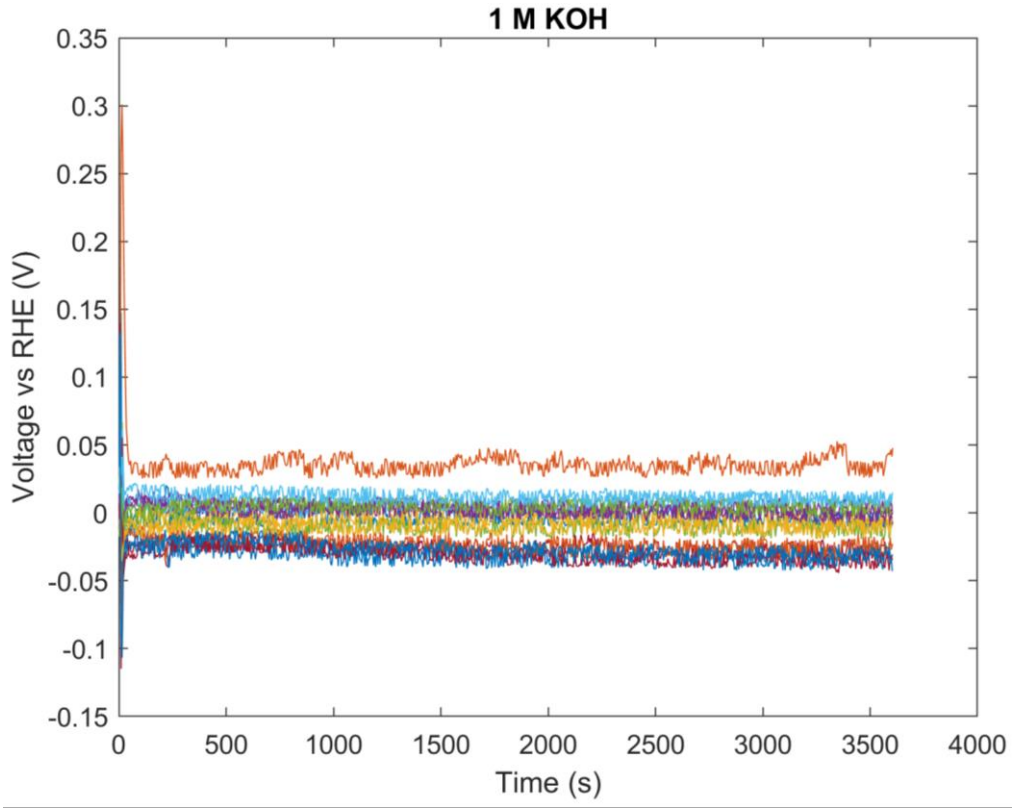

Figure 4.18. Chronopotentiometry of 16 PdRu catalyst dots on pure ePTFE at -500 µA over a 1 h time period. The concentration of the KOH electrolyte is 1 M. The range of voltage values is smaller for an electrolyte of higher concentration, due to its increased ionic conductivity.

The voltage values presented in both figures fluctuate for the first 100 s of the experiment. Then, the voltage of each dot stabilizes at a value that remains constant until the end of the experiments, only experiencing minor fluctuations. For the 0.1 M KOH experiment, the voltage of all catalyst dots ranges between -0.1 and 0.1 V, with one value at -0.2 V. However, in the 1 M KOH experiment, a much narrower spread of the voltage values can be seen, with the values being between -0.04 and 0.04 V. This can be attributed to the higher ionic conductivity of the 1 M KOH electrolyte, since the ions encounter lower resistance when moving inside the electrolyte. Overall, the 0.1 M KOH experiment shows the typical voltage values and the behavior of the voltage over time curve that can be expected during NRR experiments with the sputtered catalysts.

4.6.6. NO_3^- reduction experiments

This experiment was conducted to determine whether NH_3 that was produced in the cell could be detected by the GC. The HTP cell was assembled with a Cu catalyst on all 16 dots of the pure ePTFE substrate. The inlet of both gas parts of the HTP cell were connected to the nitrogen supply and the outlet of the gas part on the catalyst side in Figure 3.14 was connected to the GC. Next, the catholyte and

anolyte compartments were filled with 1 M KOH electrolyte that also contains 100 mM NO_3^- (nitrate). NO_3^- can be reduced to NH_3, producing a larger amount of NH_3 compared to what can be achieved through NRR for the same catalyst. A PARSTAT 4000A potentiostat with one channel was used for this experiment. Three different current values, -0.12, -10 and -50 mA, were applied to one Cu catalyst dot and the response of the voltage was recorded. The current and voltage values over the duration of the experiment are presented in Figures 4.19 and 4.20 respectively.

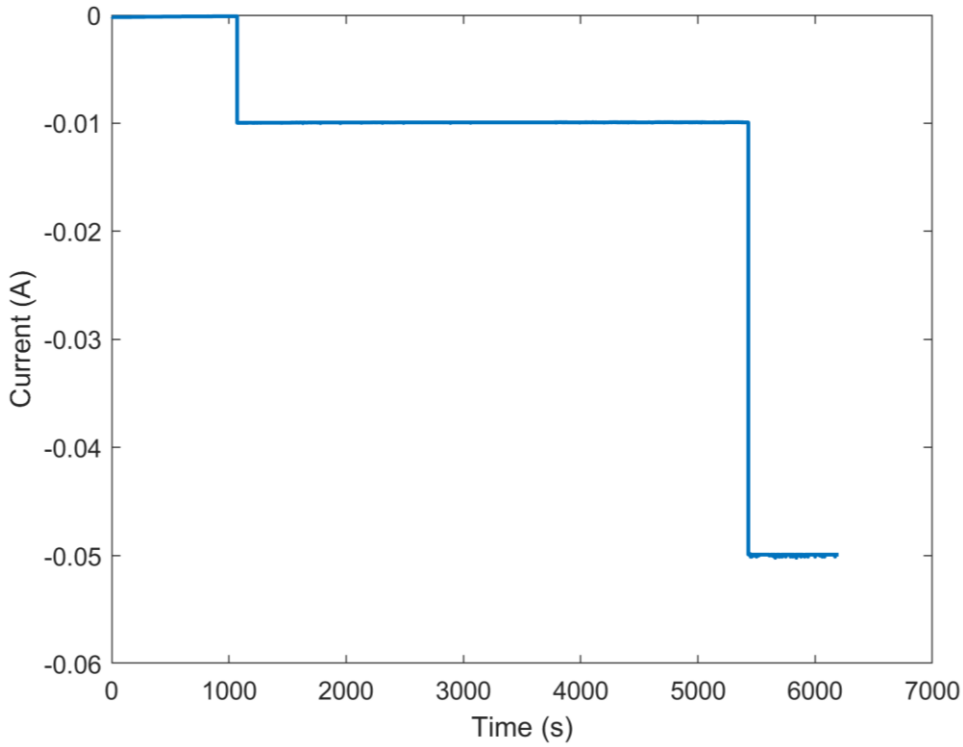

Figure 4.19. Current over time applied to one Cu catalyst dot of the HTP cell. Three different current values are applied to the catalyst dot: -0.12 mA from the start of the experiment to 1070 s, -10 mA between 1070 and 5430 s and -50 mA from 5430 s until the end of the experiment.

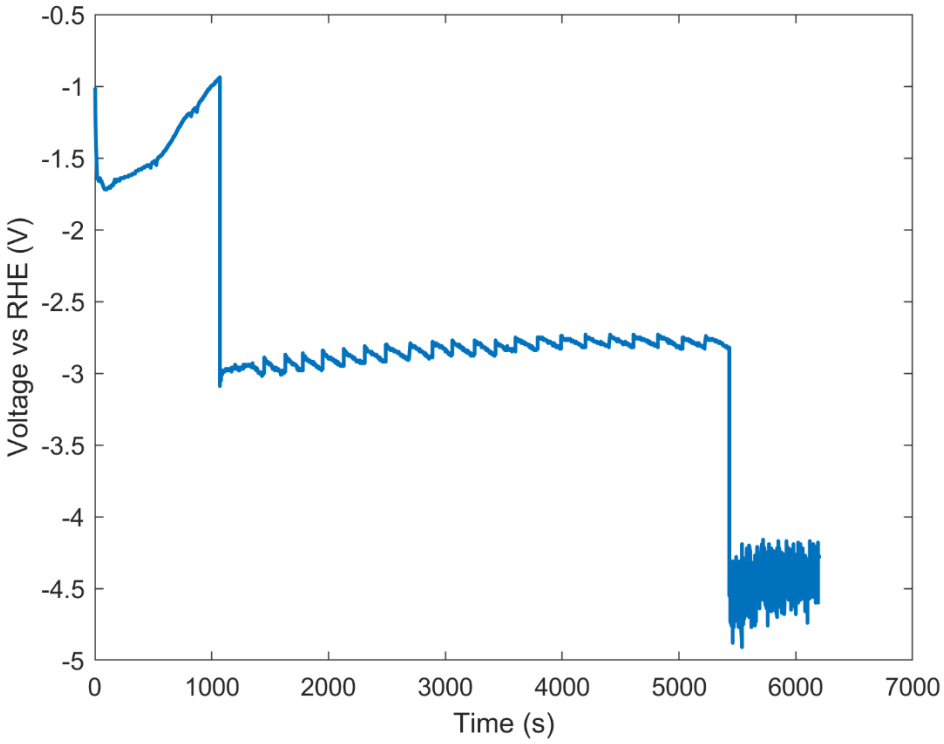

Figure 4.20. Voltage over time for one Cu catalyst dot of the HTP cell. The peaks encountered between 1070 and 5430 s indicate that bubbles are accumulating on the electrodes. After 5430 s, leakage occurred in the cell, since the higher current led to a larger number of bubbles forming in the cell.

The current applied to the Cu dot was stable and didn't experience any fluctuations throughout the experiment. The voltage peaks encountered between 1070 and 5430 s in Figure 4.20 can be explained by the formation of bubbles on the surfaces of the electrodes. This causes a higher overpotential, which in turn causes a lower voltage, until the bubble detaches from the surface of the electrode. Then, the voltage momentarily increases before starting to decrease again. From 5430 s until the end of the experiment, the applied current of -50 mA proved too high, as the produced bubbles resulted to an electrolyte leakage in the cell, causing the voltage to behave unpredictably.

During this experiment, the amount of produced NH_3 in the gas phase was measured with GC, while liquid samples were taken from the catholyte compartment to measure the NH_3 in the electrolyte by NMR spectroscopy. First, the detection of NH_3 in the gas phase will be discussed. The flowrate of the nitrogen supply was set to 10 mL/min, but only 1 mL/min reached the inlet of the GC. This indicates that there was gas leakage in the connectors of the gas parts or at the connectors of the water trap and the GC. Every 6 min the gas product was injected into the GC to measure the concentration of NH_3, with the results presented in Figure 4.21.

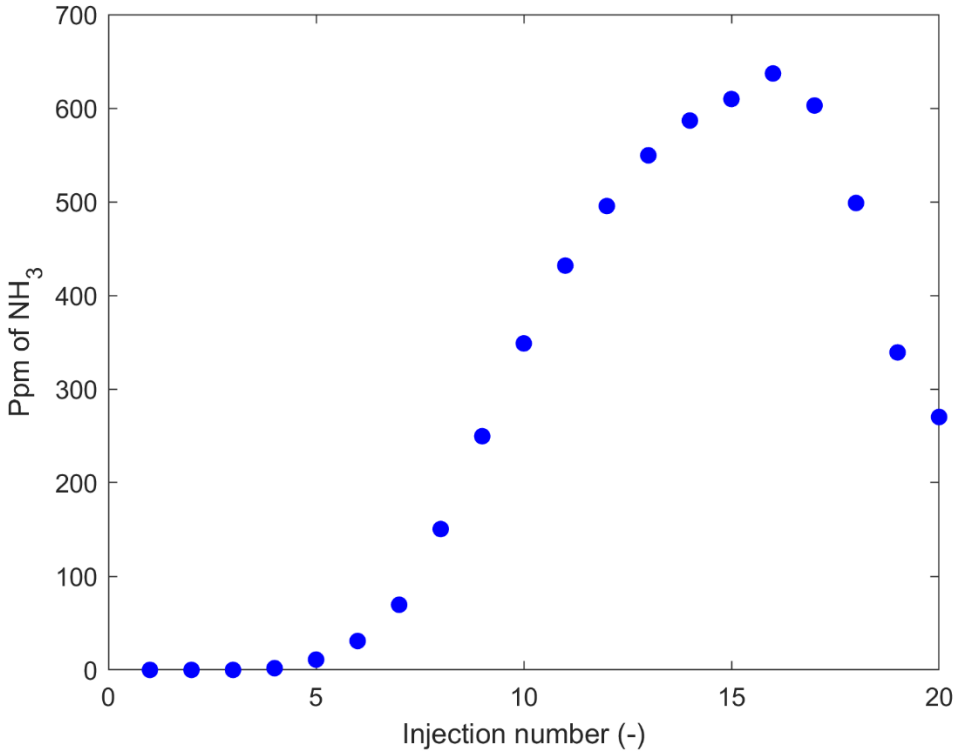

Figure 4.21. Ppm of the produced NH_3 in the gas phase. The current applied to the cell for the first 3 injections is -0.12 mA, from injection 4 to injection 16 it is -10 mA and for the last 4 injections it is -50 mA.

Looking at Figure 4.21 it is clear that, no NH_3 was detected for the first 3 injections since the applied current was only -0.12 mA. Based on Faraday's law, the expected amount of produced NH_3 was 0.23 ppm. However, from injection 4 until injection 16, the applied current was increased to -10 mA, which caused an exponential increase in the amount of produced NH_3 between injections 4 and 12. The produced NH_3 can either diffuse back into the gas part and escape towards the GC or it can be diluted inside the electrolyte. One hypothesis for the cause of the exponential increase is that as the solubility limit of the electrolyte is reached, any NH_3 that should have been diluted in the electrolyte, is instead forced back into the gas part. Between injections 13 and 16 the concentration increase becomes linear, suggesting that the gas and liquid phase might be in equilibrium during those injections, until it peaks at 637 ppm. At this point, the current is increased to -50 mA. The production of NH_3 decreases sharply until the end of the experiment, which suggests that no NH_3 is produced anymore. The stop of NH3 production might be caused by a loss of stability of the catalyst.

Next, the FE of each injection is calculated based on Eq. (3.3)-(3.5) and presented in Figure 4.22:

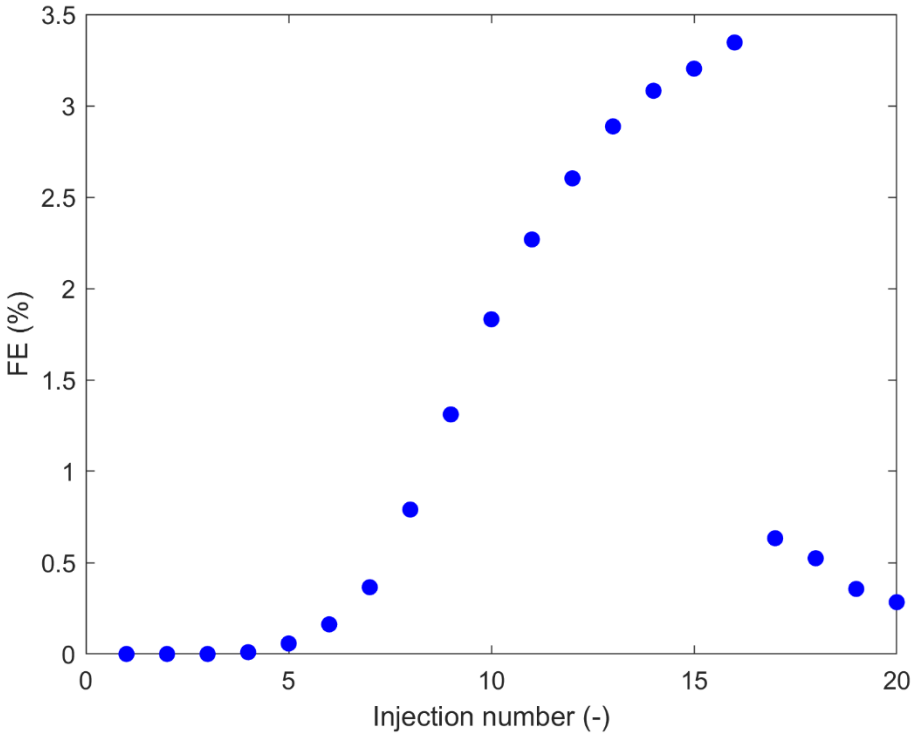

Figure 4.22. Faradaic efficiency of the ammonia detected in the gas phase for each injection. The current applied to the Cu dot for the first 3 injections is -0.12 mA, from injection 4 to injection 16 it is -10 mA and for the last 4 injections it is -50 mA.

The FE presented in Figure 4.22 has a similar pattern to the produced ppm of NH_3, shown in Figure 4.21. This was expected, as the only variable that changes between injections in Eq. (3.5) to (3.5) is the applied current. This results to the very low FE reported for the last 4 injections, where the cell became unstable due to the -50 mA of applied current. These FE values for NH_3 in the gas phase will be later compared to FE of the NH_3 produced in the liquid phase.

The concentration of NH_3 in the liquid is measured by taking samples of the electrolyte than can then be analyzed by NMR spectroscopy. In total 4 liquid samples are taken, which occur approximately at the same time as injections 11, 13, 14 and 15. If the measurement for the first injection is considered to be taken at t_1=0, then the measurements for injections 13, 14 and 15 occur for t_2=716 s, t_3=1292 s and t_3=1562 s. The applied current during those injections is -10 mA. The measured NH_3 concentration in μM is presented in Table 4.3. This value represents the accumulated NH_3 in the electrolyte. The NH_3 produced between each injection is the difference of two consecutive measurements. The electrolyte volume is 10 mL. Furthermore, the maximum NH_3 that can be produced is given by Faraday's law, as shown in Eq. (3.1). Finally, the FE of NH_3 in the liquid phase for injections 13, 14 and 15 can be calculated based on Eq. (3.5) and the results are compared with the FE of NH_3 in the gas phase in Figure 4.23.

Table 4.3. Measured and maximum NH_3 values in the liquid phase, along with the FE for each injection.

Injection # (-)	Measured NH_3 (µM)	Measured NH_3 (µmol)	Maximum NH_3 (µmol)	FE (%)
11	138.94	-	-	-
13	292.98	1.540	9.276	16.6
14	393.97	1.010	7.462	13.5
15	505.34	1.114	3.498	31.8

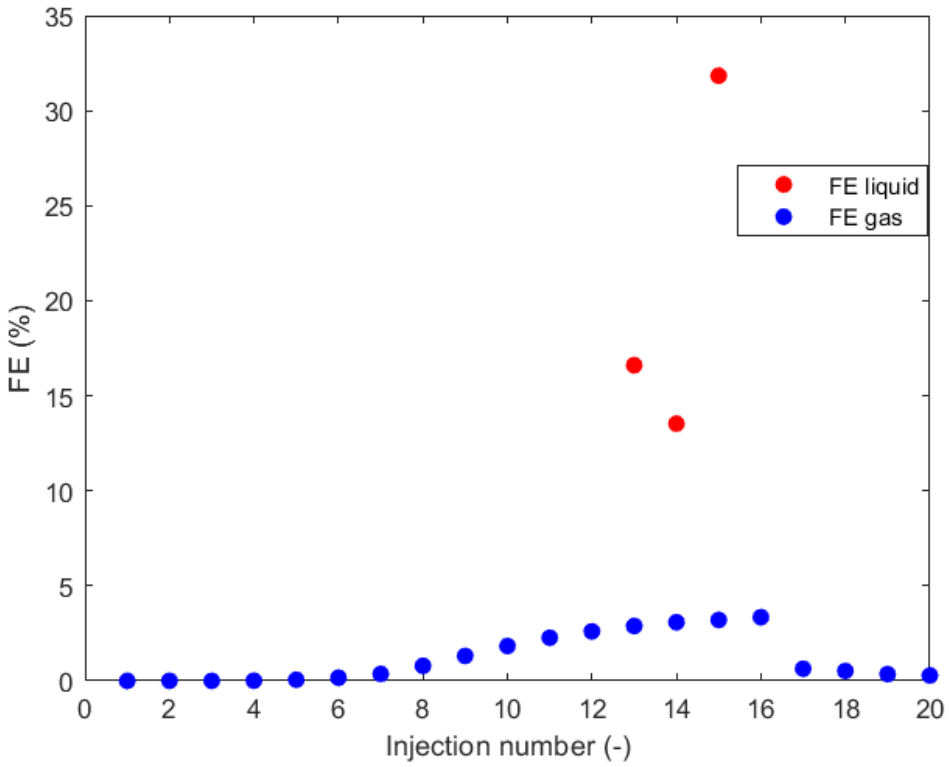

Figure 4.23. FE of the produced NH_3 in the gas and liquid phase. Measurements for the produced NH_3 in the liquid phase are only available for injections 13, 14 and 15.

First of all, it should be noted that FE value for injection 15 at 31.8 % is not accurate. The timescales between three different measurement techniques (GC, liquid samples, voltage) had to be synchronized during this experiment, which was challenging to achieve. As a result, the liquid sample for injection 15 most likely did not occur at t_3=1562 s, which causes the FE for that injection to be exaggerated. Therefore, this FE value is considered an outlier and won't be included in the discussion of the results of this experiment. As can be seen from Figure 4.23, the FE of NH_3 produced in the liquid phase is much higher compared to that of the gas phase, with the average value for injections 14 and 15 being 15.1 %. In comparison, the average FE for the gas phase during the same injections is 3.1 %. Based on these results, there is a ratio of 5:1 between the FE of NH_3 in the liquid and the gas phase.

However, during this experiment the flowrate of the nitrogen supply was set to 10 mL/min but only 1 mL/min reached the inlet of the GC. This indicates that leakage occurred at some point between the connections of the gas supply, the gas part, the water trap and the GC. If the leakage originated between

the outlet of the gas part and the GC, it would suggest that most of the supplied gas reached the cell and was involved in the electrochemical reactions. Consequently, only 10 % of the gas products reached the GC, while the remaining 90 % of the produced NH_3 was lost due to gas leakage. In this case, the FE of NH_3 in the gas phase would be 10 times higher, meaning that double the amount of NH_3 is produced in the gas phase compared to the liquid phase. If the leakage originated between the wall outlet and the gas part, then the produced NH_3 did not leak outside the cell and the results presented in Figure 4.23 are accurate.

Overall, this experiment showed that both GC and NMR spectroscopy can be utilized for the detection of NH_3 in the HTP cell. The detection with GC is faster than the detection with NMR, since the NH_3 concentration of the outlet stream of the gas part can be measured directly while the experiment is in progress. On the contrary, for the NMR spectroscopy measurements, the experiment must be interrupted to take a liquid sample from the electrolyte, which can then be measured only after the experiment is completed. Overall, the GC would lead to a more automated process, with more convenient and less time-consuming measurements. Additionally, GC is a technique that can be used in situ, which means that the supplied gas can be switched from nitrogen to argon during the same experiment. This could be used to verify that NH_3 is produced from nitrogen and is not a product of contamination.

However, current applied to one Cu dot during this experiment was -10 mA, which is considerably higher than the -500 μA applied during the electrochemical experiments conducted before the NO_3^- reduction experiment. This could lead to a situation where only a small amount of NH_3 is produced in the HTP cell and cannot be detected in the GC. Therefore, it is recommended that this experiment is repeated for a -500 μA current, no gas leakage and when current is applied to all 16 catalyst dots at the same time.

4.6.7. Initial NRR screening experiments

A PdRu bimetallic catalyst was used for the first catalyst screening experiment. The nitrogen supply was connected to the inlet of the gas part at the beginning of the experiment. The applied current to all 16 catalyst dots was -500 μA and the concentration of NH_3 would be measured by NMR spectroscopy of liquid samples from the electrolyte. However, during this experiment, the voltage values of the PdRu catalyst dots were higher compared to previous experiments with the same catalyst. Also, the voltage values appeared to be unstable, as shown in Figure 4.24.

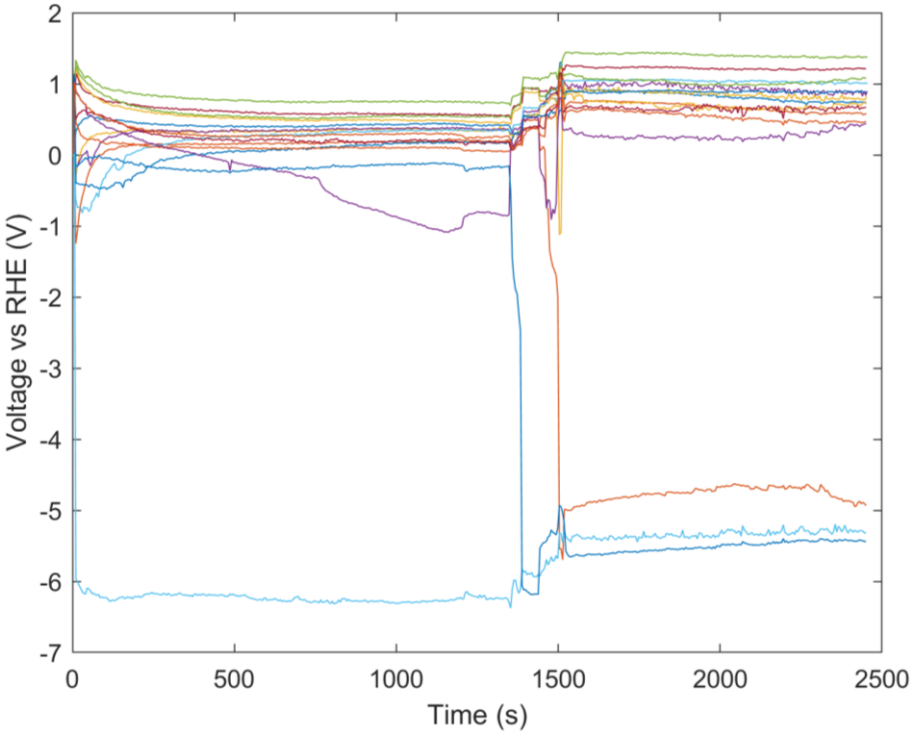

Figure 4.24. Voltage over time for 16 PdRu catalyst dots on pure ePTFE. The voltage of all catalyst dots except for one is between 0 and 1 V until t=1400 s, where it increases by 0.5 V for every dot. One catalyst dot was not operating correctly from the start of the experiment, while two more stop operating around t=1400 s.

Looking at the voltage values from the start of the experiment until t=1400 s, all of the dots are operating between 0 and 1 V except for one, which stopped operating and the voltage dropped to – 6 V. The applied current for this dot was 1.2 µA, which shows that very high resistance was encountered while applying current to this dot. A possible cause for this could be a nitrogen bubble that entered the cell and prevented the catalyst dot from contacting the gold contact of the PCB. Another possibility is that leakage occurred at that dot, meaning that there was no electrolyte left to facilitate that transport of ions. The rest of the catalyst dots operated at a higher voltage compared to previous experiments. After t=1400 s two more catalyst dots stopped operating, with the current applied to them being at 1.1 µA. This caused an increase in the voltage of the other 13 catalyst dots of the HTP that were still operating normally. It appears that the voltage that a catalyst is operating at, is affected by the voltage of other catalyst in the cell, which should not be the case. An experiment with only 8 out of 16 dots operating was conducted to test this theory. The PdRu catalyst, 0.1 M KOH electrolyte and applied current remain unchanged from the previous experiment. The results are presented in Figure 4.25.

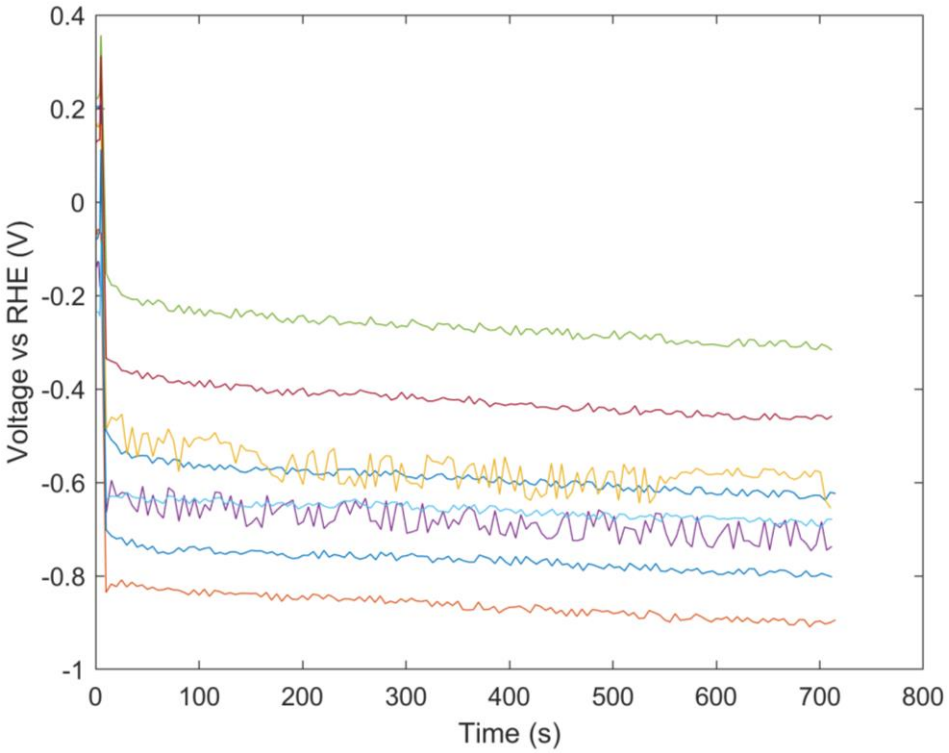

Figure 4.25. Voltage over time for 8 PdRu catalyst dots on pure ePTFE. The voltage values are between -0.2 V and -0.9 V and no catalyst dots stopped operating during this experiment.

The voltage values encountered when only 8 out of 16 catalyst dots are operating, are substantially lower compared to the values shown in Figure 4.24. During this experiment the voltage values are between -0.2 and -0.9 V compared to 0 and 1 V in the experiment with all 16 catalyst dots. Furthermore, the voltage values have a 0.7 V range, which could indicate that the electrolyte has a higher resistance compared to previous experiments. The expected maximum range of the voltage values was around 0.3 V, as shown in Figure 4.17. This was tested further by conducting experiments with 4 active dots, 2 and eventually only one active dot. In each one of those experiments, the measured voltage of the dots decreased even further. These results suggest that the voltage of each dot is affected by the operating voltage of other dots in the cell.

A possible reason that the voltage was unstable is that the RE was damaged during previous electrochemical experiments. The voltage of the currently used hydrogen RE had previously been measured vs a Hg/HgO RE, showing less than 6 mV difference. However, when the hydrogen RE was measured again vs a Hg/HgO RE after the NO_3^- experiment, the potential was very unstable and it was impossible to obtain an accurate measurement. It is likely that metal ions were deposited on the tip of the hydrogen RE during previous experiments.

This problem could be solved by discarding the RE and moving to a 2-electrode configuration. Another possible solution to this problem could be the use of 16 CEs, as currently only one Ni wire is

used as a CE. One way of implementing this is discussed in Section 5 in the conclusions and recommendations for future research in this project.

5
Conclusion and recommendations

The main goal of this project was to design a high-throughput electrochemical cell that can be used for the screening of large numbers of bimetallic catalysts, increasing the chance of finding a suitable NRR catalyst. In this project, high-throughput techniques were implemented both during the preparation and the screening of the bimetallic catalysts. Conducting chronopotentiometry experiments on 16 unique bimetallic catalyst compositions simultaneously, shows the importance of implementing HTE in electrochemistry as a tool to accelerate the discovery of new catalysts.

The HTP cell uses an ePTFE GDE that electrically isolates the 16 sputtered catalyst dots on it. The carbon GDE that was tested, substantially increased the complexity and the assembly time of the electrochemical cell and was deemed unsuitable for this project. The electrical connection of the 16 catalyst dots on pure ePTFE substrate with the multichannel potentiostat was achieved by using a PCB. The use of Dupont connectors with the PCB created a more stable electrical contact compared to copper tape, while also reducing the assembly time of the HTP cell configuration.

During the SEM imaging of the catalysts on pure ePTFE, areas of inhomogeneous metal deposition and continuous layers of metal were detected. Additional work is required to determine whether it is a random occurrence or it depends directly on the thickness of the sputtered metal. This could be achieved by sputtering different thickness of metal on different ePTFE samples and then identifying the accumulation of metal around the fibers of the ePTFE and the formation of continuous layers on each sample.

The XRD pattern of the bimetallic catalysts was also measured and compared to the patterns reported in literature for the same catalysts. It was found that the diffraction peaks of the sputtered catalysts occurred at the same angles as the ones in literature, showing that the same alloys are created through sputtering as with other manufacturing techniques. This shows that HTE can be used to rapidly validate the XRD patterns reported in literature.

The HTP cell was validated by means of NH_3 background, loss and crossover experiments. It was found that no NH_3 is oxidized at the anode but it can cross over from the catholyte to the anolyte compartment through the Zirfon membrane, which indicates that more selective ion exchange membranes could be used. These experiments also show the importance of implementing a cleaning procedure for the cell components to prevent NH_3 contamination between the screening of different bimetallic catalysts.

Additionally, an experiment for NO_3^- reduction was conducted to determine if GC could be used as a quantification method for the amount of produced NH_3. The NH_3 concentration in the gas phase was measured by GC while the concentration in the liquid phase was measured by NMR spectroscopy.

It was found that there is a ratio of 5:1 between FE of NH_3 in the liquid and the gas phase. However, it was concluded that GC is a technique that is more suitable for the HTP aspect of this project, as the NH_3 concentration can be measured in situ.

During the initial catalyst screening experiments, it was discovered that the voltage that each catalyst dot operates at, is affected by the number of catalyst dots operating in the HTP cell. This is possibly caused by the use of a single CE in the anolyte compartment, namely the spiral Ni wire. The Ni wire could be replaced by a PCB with 16 Ni wires, each one soldered on one of the gold contacts of the PCB. In this configuration, every catalyst dot will operate independently of the others, since it will be electrically isolated from them.

Finally, the catalytic activity of a metal varies depending on the temperature that the reaction takes place. Therefore, for the catalyst screening experiments it is recommended that the catalytic activity of a bimetallic catalyst is also tested for higher temperatures, up to 70 ^{o}C. For such an experiment, the HTP cell would be placed in an oven to maintain a constant temperature. Tests at different temperatures could provide more opportunities for new catalysts to be discovered with the HTP cell.

References

[1] J. Deng, J. A. Iñiguez and C. Liu, "Electrocatalytic Nitrogen Reduction at Low Temperature," *Joule,* vol. 2, pp. 846-856, 2018.

[2] S. L. Foster, S. I. P. Bakovic, R. D. Duda, S. Maheshwari, R. D. Milton, S. D. Minteer, M. J. Janik, J. N. Renner and L. F. Greenlee, "Catalysts for nitrogen reduction to ammonia," *Nature Catalysis,* vol. 1, p. 490–500, 2018.

[3] R. M. Nayak-Luke and R. Bañares-Alcántara, "Long-Term Energy Storage: What is the Need and is Ammonia a Solution?," in *13th International Symposium on Process Systems Engineering (PSE 2018)*, vol. 44, M. R. Eden, M. G. Ierapetritou and G. P. Towler, Eds., Elsevier, 2018, pp. 1843-1848.

[4] M. A. Shipman and M. D. Symes, "Recent progress towards the electrosynthesis of ammonia from sustainable resources," *Catalysis Today,* vol. 286, pp. 57-68, 2017.

[5] R. Strait and M. Nagvekar, "Carbon Dioxide Capture and Storage in the Nitrogen Syngas Industries," *Nitrogen+Syngas,* 2010.

[6] Y. Bicer, I. Dincer, G. Vezina and F. Raso, "Impact Assessment and Environmental Evaluation of Various Ammonia Production Processes," *Environmental Management,* vol. 59, p. 842–855, 2017.

[7] Y. Wan, J. Xu and R. Lv, "Heterogeneous electrocatalysts design for nitrogen reduction reaction under ambient conditions," *Materials Today,* vol. 27, pp. 69-90, 2019.

[8] C. Guo, J. Ran, A. Vasileff and S.-Z. Qiao, "Rational design of electrocatalysts and photo(electro)catalysts for nitrogen reduction to ammonia (NH3) under ambient conditions," *Energy Environ. Sci.,* vol. 11, no. 1, pp. 45-56, 2018.

[9] X. Cui, C. Tang and Q. Zhang, "A Review of Electrocatalytic Reduction of Dinitrogen to Ammonia under Ambient Conditions," *Advanced Energy Materials,* vol. 8, p. 1800369, 2018.

[10] C. J. M. van der Ham, M. T. M. Koper and D. G. H. Hetterscheid, "Challenges in reduction of dinitrogen by proton and electron transfer," *Chem. Soc. Rev.,* vol. 43, no. 15, pp. 5183-5191, 2014.

[11] J. H. Montoya, C. Tsai, A. Vojvodic and J. K. Nørskov, "The Challenge of Electrochemical Ammonia Synthesis: A New Perspective on the Role of Nitrogen Scaling Relations," *ChemSusChem,* vol. 8, pp. 2180-2186, 2015.

[12] X. Guo, H. Du, F. Qu and J. Li, "Recent progress in electrocatalytic nitrogen reduction," *J. Mater. Chem. A,* vol. 7, no. 8, pp. 3531-3543, 2019.

[13] T. Muster, A. Trinchi, T. A. Markley, D. Lau, P. Martin, A. Bradbury, A. Bendavid and S. Dligatch, "A review of high throughput and combinatorial electrochemistry," *Electrochimica Acta,* vol. 56, p. 9679–9699, 11 2011.

[14] V. Kulikov and V. M. Mirsky, "Equipment for combinatorial electrochemical polymerization and high-throughput investigation of electrical properties of the synthesized polymers," *Measurement Science and Technology,* vol. 15, pp. 49-54, 2003.

[15] W. Yu, M. D. Porosoff and J. G. Chen, "Review of Pt-Based Bimetallic Catalysis: From Model Surfaces to Supported Catalysts," *Chem. Rev.,* vol. 112, p. 5780–5817, 11 2012.

[16] M. Zhong, K. Tran, Y. Min, C. Wang, Z. Wang, C.-T. Dinh, P. De Luna, Z. Yu, A. S. Rasouli, P. Brodersen, S. Sun, O. Voznyy, C.-S. Tan, M. Askerka, F. Che, M. Liu, A. Seifitokaldani, Y. Pang, S.-C. Lo, A. Ip, Z. Ulissi and E. H. Sargent, "Accelerated discovery of CO2 electrocatalysts using active machine learning," *Nature,* vol. 581, p. 178–183, 2020.

[17] T. Burdyny and W. A. Smith, "CO2 reduction on gas-diffusion electrodes and why catalytic performance must be assessed at commercially-relevant conditions," *Energy Environ. Sci.,* vol. 12, p. 1442–1453, 2019.

[18] F. Fichter and R. Suter, "Zur Frage der kathodischen Reduktion des elementaren Stickstoffs," *Helvetica Chimica Acta,* vol. 5, pp. 246-255, 1922.

[19] A. J. Martín, T. Shinagawa and J. Pérez-Ramírez, "Electrocatalytic Reduction of Nitrogen: From Haber-Bosch to Ammonia Artificial Leaf," *Chem,* vol. 5, pp. 263-283, 2019.

[20] A. Singh, B. A. Rohr, M. J. Statt, J. A. Schwalbe, M. Cargnello and J. K. Nørskov, "Strategies toward Selective Electrochemical Ammonia Synthesis," *ACS Catal.,* vol. 9, p. 8316–8324, 9 2019.

[21] C. H. Christensen, T. Johannessen, R. Z. Sørensen and J. K. Nørskov, "Towards an ammonia-mediated hydrogen economy?," *Catalysis Today,* vol. 111, pp. 140-144, 2006.

[22] E. Skúlason, T. Bligaard, S. Gudmundsdóttir, F. Studt, J. Rossmeisl, F. Abild-Pedersen, T. Vegge, H. Jónsson and J. K. Nørskov, "A theoretical evaluation of possible transition metal electro-catalysts for N2 reduction," *Phys. Chem. Chem. Phys.,* vol. 14, no. 3, pp. 1235-1245, 2012.

[23] J. Greeley, "Theoretical Heterogeneous Catalysis: Scaling Relationships and Computational Catalyst Design," *Annu. Rev. Chem. Biomol. Eng.,* vol. 7, p. 605–635, 6 2016.

[24] T. F. Jaramillo, S.-H. Baeck, A. Kleiman-Shwarsctein and E. W. McFarland, "Combinatorial Electrochemical Synthesis and Screening of Mesoporous ZnO for Photocatalysis," *Macromol. Rapid Commun.,* vol. 25, p. 297–301, 1 2004.

[25] E. Reddington, A. Sapienza, B. Gurau, R. Viswanathan, S. Sarangapani, E. S. Smotkin and T. E. Mallouk, "Combinatorial electrochemistry: A highly parallel, optical screening method for discovery of better electrocatalysts," *Science (New York, N.Y.),* vol. 280, p. 1735–1737, 1998.

[26] T. Iwasita, "Electrocatalysis of methanol oxidation," *Electrochimica Acta,* vol. 47, p. 3663–3674, 2002.

[27] J. S. Cooper and P. J. McGinn, "Combinatorial screening of fuel cell cathode catalyst compositions," *Applied Surface Science,* vol. 254, p. 662–668, 2007.

[28] D. A. Stevens, J. M. Rouleau, R. E. Mar, A. Bonakdarpour, R. T. Atanasoski, A. K. Schmoeckel, M. K. Debe and J. R. Dahn, "Characterization and PEMFC Testing of Pt[sub 1−x]M[sub x] (M=Ru,Mo,Co,Ta,Au,Sn) Anode Electrocatalyst Composition Spreads," *Journal of The Electrochemical Society,* vol. 154, p. B566, 2007.

[29] N. Gupta, M. Gattrell and B. MacDougall, "Calculation for the cathode surface concentrations in the electrochemical reduction of CO2 in KHCO3 solutions," *Journal of Applied Electrochemistry,* vol. 36, p. 161–172, 2006.

[30] K. Liu, W. A. Smith and T. Burdyny, "Introductory Guide to Assembling and Operating Gas Diffusion Electrodes for Electrochemical CO2 Reduction," *ACS Energy Lett.,* vol. 4, p. 639–643, 3 2019.

[31] G. Larrazábal, P. Strøm-Hansen, J. P. Heli, K. Zeiter, K. T. Therkildsen, I. Chorkendorff and B. Seger, "Analysis of Mass Flows and Membrane Cross-over in CO2 Reduction at High Current Densities in an MEA-Type Electrolyzer," *ACS Appl. Mater. Interfaces,* vol. 11, p. 41281–41288, 11 2019.

[32] D. Raciti, M. Mao, J. H. Park and C. Wang, "Mass transfer effects in CO2 reduction on Cu nanowire electrocatalysts," *Catal. Sci. Technol.,* vol. 8, p. 2364–2369, 2018.

[33] D. Higgins, C. Hahn, C. Xiang, T. F. Jaramillo and A. Z. Weber, "Gas-Diffusion Electrodes for Carbon Dioxide Reduction: A New Paradigm," *ACS Energy Lett.,* vol. 4, p. 317–324, 1 2019.

[34] P. H. Vermeiren, R. Leysen, H. Beckers, J. P. Moreels and A. Claes, "The influence of manufacturing parameters on the properties of macroporous Zirfon® separators," *Journal of Porous Materials,* vol. 15, p. 259–264, 2008.

[35] R. Cardeña, B. Cercado, G. Buitrón, A. Pandey, S. V. Mohan, J.-S. Chang, P. C. Hallenbeck and C. Larroche, "Chapter 7 - Microbial Electrolysis Cell for Biohydrogen Production," in *Biohydrogen (Second Edition)*, Elsevier, 2019, p. 159–185.

[36] F. Hanifpour, A. Sveinbjörnsson, C. P. Canales, E. Skúlason and H. D. Flosadóttir, "Preparation of Nafion Membranes for Reproducible Ammonia Quantification in Nitrogen Reduction Reaction Experiments," *Angew. Chem. Int. Ed.,* vol. 59, p. 22938–22942, 12 2020.

[37] M. M. Hassan and A. Tiwari, "16 - Antimicrobial Coatings for Textiles," in *Handbook of Antimicrobial Coatings*, Elsevier, 2018, p. 321–355.

[38] F. Pang, Z. Wang, K. Zhang, J. He, W. Zhang, C. Guo and Y. Ding, "Bimodal nanoporous Pd3Cu1 alloy with restrained hydrogen evolution for stable and high yield electrochemical nitrogen reduction," *Nano Energy,* vol. 58, p. 834–841, 2019.

[39] Z. Wang, C. Li, K. Deng, Y. Xu, H. Xue, X. Li, L. Wang and H. Wang, "Ambient Nitrogen Reduction to Ammonia Electrocatalyzed by Bimetallic PdRu Porous Nanostructures," *ACS Sustainable Chem. Eng.,* vol. 7, p. 2400–2405, 1 2019.

[40] H. Yu, Z. Wang, D. Yang, X. Qian, Y. Xu, X. Li, H. Wang and L. Wang, "Bimetallic Ag3Cu porous networks for ambient electrolysis of nitrogen to ammonia," *J. Mater. Chem. A,* vol. 7, p. 12526–12531, 2019.

[41] Y. Liu, L. Huang, X. Zhu, Y. Fang and S. Dong, "Coupling Cu with Au for enhanced electrocatalytic activity of nitrogen reduction reaction," *Nanoscale,* vol. 12, p. 1811–1816, 2020.

[42] L. Xia, B. Li, Y. Zhang, R. Zhang, L. Ji, H. Chen, G. Cui, H. Zheng, X. Sun, F. Xie and Q. Liu, "Cr2O3 Nanoparticle-Reduced Graphene Oxide Hybrid: A Highly Active Electrocatalyst for N2 Reduction at Ambient Conditions," *Inorg. Chem.,* vol. 58, p. 2257–2260, 2 2019.

[43] R. Zhang, H. Guo, L. Yang, Y. Wang, Z. Niu, H. Huang, H. Chen, L. Xia, T. Li, X. Shi, X. Sun, B. Li and Q. Liu, "Electrocatalytic N2 Fixation over Hollow VO2 Microspheres at Ambient Conditions," *ChemElectroChem,* vol. 6, p. 1014–1018, 2 2019.

[44] X. Ren, J. Zhao, Q. Wei, Y. Ma, H. Guo, Q. Liu, Y. Wang, G. Cui, A. M. Asiri, B. Li, B. Tang and X. Sun, "High-Performance N2-to-NH3 Conversion Electrocatalyzed by Mo2C Nanorod," *ACS Cent. Sci.,* vol. 5, p. 116–121, 1 2019.

[45] Y. Tong, H. Guo, D. Liu, X. Yan, P. Su, J. Liang, S. Zhou, J. Liu, G. Q. (. Lu and S. X. Dou, "Vacancy Engineering of Iron-Doped W18O49 Nanoreactors for Low-Barrier Electrochemical Nitrogen Reduction," *Angew. Chem. Int. Ed.,* vol. 59, p. 7356–7361, 5 2020.

[46] W. Guo, Z. Liang, J. Zhao, B. Zhu, K. Cai, R. Zou and Q. Xu, "Hierarchical Cobalt Phosphide Hollow Nanocages toward Electrocatalytic Ammonia Synthesis under Ambient Pressure and Room Temperature," *Small Methods,* vol. 2, p. 1800204, 12 2018.

[47] H. Wang, H. Yu, Z. Wang, Y. Li, Y. Xu, X. Li, H. Xue and L. Wang, "Electrochemical Fabrication of Porous Au Film on Ni Foam for Nitrogen Reduction to Ammonia," *Small,* vol. 15, p. 1804769, 2 2019.

[48] M.-M. Shi, D. Bao, B.-R. Wulan, Y.-H. Li, Y.-F. Zhang, J.-M. Yan and Q. Jiang, "Au Sub-Nanoclusters on TiO2 toward Highly Efficient and Selective Electrocatalyst for N2 Conversion to NH3 at Ambient Conditions," *Adv. Mater.,* vol. 29, p. 1606550, 5 2017.

[49] H. Tao, C. Choi, L.-X. Ding, Z. Jiang, Z. Han, M. Jia, Q. Fan, Y. Gao, H. Wang, A. W. Robertson, S. Hong, Y. Jung, S. Liu and Z. Sun, "Nitrogen Fixation by Ru Single-Atom Electrocatalytic Reduction," *Chem,* vol. 5, p. 204–214, 2019.

[50] P. Tiwari, G. Tsekouras, G. F. Swiegers and G. G. Wallace, "Gortex-Based Gas Diffusion Electrodes with Unprecedented Resistance to Flooding and Leaking," *ACS Appl. Mater. Interfaces,* vol. 10, p. 28176–28186, 8 2018.

[51] X. Xiang, Y. Ju, M. Wang, Y. Wang, S. Wang and C. Fu, "Electrical Properties of Amorphous Titanium Oxide Thin Films for Bolometric Application," *Advances in Condensed Matter Physics,* vol. 2013, p. 365475, 2013.

Appendix

A1. MATLAB code for the composition calculator

```
close all;clear all;clc;

%% Loading the data
% First we are reading the names of all the elements and their molar
volume

[NUM, TXT, RAW] = xlsread('Power calculator - Greg.xlsx','B2:B138');
Element = TXT;
Molar_volume = xlsread('Power calculator - Greg.xlsx','C2:C138');

% Request the names of the two metals
prompt1 = 'Which one is the first metal? ';
M1 = input(prompt1,'s');
prompt2 = 'Which one is the second metal? ';
M2 = input(prompt2,'s');

M1 = {M1};
M2 = {M2};

%% Finding the position of the two metals in the tables
% We find the position of each element on the table to find the
corresponding
% molar volume
for i=1:length(Element)
    if isequal(M1{1}, Element{i})
        MV1 = Molar_volume(i);
    elseif isequal(M2{1}, Element{i})
        MV2 = Molar_volume(i);
    end
end

%% Composition, tooled rate and power
prompt3 = 'What is the composition of the first metal? ';
Comp_M1 = input(prompt3);
Comp_M2 = 100-Comp_M1;
prompt5 = 'What is the tooled rate of the first metal? ';
Tooled_rate_M1 = input(prompt5);    % A/s
prompt6 = 'What is the tooled rate of the second metal? ';
Tooled_rate_M2 = input(prompt6);    % A/s

% Power at which the tooling data was measured
prompt7 = 'What is the tooled power of the first metal? ';
Tooled_power_M1 = input(prompt7);   % W
prompt8 = 'What is the tooled power of the second metal? ';
Tooled_power_M2 = input(prompt8);   % W

% Wish rate of metal 2, how much it should be in order to give the
correct
```

```
% composition
Wish_rate_M1 = Tooled_rate_M1;
Wish_rate_M2 = (Wish_rate_M1/(Comp_M1*MV1))*(Comp_M2*MV2);
Total_tooled_rate = Wish_rate_M1+Wish_rate_M2;

% Power to set at the guns
Final_power_M1 = (Wish_rate_M1*Tooled_power_M1)/Tooled_rate_M1;
Final_power_M2 = (Wish_rate_M2*Tooled_power_M2)/Tooled_rate_M2;

% Making sure that the final power of the guns doesn't exceed 200 W
while Final_power_M2>200
    Wish_rate_M1 = Wish_rate_M1/2;
    Wish_rate_M2 = (Wish_rate_M1/(Comp_M1*MV1))*(Comp_M2*MV2);
    Total_tooled_rate = Wish_rate_M1+Wish_rate_M2;
    Final_power_M1 = (Wish_rate_M1*Tooled_power_M1)/Tooled_rate_M1;
    Final_power_M2 = (Wish_rate_M2*Tooled_power_M2)/Tooled_rate_M2;
end


% Total thickness at the middle of the PCB
prompt9 = 'What is the expected thickness at the middle? (in nm) ';
Total_thickness = input(prompt9);

% Deposition time
Time = Total_thickness*10/Total_tooled_rate;   % seconds
Final_time = fix(mod(Time, [0, 3600, 60]) ./ [3600, 60, 1]);   %
minutes + seconds

%% Composition calculator on each dot of the PCB

% Loading the experimental results
% We read the thickness of the deposited layer for ech metal and
angle for
% M2, which can be either 90 or 180. The angle for M1 is always
considered
% zero.

M1_thickness = xlsread('Power calculator - Greg.xlsx','F5:F8');
M2_thickness = xlsread('Power calculator - Greg.xlsx','G5:G8');
% Duration of the deposition for the tooling data
prompt10 = 'What is the duration of the deposition of the first
metal? (in s) ';
Time_M1 = input(prompt10);
prompt11 = 'What is the duration of the deposition of the second
metal? (in s) ';
Time_M2 = input(prompt11);
prompt12 = 'What is the sputtering angle of the second metal? (180
or 90) ';
M2_angle = input(prompt12);
Length4 = [13; 23; 33; 43];  %Position of the dots on the 4x4 PCB

%% Thickness increase per cm
% We calculate the thickness increase per cm on the PCB. This will
be used
% later in the case of M2 having a 90 degree angle. The thickness is
% changed due to the new power and deposition time
```

```
M1_thickness =
M1_thickness*(Final_power_M1/Tooled_power_M1)*(Time/Time_M1);
M2_thickness =
M2_thickness*(Final_power_M2/Tooled_power_M2)*(Time/Time_M2);

for i=1:length(Length4)
    thickness_incM1(i) = M1_thickness(i)/Length4(5-i);
    thickness_incM2(i) = M2_thickness(i)/Length4(i);
end
Avg_thickness_incM1 =
(thickness_incM1(1)+thickness_incM1(2)+thickness_incM1(3)+thickness_
incM1(4))/4;
Avg_thickness_incM2 =
(thickness_incM2(1)+thickness_incM2(2)+thickness_incM2(3)+thickness_
incM2(4))/4;

% Polynomial for the thickness
pfitM1 = polyfit(Length4, M1_thickness, 1);
pfitM2 = polyfit(Length4, M2_thickness, 1);

% Thickness at the middle of the PCB (28mm x 28mm)
Middle_M1_thickness = Avg_thickness_incM1*28;
Middle_M2_thickness = Avg_thickness_incM2*28;

% Composition at the middle of the PCB (28mm x 28mm)
Middle_M2_comp =
(100*Middle_M2_thickness*MV1)/(Middle_M1_thickness*MV2+Middle_M2_thi
ckness*MV1);
Middle_M1_comp = 100-Middle_M2_comp;


%% Predicting the composition on the 4x4 PCB

if M2_angle==180
    % Position of each dot on the 4x4 PCB
    [Final_M1_comp] = zeros(4,1);
    [Final_M2_comp] = zeros(4,1);
    [Final_M1_thickness] = zeros(4,1);
    [Final_M2_thickness] = zeros(4,1);

    for i=1:length(Length4)
        Final_M1_thickness(i) = pfitM1(1)*Length4(i)+pfitM1(2);
        Final_M2_thickness(i) = pfitM2(1)*Length4(i)+pfitM2(2);
    end

    for i=1:length(Length4)
        Final_M2_comp(i) =
(100*Final_M2_thickness(i)*MV1)/(Final_M1_thickness(i)*MV2+Final_M2_
thickness(i)*MV1);
        Final_M1_comp(i) = 100-Final_M2_comp(i);
    end


    % Gradient per cm
```

```
    % This calculates the gradient (the composition increase) per cm
on the PCB
    % First we find the composition% increase for each individual
dot, then we
    % take the average. We repeat the same for every metal.

    for i=1:length(Length4)
        Total_thickness(i) =
Final_M1_thickness(i)+Final_M2_thickness(i);
        Comp_incM1(i) = Final_M1_comp(i)/Length4(5-i);
        Comp_incM2(i) = Final_M2_comp(i)/Length4(i);
    end

    Avg_comp_incM1 =
(Comp_incM1(1)+Comp_incM1(2)+Comp_incM1(3)+Comp_incM1(4))/4;
    Avg_comp_incM2 =
(Comp_incM2(1)+Comp_incM2(2)+Comp_incM2(3)+Comp_incM2(4))/4;

elseif M2_angle==90
    % M2 is sputtered perpendicular to M1
    % M1 is always considered to be angle 0. M2 was at angle 180 so
far, in
    % this case it is at angle 90.
    [Final_M1_comp] = zeros(4,4);
    [Final_M2_comp] = zeros(4,4);
    [Final_M1_thickness] = zeros(4,4);
    [Final_M2_thickness] = zeros(4,4);
    for j=1:length(Length4)
        for i=1:length(Length4)
            Final_M1_thickness(i,j) =
pfitM1(1)*Length4(j)+pfitM1(2);
            Final_M2_thickness(i,j) = pfitM2(1)*Length4(5-
i)+pfitM2(2);
        end
    end
    for i=1:length(Length4)
        for j=1:length(Length4)
            Total_thickness(i,j) =
Final_M1_thickness(i,j)+Final_M2_thickness(i,j);
            Final_M2_comp(i,j) =
(100*Final_M2_thickness(i,j)*MV1)/(Final_M1_thickness(i,j)*MV2+Final
_M2_thickness(i,j)*MV1);
            Final_M1_comp(i,j) = 100-Final_M2_comp(i,j);
        end
    end
end

% Plots
figure(1)
h1 = heatmap(Final_M1_comp);
title('Composition of M1 (%)');
figure(2)
h2 = heatmap(Final_M2_comp);
title('Composition of M2 (%)');
figure(3)
h3 = heatmap(Total_thickness');
```

```
title('Deposition thickness on the PCB (nm)');

% Output of power and deposition time
hours = Final_time(1);
minutes = Final_time(2);
seconds = Final_time(3);
P1 = ['The power of the first gun is ', num2str(Final_power_M1), '
W'];
P2 = ['The power of the second gun is ', num2str(Final_power_M2), '
W'];
if hours ~=0
    T = ['The deposition time is ', num2str(hours), ' hours , '
num2str(minutes), ' minutes and ', num2str(seconds), ' seconds'];
    disp(P1)
    disp(P2)
    disp(T)
else
    T = ['The deposition time is ', num2str(minutes), ' minutes and
', num2str(seconds), ' seconds'];
    disp(P1)
    disp(P2)
    disp(T)
end
```

A2. Technical drawing of the HTP cell components

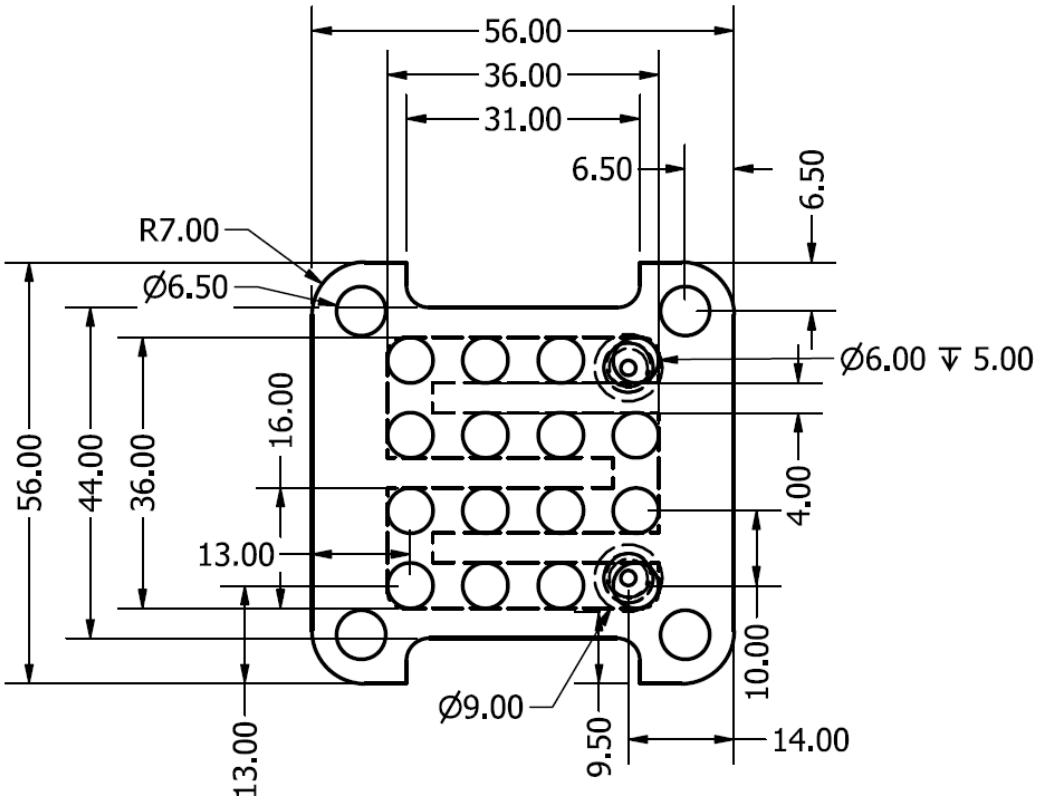

Figure A1. Top view of the gas part with serpentine flow path.

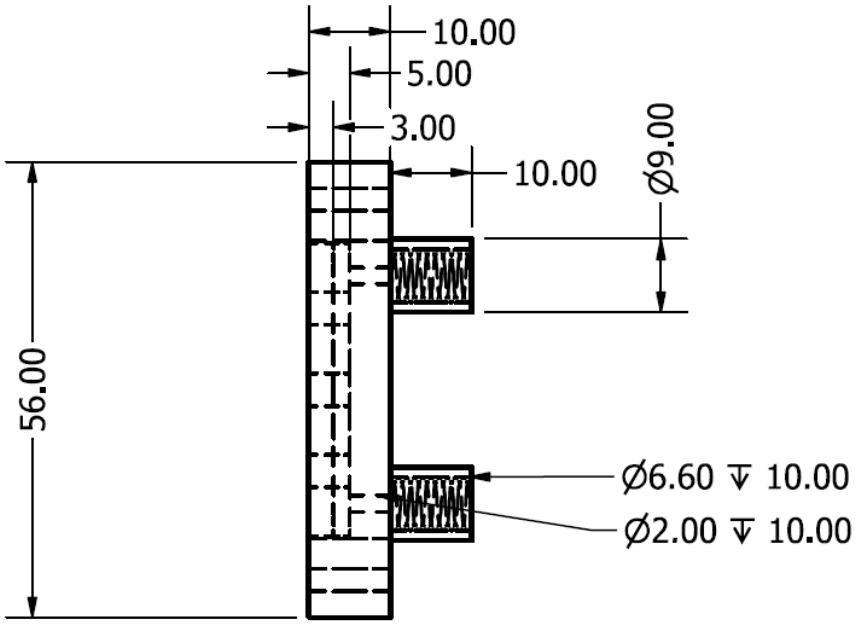

Figure A2. Side view of the gas part with serpentine flow path.

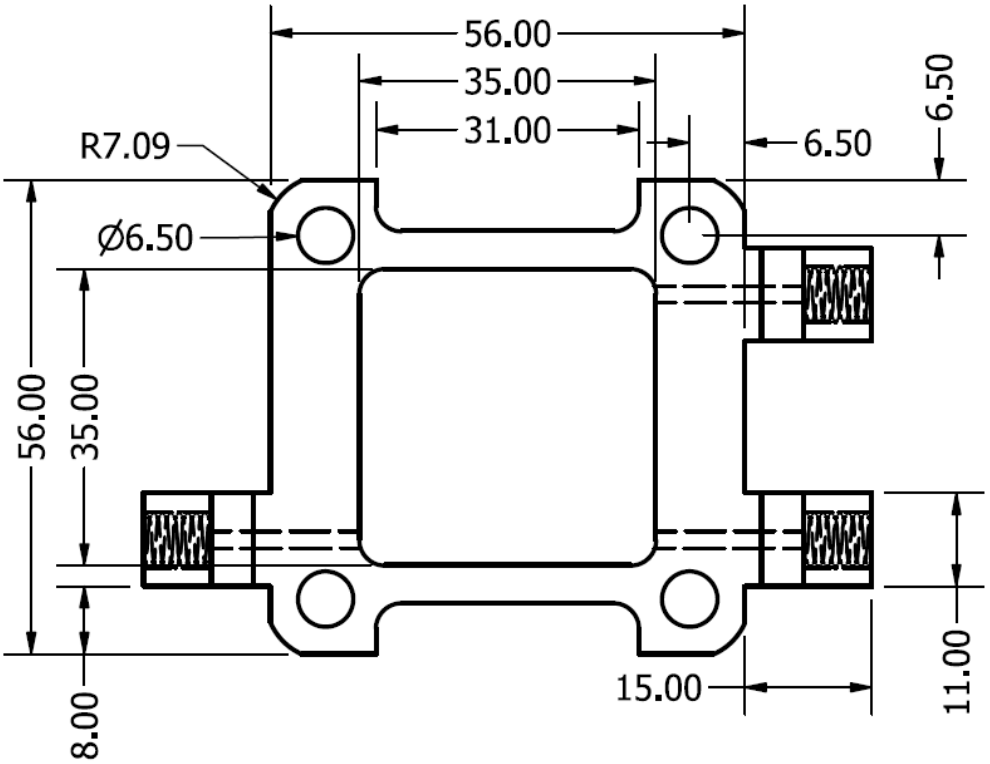

Figure A3. Top view of the catholyte part.

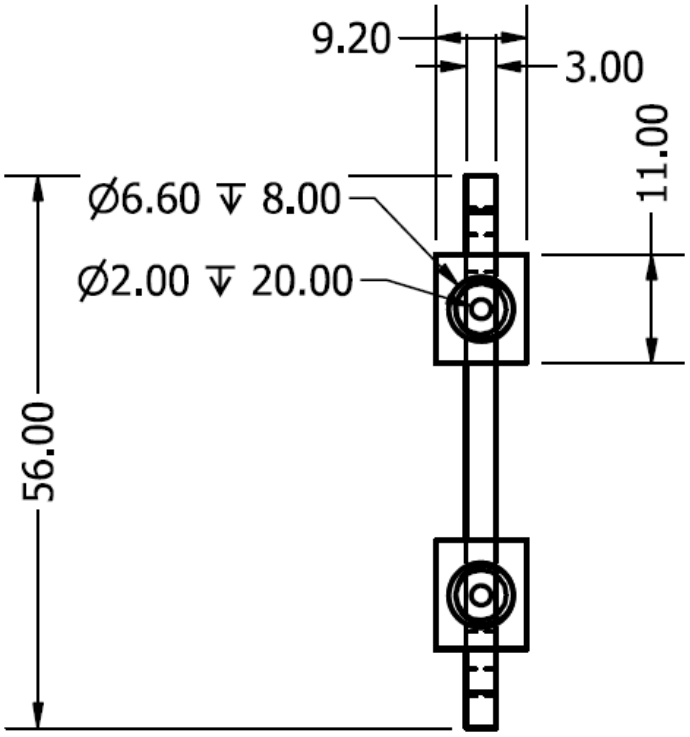

Figure A4. Side view of the catholyte part.

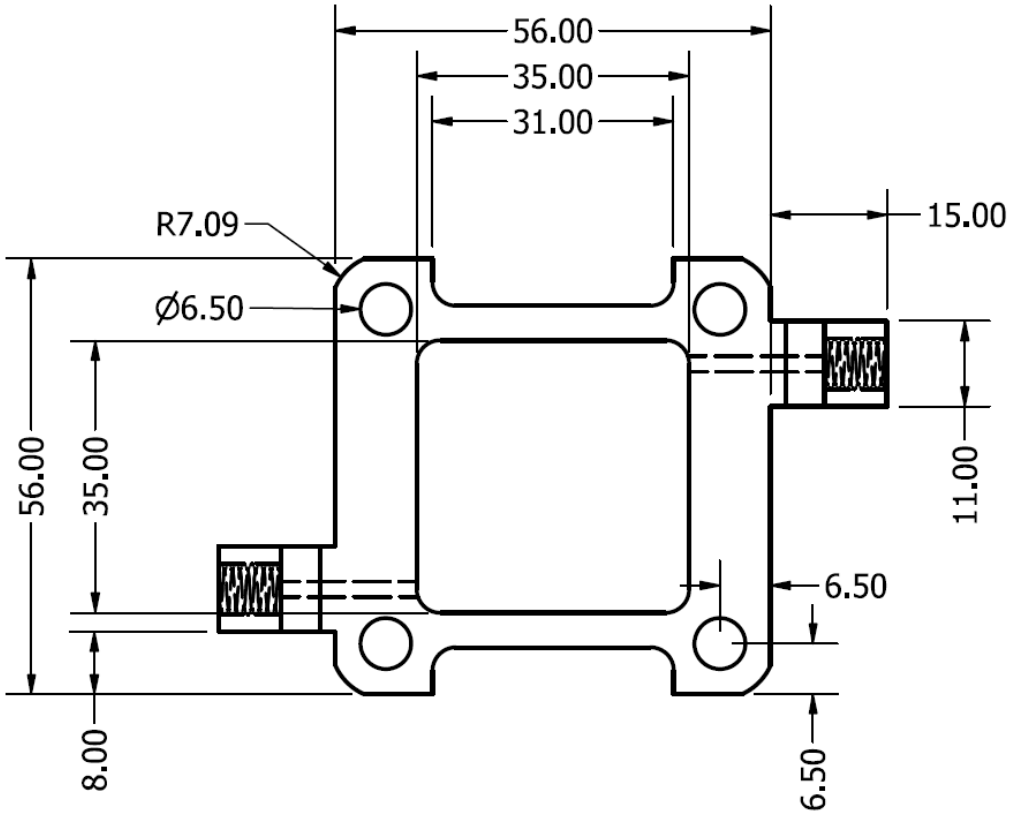

Figure A5. Top view of the anolyte part.

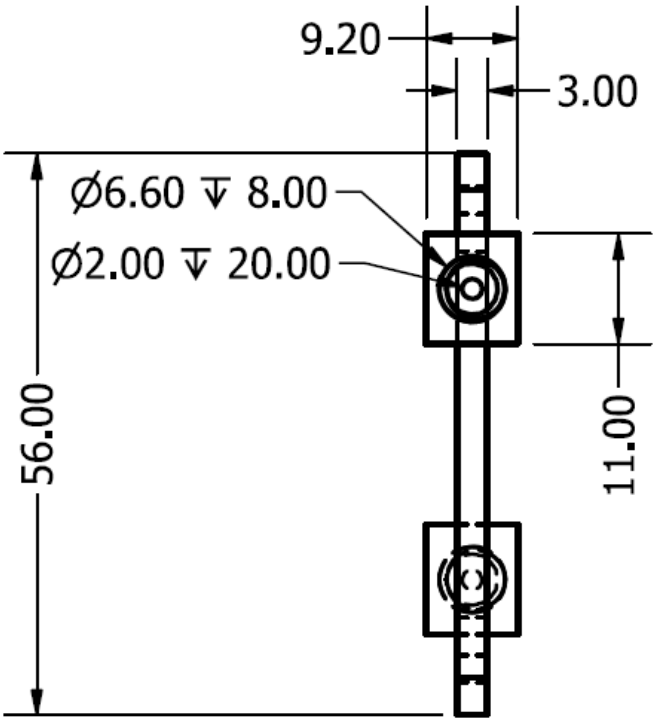

Figure A6. Side view of the anolyte part.